


Towards a quantum interface between spin waves and paramagnetic spin bathsC. Gonzalez-Ballester^{1,2,*}, Toeno van der Sar³, and O. Romero-Isart^{1,2}¹*Institute for Quantum Optics and Quantum Information of the Austrian Academy of Sciences, 6020 Innsbruck, Austria*²*Institute for Theoretical Physics, University of Innsbruck, A-6020 Innsbruck, Austria*³*Department of Quantum Nanoscience, Kavli Institute of Nanoscience, Delft University of Technology, Lorentzweg 1, 2628 CJ, Delft, The Netherlands* (Received 7 December 2020; revised 10 January 2022; accepted 12 January 2022; published 8 February 2022)

Spin waves have risen as promising candidate information carriers for the next generation of information technologies. Recent experimental demonstrations of their detection using electron spins in diamond pave the way towards studying the back-action of a controllable paramagnetic spin bath on the spin waves. Here, we present a macroscopic quantum theory describing the interaction between spin waves and paramagnetic spins. As a case study, we consider an ensemble of nitrogen-vacancy spins in diamond in the vicinity of an yttrium-iron-garnet thin film. We show how the back-action of the ensemble results in strong and tuneable modifications of the spin wave spectrum and propagation properties. These modifications include the full suppression of spin wave propagation and, in a different parameter regime, the enhancement of their propagation length by $\sim 50\%$ for modes near resonance with the NV transition frequency. Furthermore, we show how the spin wave thermal fluctuations—even down to the quantum magnonic ground state—induce a measurable frequency shift of the paramagnetic spins in the bath. This shift results in a thermal dispersion force that can be measured optically and/or mechanically with a diamond mechanical resonator. In addition, we use our theory to compute the spin wave-mediated interaction between the spins in the bath. We show that all the above effects are measurable by state-of-the-art experiments. Our results provide the theoretical foundation for describing hybrid quantum systems of spin waves and spin baths and establish the potential of quantum spins as active control, sensing, and interfacing tools for spintronics.

DOI: [10.1103/PhysRevB.105.075410](https://doi.org/10.1103/PhysRevB.105.075410)**I. INTRODUCTION**

In the last years, spin waves have become the focus of intense research because of the following reasons. First, spin waves can be integrated into optical, microwave, and acoustic technological platforms [1–11]. Second, spin waves act as carriers for next-generation information processing in the field of magnon spintronics [12–16]. This is due to their low loss as compared to electronic currents, especially in ferromagnetic insulators (e.g., YIG—yttrium-iron-garnet) [14,17,18]. Third, spin waves, and their quanta (magnons) display a rich and tuneable phenomenology including exotic dispersion relations, nonreciprocity [14,19,20], room temperature Bose-Einstein condensation [21], and superfluidity [22]. These properties make spin waves very attractive in the context of hybrid quantum technologies [15,18,23].

In addition, recent experiments [24–31] have demonstrated the possibility of interfacing spin waves with solid-state paramagnetic spin baths. Inspired by this possibility, in this article we propose to explore the quantum phenomena stemming from the coupling between propagating fields (spin waves) and quantum emitters and their potential applications in magnonics. In particular, we will focus on the strong back-action exerted by ensembles of quantum emitters on fields and

vice versa. Such backaction has been demonstrated in many platforms in the optical domain, including dye molecules in plasmonics [32], rare earth impurities in optical fibers [33] and cold and Rydberg atoms in free space [34–36]. Harnessing a similar back-action for spin waves could, for instance, allow to dynamically mold the flow of spin currents without the need for material microstructuring in magnon spintronics. Furthermore and in analogy to plasmonics [37], a fundamental understanding of spin wave-paramagnetic spin interfaces could bring a new degree of control to spin wave-based hybrid technologies and enable applications in sensing [24,28,38], transduction [31,39], and computing [14,18,40–43].

In this paper, we provide a macroscopic quantum theory describing spin waves interacting with paramagnetic spin baths. We focus on paramagnetic spins with total spin $S = 1$. As a case study [Fig. 1(a)], we will consider nitrogen-vacancy (NV) centers in diamond in the vicinity of a YIG thin film in a parallel field configuration, although our model applies to a wide variety of magnetic structures. The choice of NVs is motivated by current experiments as well as their controllability [44] and potential for hybrid quantum technologies [24,45–54]. We apply open quantum systems theory to describe mutual back-action between the paramagnetic spin bath and the spin waves, and highlight two particular applications of relevance for magnonics. First, the tailoring of the spin wave propagation properties via their controlled coupling to the paramagnetic spin bath. In analogy to the back-action of

*c.gonzalez-ballester@uibk.ac.at

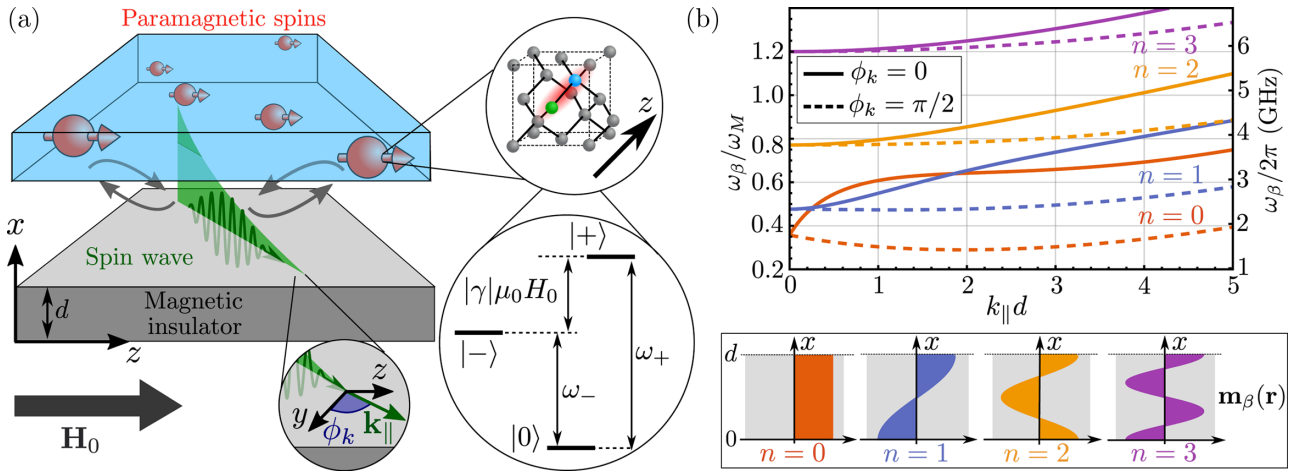


FIG. 1. (a) We consider paramagnetic spins with spin $S = 1$ in the vicinity of a magnetic insulator supporting spin waves. As a case study we focus on NV centers (upper inset) near a YIG thin film. The wave vector of the spin waves in the y - z plane is \mathbf{k}_{\parallel} . (b) Lowest four spin wave energy bands of a YIG film for the parameters in Table I and an applied field $\mu_0 H_0 = 20$ mT as a function of wave-vector modulus, for $\phi_k = 0$ (solid lines, Damon-Eshbach propagation) and $\phi_k = \pi/2$ (dashed lines, parallel propagation). The left and right axes show the spin wave frequency in units of $\omega_M \equiv |\gamma| \mu_0 M_S$ and in GHz, respectively. As indicated by the bottom panel, the band index n corresponds to the number of nodes of the magnetization mode function across the film thickness d .

quantum emitters on light, the spin bath simultaneously modifies the group velocity and the decay rate of spin waves enabling, among others, a net increase in propagation length. Second, a new method to probe spin waves based on their back-action on the paramagnetic spins. For both applications, our predictions rely on ensembles of maximally polarized (e.g., via optical pumping) NV centers with densities $\gtrsim 10^3 (\mu\text{m})^{-3}$, and can thus be tested with state-of-the-art experiments. Our theory allows us to understand and predict exhaustively the interaction between spin waves and paramagnetic spins, both at the classical and at the quantum levels.

This paper is organized as follows. First, we describe how we model the interaction of spin waves and a paramagnetic spin bath and summarize its coherent and dissipative dynamics in Sec. II. We then derive the effective spin wave dynamics induced by back-action of the paramagnetic spin bath in Sec. III and discuss the back-action-enabled possibility of modifying the spin wave spectrum and propagation features. In Sec. IV, we derive the effective dynamics of a paramagnetic spin under back-action of the spin waves and its potential as a novel probing method for spin waves. Our conclusions and outlook are in Sec. V. This paper is complemented by six exhaustive appendices including derivations and additional results. The quantization of the spin wave eigenmodes of a thin film, a detailed analysis of their properties, and the computation of the magnetic field power spectral densities outside the film are contained in Appendix A. Appendix B contains the analysis of the quantum dynamics of NV centers both at thermal equilibrium and under optical pumping. The derivation of the interaction between paramagnetic spins and spin waves is contained in Appendix C. In Appendix D, we summarize and give a practical formulation of the open quantum system approach to obtain effective equations of motion for a system coupled to a bath. We apply this procedure in the last two appendices; in Appendix E, we derive the spin wave induced effective dynamics of an ensemble of paramagnetic spins, and analyze in detail the modification of their lifetimes,

the induced frequency shifts and corresponding forces, and the induced coupling between different spins. In Appendix F, we derive the effective spin wave dynamics induced by a paramagnetic spin bath and study the modification of the magnetic field power spectral densities outside the film.

II. SYSTEM AND EQUATIONS OF MOTION

In this section, we summarize the Hamiltonian and the dissipative dynamics governing the coupled system formed by paramagnetic spins and spin waves. The density matrix of the total system obeys the von Neumann equation

$$\frac{d}{dt} \hat{\rho} = -\frac{i}{\hbar} [\hat{H}, \hat{\rho}] + \mathcal{D}_{\text{sw}}[\hat{\rho}] + \mathcal{D}_{\text{ps}}[\hat{\rho}]. \quad (1)$$

Here, the total Hamiltonian is written as a sum of three contributions,

$$\hat{H} = \hat{H}_{\text{sw}} + \hat{H}_{\text{ps}} + \hat{V}, \quad (2)$$

namely, the free Hamiltonian of the spin waves, the free Hamiltonian of the paramagnetic spins, and their interaction. The last two terms in Eq. (1) correspond to the independent dissipation of the spin waves and the paramagnetic spins. The detailed derivation of all the above terms is given in Appendices A–C. Let us summarize each of the contributions in Eq. (1) separately.

We first focus on the spin waves, namely, magnetization waves supported by a saturated ferromagnetic insulator. In the presence of a static field $\mathbf{H}_0 = H_0 \mathbf{e}_z$, a ferromagnetic insulator of arbitrary geometry acquires a magnetization field given by $\mathbf{M}(\mathbf{r}, t) = M_S \mathbf{e}_z + \mathbf{m}(\mathbf{r}, t)$, with M_S the saturation magnetization. The dynamical component $\mathbf{m}(\mathbf{r}, t)$ describes small oscillations ($|\mathbf{m}(\mathbf{r}, t)| \ll M_S$) above such fully magnetized state, namely, spin waves [20]. The quantum Hamiltonian of the spin waves, namely, the first contribution in Eq. (2), reads

$$\hat{H}_{\text{sw}} = \hbar \sum_{\beta} \omega_{\beta} \hat{s}_{\beta}^{\dagger} \hat{s}_{\beta}. \quad (3)$$

Here, β is a multi-index labeling all the spin wave eigenmodes supported by the ferromagnetic structure, ω_β the corresponding mode frequency, and \hat{s}_β^\dagger and \hat{s}_β are bosonic ladder operators which describe creation and annihilation of spin wave quanta (magnons) in eigenmode β .

Hereafter we focus on the particular magnetic structure depicted in Fig. 1(a), i.e., a YIG thin film infinitely extended on the y - z plane and occupying the region $0 \leq x \leq d$. The static magnetic field \mathbf{H}_0 is applied along a direction parallel to the film, a configuration chosen in most experiments as it gives rise to rich spin wave dynamics [25–30]. As shown in Appendix A, to derive \hat{H}_{sw} we first diagonalize the classical equations of motion for the spin waves, namely, the linearized Landau-Lifshitz equations in the magnetostatic approximation [20,55]. In this way, we obtain the corresponding eigenfrequencies ω_β and dimensionless magnetization eigenmodes $\mathbf{m}_\beta(\mathbf{r})$ analytically. We follow the approach in Refs. [56,57], where the exchange interaction is fully accounted for whereas the dipole-dipole interaction is included to first order in perturbation theory.

For the YIG film geometry under study, the spin wave eigenmodes and eigenfrequencies are fully characterized by five parameters, namely, the gyromagnetic ratio γ , the film thickness d , the applied field H_0 , the exchange stiffness α_x , and the saturation magnetization M_S or, equivalently, the natural frequency $\omega_M \equiv |\gamma|\mu_0 M_S$ [20]. The eigenmodes are labeled by three mode indices $\beta \equiv \{\mathbf{k}_\parallel, n\}$, namely, the wave vector on the film plane $\mathbf{k}_\parallel = k_\parallel[\mathbf{e}_y \cos(\phi_k) + \mathbf{e}_z \sin(\phi_k)]$ plus a discrete band index $n = 0, 1, 2, \dots$ indicating the number of nodes of the magnetization mode function across the film thickness, see Fig. 1(b). Among the many properties of the eigenmodes, three are of special interest regarding the interaction with paramagnetic spins: (i) the polarization of the magnetic field generated by a spin wave outside the film depends strongly on its propagation direction. As an example, a spin wave propagating in the Damon-Eshbach configuration [58,59], i.e., with wave vector $\mathbf{k}_\parallel = \pm k_\parallel \mathbf{e}_y$ or, equivalently, $\phi_k = 0$ or $\phi_k = \pi$, produces a circularly polarized field with polarization $\mathbf{e}_\mp \equiv (\mathbf{e}_x \mp i\mathbf{e}_y)/\sqrt{2}$ above the film and with the opposite polarization below it. (ii) The amplitude of the spin wave magnetic field can have different values above and below the film and, at certain values of \mathbf{k}_\parallel , can even completely vanish at one of the sides, a phenomenon known as *modal-profile nonreciprocity* [57,60]. (iii) Outside the film, the magnetic field amplitude of a spin wave decays exponentially as $\exp(-k_\parallel l)$, with l the absolute vertical separation from the surface of the film.

Once the classical eigenmodes have been obtained and characterized we quantize them [61] to obtain both the Hamiltonian (3) and the spin wave magnetization operator,

$$\hat{\mathbf{m}}(\mathbf{r}) = \sum_\beta \mathcal{M}_{0\beta} [\mathbf{m}_\beta(\mathbf{r}) \hat{s}_\beta + \text{H.c.}], \quad (4)$$

where

$$\mathcal{M}_{0\beta} \equiv \sqrt{\frac{\hbar |\gamma| M_S \omega_M}{2L^2 d \omega_\beta}} \quad (5)$$

TABLE I. Chosen values for the relevant parameters of YIG and of the NV centers across the main text. Note that other relevant parameters whose value is not fixed, such as the field H_0 or the distance l between the NV centers and the film, are not included in this table.

Parameter	Value
YIG film thickness	$d = 200 \text{ nm}$
YIG gyromagnetic ratio	$\gamma = -1.76 \times 10^{11} \text{ T}^{-1} \text{ s}^{-1}$
YIG magnetization	$M_S = 1.39 \times 10^5 \text{ A m}^{-1}$
YIG exchange stiffness	$\alpha_x = 2.14 \times 10^{-4} (\mu\text{m})^{-2}$
YIG Gilbert damping parameter	$\alpha_G = 10^{-4}$
NV zero-field splitting	$D_0 = 2\pi \times 2.877 \text{ GHz}$
NV gyromagnetic ratio	$\gamma_s = -1.76 \times 10^{11} \text{ T}^{-1} \text{ s}^{-1}$
NV occupation lifetime	$T_1 = 3 \text{ ms}$
NV coherence lifetime	$T_2^* = 1 \mu\text{s}$

is the zero-point magnetization [6,61,62], and $L \rightarrow \infty$ is a quantization length.¹

We now focus on the Hamiltonian of a single paramagnetic spin at a position \mathbf{r}_0 outside the magnetic structure and whose symmetry axis is oriented parallel to the z -axis, as depicted in Fig. 1(a). We describe the paramagnetic spin through the three states $|0\rangle$, $|+\rangle$, and $|-\rangle$ corresponding to the eigenstates of the spin operator \hat{S}_z with eigenvalue $m_S = 0, +\hbar$, and $-\hbar$, respectively. The Hamiltonian of the paramagnetic spin is [10,11,63–65]

$$\hat{H}_{\text{ps}} = \hbar^{-1} D_0 \hat{S}_z^2 + \omega_H \hat{S}_z = \hbar \sum_{\alpha=\pm} \omega_\alpha \hat{\sigma}_{\alpha\alpha}, \quad (6)$$

where we define the transition matrices $\hat{\sigma}_{\alpha\alpha'} \equiv |\alpha\rangle\langle\alpha'|$, and the frequencies $\omega_\pm \equiv D_0 \pm \omega_H$ and $\omega_H \equiv |\gamma_s| \mu_0 H_0$ with γ_s the gyromagnetic ratio of the spin and μ_0 the vacuum permeability. The first term in Eq. (6) describes the zero-field splitting between the $m_S = 0$ and the $m_S = \pm 1$ states, quantified by a rate D_0 . This splitting, absent in paramagnetic spins with $S = 1/2$, is crucial for tuning spin waves in resonance with the transitions of the paramagnetic spin. The second term in Eq. (6), proportional to ω_H , corresponds to the Zeeman splitting induced by the applied field H_0 between the levels $|\pm\rangle$, which are degenerate at zero field. The Hamiltonian (6) describes the dynamics of, among others, the spin-split ground-state manifold of negatively charged NV centers [10,11,63–65], with parameters given by Table I.

The third contribution in Eq. (2), namely, the interaction between the spin waves and the single paramagnetic spin at position \mathbf{r}_0 , stems from the magnetic dipole interaction:

$$\hat{V} = -\mu_0 \hat{\boldsymbol{\mu}}_{\text{ps}} \cdot [\hat{\mathbf{H}}(\mathbf{r}_0) - \mathbf{H}_0] \quad (7)$$

$$= \hbar \sum_\beta (g_\beta \hat{s}_\beta \hat{\sigma}_{-0} + \text{H.c.}) + \hat{S}_z \sum_{\beta\beta'} \tilde{g}_{\beta\beta'} \hat{s}_\beta^\dagger \hat{s}_{\beta'}, \quad (8)$$

with $\hat{\boldsymbol{\mu}}_{\text{ps}} = -|\gamma_s| \hat{\mathbf{S}}$ the magnetic dipole moment of the paramagnetic spin and $\hat{\mathbf{S}}$ its total spin operator. The field generated by the spin waves, $\hat{\mathbf{H}}(\mathbf{r}_0) - \mathbf{H}_0$, is given by the total magnetic

¹Note that, in analogy to the mode volume in quantum optics [90], no physical observable will depend on the quantization length L .

field operator minus the applied field \mathbf{H}_0 , whose interaction with the paramagnetic spin has already been included in the spin Hamiltonian Eq. (6). As detailed in Appendix C, the explicit expression in the second line of Eq. (7) is obtained by computing the spin wave magnetic field up to second order in magnon operators \hat{s}_β and \hat{s}_β^\dagger and undertaking a rotating wave approximation. The first contribution in Eq. (7) describes magnon-induced decay and absorption along the spin transition $|0\rangle \leftrightarrow |-\rangle$. It is characterized by a coupling rate

$$g_\beta \equiv \mu_0 |\gamma_s| \mathcal{M}_{0\beta} \int d^3 \mathbf{r} [\mathbf{e}_-^* \cdot \overline{\overline{\mathbf{G}}}(\mathbf{r}_0 - \mathbf{r}) \mathbf{m}_\beta(\mathbf{r})], \quad (9)$$

where $\overline{\overline{\mathbf{G}}}(\mathbf{r})$ is the magnetostatic Green's tensor of the film, defined and analytically computed in Appendix A. Within the rotating wave approximation, valid for $d \gtrsim 50$ nm and $\mu_0 H_0 \sim 10\text{--}35$ mT, the coupling between spin waves and the transition $|0\rangle \leftrightarrow |+\rangle$ can be neglected. The second contribution in Eq. (7) describes spin wave induced dephasing of the paramagnetic spins. Despite being of second order, this contribution, characterized by a coupling rate

$$\begin{aligned} \tilde{g}_{\beta\beta'} &= -\mu_0 |\gamma_s| \frac{\mathcal{M}_{0\beta} \mathcal{M}_{0\beta'}}{M_S} \int d^3 \mathbf{r} [\mathbf{m}_\beta^*(\mathbf{r}) \cdot \mathbf{m}_{\beta'}(\mathbf{r}) \\ &\quad \times \text{Re}[\mathbf{e}_z \cdot \overline{\overline{\mathbf{G}}}(\mathbf{r}_0 - \mathbf{r}) \mathbf{e}_z]], \end{aligned} \quad (10)$$

is resonant for an infinite set of magnon pairs $\{\beta, \beta'\}$. It can thus be as relevant as the first-order contribution which is resonant only for spin waves fulfilling $\omega_\beta = \omega_-$. This cumulative effect of second-order contributions has already been found to be relevant for e.g., acoustic phonon baths [66].

We now focus on the dissipative contributions to the von Neumann equation Eq. (1). We first consider the spin waves, which undergo dissipation through Gilbert damping [19,20,67]. Gilbert damping is modelled through the dissipator [68]

$$\mathcal{D}_{\text{sw}}[\hat{\rho}] = \sum_\beta \gamma_\beta (\bar{n}_\beta \mathcal{L}_{\hat{s}_\beta \hat{s}_\beta^\dagger}[\hat{\rho}] + (1 + \bar{n}_\beta) \mathcal{L}_{\hat{s}_\beta^\dagger \hat{s}_\beta}[\hat{\rho}]), \quad (11)$$

which describes absorption and decay into a thermal bath at temperature T , in terms of Lindblad superoperators defined as

$$\mathcal{L}_{\hat{a}\hat{b}}[\hat{\rho}] \equiv \hat{a}\hat{\rho}\hat{b} - \frac{1}{2}\{\hat{b}\hat{a}, \hat{\rho}\}, \quad (12)$$

with γ_β the magnon decay rate and $\bar{n}_\beta = [\exp(\hbar\omega_\beta/k_B T) - 1]^{-1}$ the Bose-Einstein distribution at the spin wave frequency. The magnon decay rate γ_β , typically in the \sim MHz range, is computed analytically using the expression from phenomenological loss theory [20,69,70],

$$\gamma_\beta = \frac{2\alpha_G \omega_\beta}{|\gamma| \mu_0} \frac{\partial \omega_\beta}{\partial H_0}, \quad (13)$$

which is known to be a good description of propagation loss in thin films and stripes [69]. Here, we have introduced the additional Gilbert damping parameter α_G characterizing the spin wave losses (see Table I).

The dissipation of the paramagnetic spin is modelled through the following dissipator [63–65,71]:

$$\begin{aligned} \mathcal{D}_{\text{ps}}[\hat{\rho}] &= \frac{\kappa_2}{\hbar^2} \mathcal{L}_{\hat{s}_z \hat{s}_z}[\hat{\rho}] + \kappa_1 \sum_{\alpha=\pm} \\ &\quad \times (\bar{n}_\alpha \mathcal{L}_{\hat{\sigma}_{\alpha 0} \hat{\sigma}_{\alpha 0}}[\hat{\rho}] + (\bar{n}_\alpha + 1) \mathcal{L}_{\hat{\sigma}_{\alpha 0} \hat{\sigma}_{\alpha 0}}[\hat{\rho}]). \end{aligned} \quad (14)$$

The first term above describes dephasing at a rate κ_2 , whereas the second line describes decay and absorption at a rate κ_1 along the two spin transitions, namely, $|0\rangle \leftrightarrow |\pm\rangle$, induced by a bosonic thermal reservoir at temperature T , with $\bar{n}_\alpha = [\exp(\hbar\omega_\alpha/k_B T) - 1]^{-1}$. The rates κ_1 and κ_2 are related to the experimentally measured values for the two decoherence timescales T_1 and T_2^* of the paramagnetic spin. These timescales are defined through the decay of the occupations $\langle \hat{\sigma}_{\alpha\alpha} \rangle \sim \exp(-t/T_1)$ ($\alpha = 0, \pm$) and the coherences $\langle \hat{\sigma}_{0\pm} \rangle \sim \exp(-t/T_2^*)$ in the zero-field limit $H_0 \rightarrow 0$ [71,72] and are given by

$$T_1^{-1} \equiv \kappa_1(1 + 3\bar{n}_0); \quad (T_2^*)^{-1} \equiv \frac{T_1^{-1} + \kappa_2}{2} \quad (15)$$

with $\bar{n}_0 = [\exp(\hbar D_0/k_B T) - 1]^{-1}$. For the specific case of NV centers these timescales typically lie on the range $T_1 \sim$ ms and $T_2^* \sim \mu$ s [28,63,72–75].²

The above expressions can be generalized to an ensemble of paramagnetic spins situated at positions \mathbf{r}_j , $j = 1, \dots, N$ (see Appendix C). We assume the density of paramagnetic spins is low enough such that the spins are independent from each other, that is, any interaction between them can be neglected. In the specific case of NV centers, this approximation holds for all the densities considered in this work (at most $10^5(\mu\text{m})^{-3}$) [76,77]. Under this assumption both the Hamiltonian and the dissipator of the paramagnetic spins are simply written as a sum of the independent Hamiltonian and dissipator, Eqs. (6) and (14), over all the spins in the ensemble. Furthermore, the above expressions can be extended to include external pumping of the paramagnetic spins, i.e., any mechanism whereby the spins are initialized near their ground state $|0\rangle$. This external pumping results in an enhancement of the mutual back-action between spin waves and paramagnetic spins as we will see below. A particular case, namely, the optical pumping of NV centers [44,78–83], is modelled and analyzed in detail in Appendix B 2.

In the following two sections, we study the back-action of the paramagnetic spins on the spin waves (Sec. III) and, conversely, the back-action of spin waves onto the paramagnetic spins (Sec. IV). In both cases, we follow the approach in open quantum systems [68], namely, we trace out the degrees of freedom of one component (the bath) in order to derive an effective equation of motion for the second component (the system). By doing so, we obtain a reduced master equation describing only the dynamics of the system degrees of freedom, and including the back-action of the bath in the form of effective dynamical terms such as additional dissipation or frequency shifts. This master equation allows to characterize the full dynamics of the system under the back-action of the bath. A brief general summary of the involved techniques and approximations is given in Appendix D.

We remark that, although here we focus on a specific geometry (YIG thin film in the parallel-field configuration), the

²Although, as indicated by Table I, throughout this work, we take $T_2^* = 1\mu$ s, this value can be significantly increased using isotopically pure samples [63,73] or dynamical decoupling techniques [44,63,74,75].

whole framework presented above and in the Appendices remains general. Indeed, our whole formalism relies only on two assumptions, namely, (i) the weak coupling approximation and (ii) the fast decay of the spin wave-generated magnetic field outside the magnetic material. Our formalism thus can be directly applied to almost every magnonic structure showing one-, two-, or three-dimensional confinement, either using the above Hamiltonian or its most general expression derived in Appendices A–C. Extension to arbitrarily high bias fields and even time-dependent external magnetic fields is straightforward using the results of, e.g., Ref. [84].

III. MODIFICATION OF THE SPIN WAVE PROPERTIES

The strong back-action experienced by optical frequency electromagnetic fields due to their interaction with high-density quantum emitter ensembles has been demonstrated in many different platforms [32–36]. For spin waves, however, the back-action of paramagnetic spins has remained practically unexplored and is not yet well understood, in spite of the significant advantages that an engineered back-action could provide for spintronics, from molding the flow of spin currents to patterning the spin waves without the need for material microstructuring. In this section, we derive and study the effective spin wave dynamics induced by a bath of paramagnetic spins and discuss its potential applications. The detailed derivation of the results in this section is provided in Appendix F.

We focus on the particular configuration depicted in Fig. 2(a), which is used in most experiments [25–27,29,30]. Specifically, we consider an ensemble of $N \gg 1$ identical paramagnetic spins³ hosted, at randomly distributed positions \mathbf{r}_j ($j = 1, \dots, N$), inside an infinite diamond slab parallel to the YIG film. The diamond slab has a width $l_2 - l_1$ and is placed at a height l_1 above the film. Under these assumptions, and after tracing out the bath of paramagnetic spins, we obtain the following master equation for the reduced density matrix of the spin waves, $\hat{\rho}_{\text{sw}}$:

$$\frac{d}{dt} \hat{\rho}_{\text{sw}} = -\frac{i}{\hbar} [\hat{H}'_{\text{sw}}, \hat{\rho}_{\text{sw}}] + \mathcal{D}_{\text{sw}}[\hat{\rho}_{\text{sw}}] + \mathcal{D}_c[\hat{\rho}_{\text{sw}}]. \quad (16)$$

The first term in Eq. (16) describes the modified spin wave Hamiltonian and includes a paramagnetic spin-induced frequency shift,

$$\hat{H}'_{\text{sw}} = \hbar \sum_{\beta} (\omega_{\beta} + \delta_{\beta}) \hat{s}_{\beta}^{\dagger} \hat{s}_{\beta} \equiv \hbar \sum_{\beta} \omega'_{\beta} \hat{s}_{\beta}^{\dagger} \hat{s}_{\beta}. \quad (17)$$

The dissipative part is composed by the original dissipator $\mathcal{D}_{\text{sw}}[\hat{\rho}]$, given by Eq. (11), and an additional absorption and decay for each spin wave mode,

$$\mathcal{D}_c[\hat{\rho}] \equiv \sum_{\beta} \Gamma_{d\beta} \mathcal{L}_{\hat{s}_{\beta}^{\dagger} \hat{s}_{\beta}}[\hat{\rho}] + \Gamma_{a\beta} \mathcal{L}_{\hat{s}_{\beta} \hat{s}_{\beta}^{\dagger}}[\hat{\rho}]. \quad (18)$$

³Our results can be directly extended to include spin-dependent frequencies and lifetimes, as well as to an arbitrary number and spatial distribution of paramagnetic spins. The latter extension is carried out in Appendix F where we show that, for a slab below the YIG film, the shifts δ_{β} and Γ_{β} are given by Eq. (20) under the substitution $\phi_k \rightarrow \phi_k + \pi$.

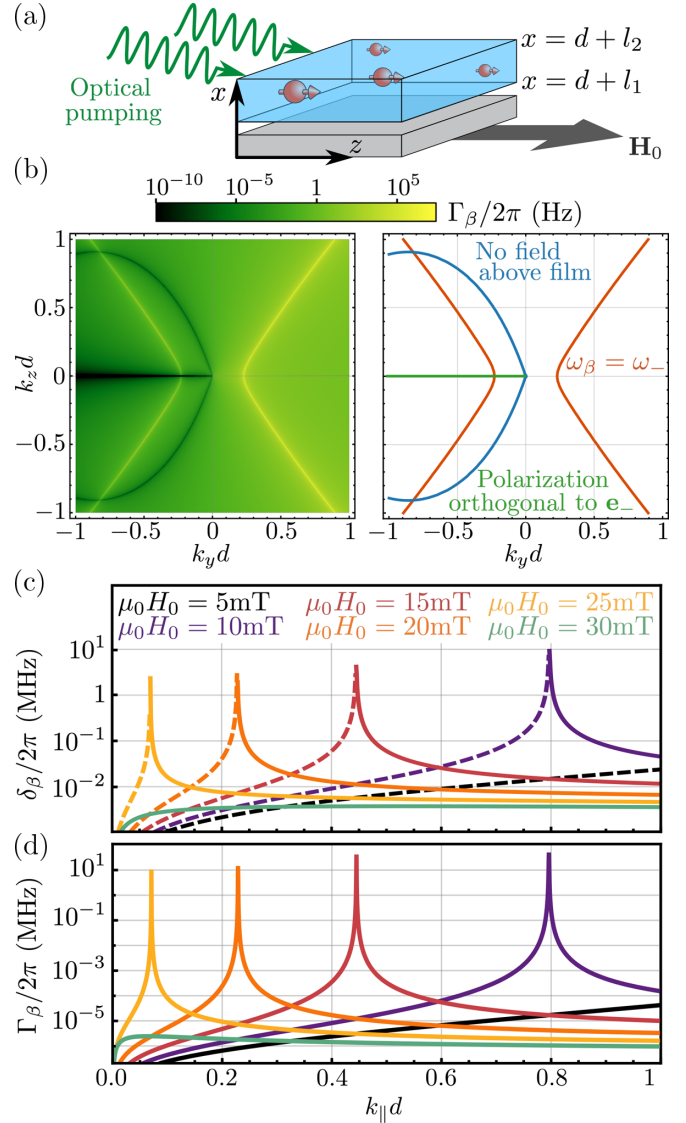


FIG. 2. (a) We study the effective dynamics of spin waves in the presence of a diamond slab containing optically pumped NV centers. (b) Left: increase of the linewidth of $n = 0$ spin waves at $\mu_0 H_0 = 20$ mT as a function of their parallel wave vector. Right: isolines corresponding to spin waves with $\omega_{\beta} = \omega_{-}$ (red), spin waves with polarization orthogonal to \mathbf{e}_{-} (green), and spin waves generating zero magnetic field above the film (blue). [(c) and (d)] Frequency and linewidth modification for $n = 0$ spin wave modes propagating along the $+y$ direction as a function of wave number, for different values of the applied field H_0 . Dashed and solid lines indicate negative and positive sign, respectively. In all the panels, we take $l_1 = 0$, $l_2 = \infty$, $\rho_{\text{nv}} = 10^4 \mu\text{m}^{-3}$, $T = 300$ K, optimum optical pumping parameters, and the parameters in Table I.

General expressions for the rates δ_{β} , $\Gamma_{d\beta}$, and $\Gamma_{a\beta}$ are given in Appendix F [see also Eq. (20)]. The above dissipator Eq. (18) results in an increase of the linewidth of the spin waves, namely,

$$\gamma_{\beta} \longrightarrow \gamma_{\beta} + \Gamma_{d\beta} - \Gamma_{a\beta} \equiv \gamma_{\beta} + \Gamma_{\beta}. \quad (19)$$

We remark that the full master equation includes an additional interaction between different spin wave modes. The corresponding coupling rates, as opposed to the shift δ_{β} and

the linewidth increase Γ_β , depend on the parallel coordinates (y_j, z_j) of each paramagnetic spin and can be shown to average out to zero in the limit of $N \gg 1$ randomly distributed paramagnetic spins.

The rates δ_β and Γ_β are given by

$$\begin{aligned} \begin{bmatrix} \delta_\beta \\ \Gamma_\beta \end{bmatrix} &= \langle \hat{\sigma}_{00} - \hat{\sigma}_{--} \rangle_{ss} \frac{\mu_0^2 |\gamma| \gamma_s^2 \hbar M_S \rho_{ps}}{\Delta_\beta^2 + (\kappa_T/2)^2} \begin{bmatrix} \Delta_\beta \\ \kappa_T \end{bmatrix} \\ &\times \frac{\cos^4(\phi_k/2)}{\omega_\beta/\omega_M} h_{\beta+0}^2 \int_{l_1/d}^{l_2/d} dx e^{-2(k_\parallel d)x}, \quad (20) \end{aligned}$$

where the subindex “ss” indicates the steady state of the paramagnetic spins and $h_{\beta+0}$ is a real and dimensionless mode amplitude of order unity, defined in Appendix A. In the above expression, we have defined the detuning $\Delta_\beta \equiv \omega_\beta - \omega_-$, the total decay rate of the paramagnetic spin coherence $\langle \hat{\sigma}_{0-} \rangle$, namely, $\kappa_T/2$, and the volumetric density of paramagnetic spins, $\rho_{ps} \equiv NL^{-2}(l_2 - l_1)^{-1}$. Note that although we take the limit $N, L \rightarrow \infty$, the density ρ_{ps} remains constant. For a given spin wave mode β , the rates in Eq. (20) are maximized in the thick slab limit $k_\parallel l_2 \gg 1$ which, for the parameters in this work, is effectively achieved at $l_2 \gtrsim 5 \mu\text{m}$. In this limit the rates decay exponentially with the slab-film distance l_1 , and are thus maximized for a slab lying directly on top of the YIG film ($l_1 = 0$). Furthermore, the rates δ_β and Γ_β depend crucially on the spin wave propagation direction through ϕ_k , its amplitude and polarization through the mode amplitude $h_{\beta+0}$, its frequency through the sharply peaked factor $[\Delta_\beta^2 + (\kappa_T/2)^2]^{-1}$, and temperature and spin pumping through the occupation factor $\langle \hat{\sigma}_{00} - \hat{\sigma}_{--} \rangle_{ss}$.

Let us analyze the shifts δ_β and Γ_β in detail for the fundamental spin wave band $n = 0$, where they are most relevant. We focus on the specific case of an ensemble of optically pumped NV centers, where $\kappa_T/2 = \kappa_1(1 + 2\bar{n}_- + \bar{n}_+)/2 + \kappa_2/2 + \Omega \approx [T_2^*]^{-1}$ with Ω the optical pumping rate, proportional to the pumping intensity (see Appendix B). These ensembles can reach NV center densities ρ_{nv} as high as $\rho_{nv} \sim 10^5 \mu\text{m}^{-3}$ [76,77,85,86] and even larger [87,88], although in such cases the extreme concentrations prove harmful for the coherence and decay times of NV centers. The shift Γ_β is shown in the left panel of Fig. 2(b) as a function of the wave vectors k_y and k_z , for an NV center density $\rho_{nv} = 10^4 \mu\text{m}^{-3}$. We assume optimal optical pumping conditions, i.e., maximally polarized NV centers, $\langle \hat{\sigma}_{00} - \hat{\sigma}_{--} \rangle_{ss} \approx 0.7$. The dark areas in Fig. 2(b), which indicate $\Gamma_\beta = 0$, correspond to spin waves that do not couple to the paramagnetic spin bath. This is certified by the green and blue curves in Fig. 2(b), right panel, which indicate, respectively, the spin wave modes whose polarization is orthogonal to that of the spin transition $|0\rangle \leftrightarrow |- \rangle$ and the spin wave modes whose field amplitude vanishes above the YIG film. Conversely, the sharp maxima displayed by Γ_β and indicated by yellow lines in the left panel of Fig. 2(b) stem from the factor $\kappa_T/[\Delta_\beta^2 + (\kappa_T/2)^2]^{-1}$ in Eq. (20) and occur for spin waves in resonance with the paramagnetic spin transition ($\Delta_\beta = 0$). This is evidenced by the red curves in the right panel of Fig. 2(b), which are isolines indicating the resonant spin wave condition $\Delta_\beta = 0$. The behavior of the frequency shift δ_β , not shown in the figure, is very similar to Fig. 2(b). In this case, however, the different dependence with the detuning, $\delta_\beta \propto \Delta_\beta/[\Delta_\beta^2 + (\kappa_T/2)^2]$, results in

two sharp extremal points, namely, a maximum and a minimum at $\omega_\beta = \omega_- + \kappa_T/2$ and $\omega_\beta = \omega_- - \kappa_T/2$, respectively. For spin waves exactly on resonance, $\omega_\beta = \omega_-$, the frequency shift is exactly zero. Finally, note that the spin waves that experience the largest shifts δ_β and Γ_β are the (\mathbf{e}_- -polarized) Damon-Eshbach modes propagating along the $+y$ direction ($\phi_k = 0$), for which the coupling to the paramagnetic spins is maximized. In the following we will focus on these modes.

Since the most relevant feature of the shifts δ_β and Γ_β is their sharp modifications for near-resonant spin waves, $\omega_\beta = \omega_-(H_0)$, these shifts depend critically on the applied magnetic field H_0 . This is illustrated in Figs. 2(c) and 2(d) where we display δ_β and Γ_β respectively for spin wave modes propagating along the $+y$ direction and for different values of the applied field. Both shifts are suppressed for large fields ($\mu_0 H_0 \gtrsim 30$ mT) as the resonance condition is never met [$\omega_\beta > \omega_- \forall \beta$, see e.g., Fig. 10(a)]. They are also suppressed at small fields ($\mu_0 H_0 \lesssim 5$ mT) as the resonance condition is met only for spin waves with large wave number k_\parallel , which are very weakly coupled to the paramagnetic spin transition due to their exponentially reduced magnetic field amplitude above the film [see the discussion above Eq. (A62)]. In Fig. 3(a), we display the maximum linewidth modification $\Gamma_{\beta,\text{max}} = \max_{k_\parallel} \Gamma_\beta|_{n=0}$ as a function of applied field H_0 for three values of the NV center density, both for optically pumped NV centers (solid lines) and for NV centers in the absence of optical pumping, i.e., at room temperature thermal equilibrium (dashed lines). The maximum frequency shift δ_β fulfills $\delta_{\beta,\text{max}} \approx \Gamma_{\beta,\text{max}}/4$.⁴ According to Fig. 3(a), the highest possible values for Γ_β are achieved for $\mu_0 H_0 \approx 10\text{--}15$ mT where the resonant spin waves have moderate wave numbers $k_\parallel d \sim 0.4\text{--}0.8$ [compare with Figs. 2(c) and 2(d)]. In the absence of pumping [dashed curves in Fig. 3(a)], the rate $\Gamma_{\beta,\text{max}}$ is largely suppressed as the NV transition is practically saturated, i.e., $\langle \hat{\sigma}_{00} - \hat{\sigma}_{--} \rangle_{ss} \approx 10^{-4}$. In this case, the maximum attainable value at large NV densities $\rho_{nv} \gtrsim 10^4 \mu\text{m}^{-3}$, $\Gamma_{\beta,\text{max}} \approx 2\pi \times 10\text{--}100$ kHz, represents at best a correction of $\sim 10\%$ to the bare spin wave linewidth $\gamma_\beta \approx 2\pi \times 600$ kHz, which is barely detectable. On the other hand, at optimal optical pumping conditions [solid curves in Fig. 3(a)], the NV centers are near their ground state and the change in the linewidth can be much larger, e.g., $\Gamma_{\beta,\text{max}} \approx 2\pi \times 20$ MHz $\approx 30\gamma_\beta$ at $\rho_{nv} = 10^4 \mu\text{m}^{-3}$. These results suggest that, in this regime, a significant modification of the spin wave properties should be observed.

To analyze the modification of the spin wave properties, we compute three characteristics particularly relevant for applications in spin wave based information processing [25,69], namely, the modified spin wave frequency $\omega'_\beta \equiv \omega_\beta + \delta_\beta$, the modified group velocity defined as $v_g \equiv \partial \omega'_\beta / \partial k_y$, and the propagation length defined as $l_\beta \equiv v_g \tau_\beta$, where $\tau_\beta = 2/(\gamma_\beta + \Gamma_\beta)$ is the spin wave lifetime. For the sake of illustration, we display in Fig. 3(b) both the frequency ω_β and the propagation length l_β in the absence of NV centers ($\rho_{nv} = 0$). In the presence of the paramagnetic spins, the spin wave properties experience strong modifications within

⁴This is to be expected from the ratio between the corresponding peaked functions appearing on Γ_β and δ_β , $\max[2a(x^2 + a^2)^{-1}] / \max[x(x^2 + a^2)^{-1}] = 4$.

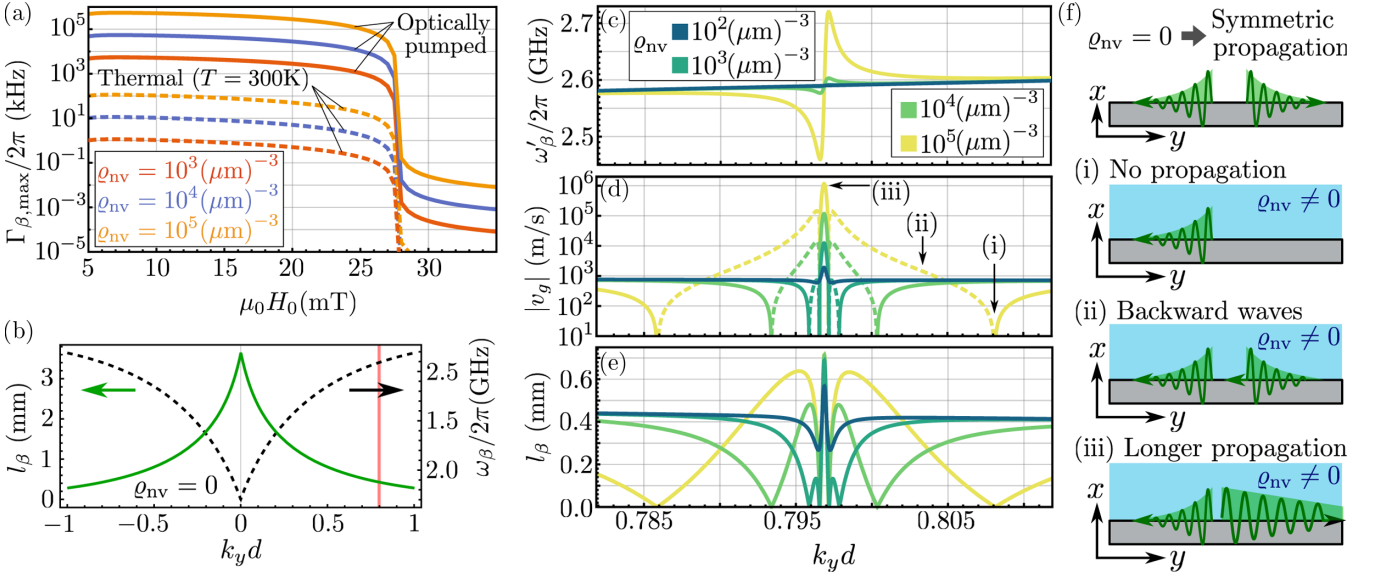


FIG. 3. (a) Maximum linewidth increase induced by optically pumped NV centers (assuming optimal pumping conditions, solid lines) and NV centers at room-temperature thermal equilibrium (dashed lines), as a function of applied field H_0 and for different densities of NV centers. (b) Propagation length (green) and dispersion relation (dashed black) of $n = 0$ Damon-Eshbach spin waves in the absence of NV centers. The red shaded area indicates the spin waves which are significantly affected by the NV centers. [(c)–(e)] Spin wave dispersion relation, absolute value of group velocity, and propagation length respectively, for optically pumped NV centers (optimal pumping conditions). The horizontal axis spans the red area indicated in (b), and different colors indicate different NV center densities. In (d), solid/dashed curves indicate positive/negative values of v_g . (f) Illustration of the modification of the spin wave properties induced by the NV centers, at the points (i), (ii), and (iii) marked in (d). In all the panels, we take $\mu_0 H_0 = 10$ mT, $l_1 = 0$, $l_2 = \infty$, and the parameters in Table I.

a narrow wave-number range [indicated by the red shaded area in Fig. 3(b)], corresponding to the frequency range $\omega_- - \kappa_T/2 \lesssim \omega_\beta \lesssim \omega_- + \kappa_T/2$. The spin wave frequencies, group velocities (in absolute value), and propagation lengths within this narrow range are shown in Figs. 3(c)–3(e), respectively, for different densities of NV centers. As evidenced by the figure, although the modification of the frequency ω'_β is relatively small ($\sim 4\%$), it displays very abrupt slope changes resulting in variations of several orders of magnitude in the group velocity. The propagation length does not display such a strong increase as the effective spin wave loss rate $\gamma_\beta + \Gamma_\beta$ becomes also very large.

Three especially interesting possibilities, schematically illustrated in Fig. 3(f), can be identified in Figs. 3(c)–3(e): (i) full suppression of spin wave propagation at wave numbers for which $v_g = l_\beta = 0$; (ii) backward-wave propagation [89] for a wide range of wave numbers where the group velocity becomes negative, $v_g < 0$; and (iii) enhancement of the propagation length by a factor up to $\sim 60\%$ for near-resonant spin waves, a value that can be extracted also from Fig. 3(e) as $l_{\beta,\max}/l_{\beta,\text{no NVs}} \approx l_{\beta,\max}/(l_\beta|_{k_y d=0.782}) \approx 1.63$. This enhancement of the propagation length, *a priori* counterintuitive due to the very large effective decay rate $\gamma_\beta + \Gamma_\beta$, is enabled by the corresponding increase in the group velocity. Note that all of these modifications occur for Damon-Eshbach modes propagating with $k_y > 0$, whereas the modes with $k_y < 0$ remain unchanged as their polarization is orthogonal to the paramagnetic spin transition [see Fig. 2(b)]. The presence of the paramagnetic spins as a bath thus induces, within a narrow but tuneable range of wave vectors, a further symmetry breaking for the Damon-Eshbach spin waves. The exotic phenomenology shown in Fig. 3 can be observed

experimentally using narrow-band spin wave excitation, i.e., spin wave sources able to excite quasi-monochromatic spin waves whose width in k space, (Δk_y) , is comparable to the narrow features of Figs. 3(c)–3(e). An example is the setup in Ref. [25], where a microwave stripline allows to excite spin waves with a spectral width of $(\Delta k_y) \lesssim 0.1(\mu\text{m})^{-1}$, and where NV photoluminescence enables detecting changes as small as $\sim 10\%$ in the spin wave propagation length. Similar or even stronger modifications of the propagation properties could be achieved with other paramagnetic spins (e.g., allowing for higher spin densities than NV center ensembles) and/or more efficient pumping schemes able to reach maximum polarization, $\langle \hat{\sigma}_{00} - \hat{\sigma}_{--} \rangle_{ss} \approx 1$.

IV. BACK-ACTION-BASED SPIN WAVE SENSING

The possibility of modifying spin wave properties through the passive back-action effected by the paramagnetic spins is far from the full potential of these spins for spintronics. Indeed, a natural step forward consists on using the paramagnetic spins as *active* components to probe and control spin waves [25–27,29–31]. An essential capability toward this goal is that of measuring the quantum back-action exerted by the spin waves on the paramagnetic spins. In this section, we characterize such back-action and show the possibility of detecting it both optically and mechanically, should the paramagnetic spins be embedded in a micromechanical oscillator (e.g., a diamond cantilever), see Fig. 4(a). Aside from spin wave probing, this optical and/or mechanical detection of spin wave back-action could allow for a new generation of flexible spin wave hybrid platforms integrating optical and mechanical degrees of freedom.

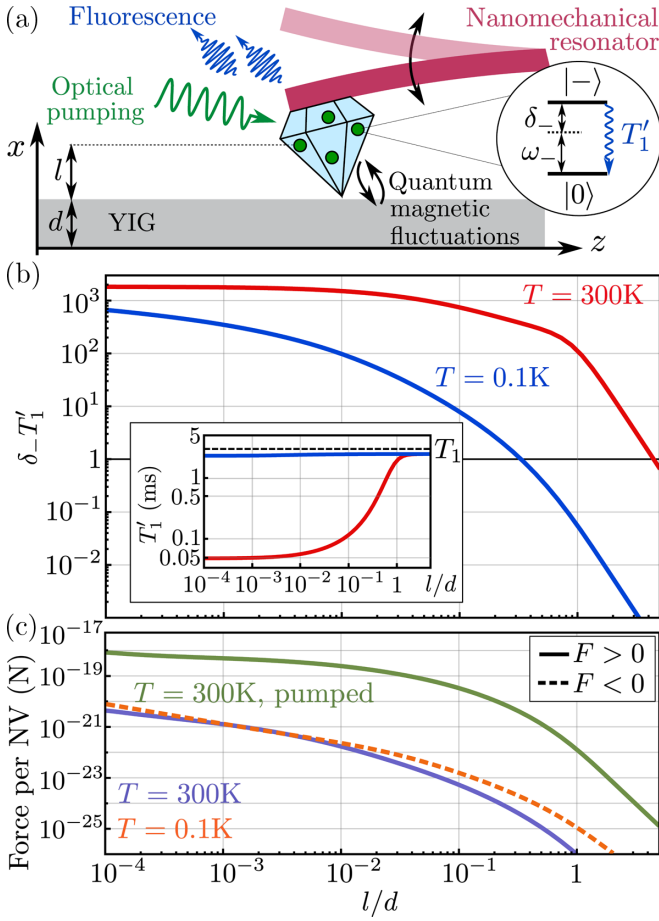


FIG. 4. (a) The spin waves modify the frequency and lifetime of the $|0\rangle \rightarrow |- \rangle$ transition of the (potentially optically pumped) NV centers. The frequency shift and corresponding force can be detected through fluorescence or nanomechanical force sensing. (b) Product of the frequency shift δ_- and the modified transition lifetime T'_1 of the $|0\rangle \leftrightarrow |- \rangle$ transition of a single NV center above the YIG film, at room (red) and cryogenic (blue) temperatures. The inset shows the corresponding modified lifetimes T'_1 , the dashed line indicating the bare lifetime in the absence of spin waves, T_1 . (c) Spin-wave induced force per NV center, at room temperature (purple), cryogenic temperature (dashed orange), and room temperature under optimal optical pumping conditions (green). Solid (dashed) lines indicate positive (negative) forces. In all panels, we choose $\mu_0 H_0 = 35$ mT and the parameters in Table I.

The spin wave back-action induces the following effective dynamics on an ensemble of paramagnetic spins: (i) a shift of the transition frequencies ω_{\pm} and a corresponding mechanical force, see details below; (ii) a modification of the lifetimes T_1 and T_2^* ; and (iii) an effective interaction between different paramagnetic spins, which inherits the direction-dependent character of the spin waves. All these effects are studied in detail in Appendix E. Hereafter we consider a single paramagnetic spin at an arbitrary position outside the YIG film. The resulting master equation for its reduced density matrix, $\hat{\rho}_{\text{ps}}$, is given by

$$\frac{d}{dt} \hat{\rho}_{\text{ps}} = -\frac{i}{\hbar} [\hat{H}'_{\text{ps}}, \hat{\rho}_{\text{ps}}] + \mathcal{D}_{\text{ps}}[\hat{\rho}_{\text{ps}}] + \mathcal{D}_{\text{d}}[\hat{\rho}_{\text{ps}}]. \quad (21)$$

The coherent contribution, given by the Hamiltonian

$$\hat{H}'_{\text{ps}} = \hbar \sum_{\alpha=\pm} (\omega_{\alpha} + \delta_{\alpha}) \hat{\sigma}_{\alpha\alpha}, \quad (22)$$

describes the modification of the two transition frequencies by a shift δ_{α} , in analogy to the AC Stark effect experienced by electric dipoles in an electromagnetic bath [90]. Although within our approximations the coupling between the transition $|0\rangle \rightarrow |+ \rangle$ and spin waves is neglected [see Eq. (7)], the frequency of this transition is also modified due to the energy shift of the state $|0\rangle$. Moreover, the spin waves introduce additional dissipative dynamics, given in Eq. (21) by the dissipator

$$\mathcal{D}_{\text{d}}[\hat{\rho}] = \kappa_a \mathcal{L}_{\hat{\sigma}_+ \hat{\sigma}_-}[\hat{\rho}] + \kappa_d \mathcal{L}_{\hat{\sigma}_- \hat{\sigma}_+}[\hat{\rho}] + \frac{\kappa'_2}{\hbar^2} \mathcal{L}_{\hat{s}_z \hat{s}_z}[\hat{\rho}]. \quad (23)$$

Here, the first two terms represent additional absorption and decay along the $|0\rangle \rightarrow |- \rangle$ transition, with rates κ_a and κ_d respectively, whereas the last term represents an additional dephasing of both excited states $|+ \rangle$ and $|- \rangle$ at a rate κ'_2 . Analytical expressions for the rates δ_{α} , κ_a , κ_d , and κ'_2 are given in Appendix E.

Let us discuss the frequency shifts δ_{\pm} . These shifts fulfill $|\delta_-| \geq 2|\delta_+|$,⁵ allowing us to focus on the main shift, namely, that of the coupled transition $|0\rangle \leftrightarrow |- \rangle$ given by

$$\delta_- = - \sum_{\beta} \frac{\Delta_{\beta}}{\Delta_{\beta}^2 + (\gamma_{\beta}/2)^2} |g_{\beta}|^2 (1 + 2\bar{n}_{\beta}). \quad (24)$$

The above frequency shift is measurable, for instance by fluorescence in the case of an NV center, provided that it is larger than the linewidth of the transition $|0\rangle \leftrightarrow |- \rangle$, i.e., provided that $|\delta_- T'_1| > 1$. Here, $T'_1 < T_1$ is the lifetime of the transition $|0\rangle \leftrightarrow |- \rangle$, which is also modified by the back-action of the spin waves. The definition of T'_1 is not straightforward since, in the presence of spin waves, the occupations $\langle \hat{\sigma}_{--} \rangle(t)$ do not obey a simple- but a multiexponential decay characterized by more than one rate.⁶ We define T'_1 as the shortest timescale of this evolution or, conversely, as the inverse of the largest decay rate. Both δ_- and T'_1 are computed numerically by expressing them in an integral form. In this form, it can be shown using symmetry arguments that both quantities are independent on the parallel (y, z) coordinates of the paramagnetic spin or on the side of the film on which the paramagnetic spin is placed, and are a function exclusively of the ratio l/d .

Let us consider the specific case of NV centers. The product $|\delta_- T'_1|$ for these paramagnetic spins is displayed in Fig. 4(b) as a function of vertical separation l/d , for $\mu_0 H_0 = 35$ mT and thermal equilibrium at room (red) and cryogenic (blue) temperatures. The corresponding inset shows the modified lifetime T'_1 for the same parameters. The spin wave induced effects are stronger both at room temperature and at short separations l , as the amplitude of the thermal spin waves is larger. At room temperature, the large values of δ_- (up to

⁵Specifically at room temperature $\delta_- \approx 2\delta_+$ whereas at cryogenic temperatures $\delta_+ \approx 0$.

⁶Adding to the difficulty, the rates associated to the decays of the two occupations $\langle \hat{\sigma}_{--} \rangle(t)$ and $\langle \hat{\sigma}_{++} \rangle(t)$ are generally different.

$\sim 2\pi \times 8$ MHz) are more significant than the reduction of the lifetime T_1' , resulting in a product $|\delta_- T_1'| > 1$ for NV-YIG film separations as large as $l = 4d = 800$ nm. This should allow for the experimental observation of the spin wave induced frequency shift of the transition $|0\rangle \leftrightarrow |- \rangle$ in current setups, e.g., via fluorescence of the NV center [24–31,72]. Note that the results in Fig. 4(b) do not require optical pumping of the NV centers. Moreover, as opposed to previous methods to detect highly populated spin wave states [25–31], this scheme focuses on measuring thermal—and even quantum, see below—spin wave fluctuations and thus does not require coherent spin wave driving. More details on the behavior of the frequency shift δ_- and of the lifetime T_1' , including their dependence with the applied field H_0 , are provided in Appendix E.

A consequence of a position-dependent frequency shift, that is, a position-dependent transition frequency, is the presence of a net force acting on the paramagnetic spin, namely, the magnetic thermal Casimir-Polder force [91] which has been extensively studied in quantum electrodynamics [91–93]. The net force experienced by a paramagnetic spin lying above the YIG film⁷ in its steady state is given by $\mathbf{F} = -\langle \nabla \hat{H}'_{ps} \rangle_{ss}$ [92,93]. Here we focus on the high- and low-temperature limits, where the force is given by the simpler expression

$$\mathbf{F} = -\mathbf{e}_x \frac{\hbar d\delta_-(l)}{2 dl} \times \begin{cases} \langle \hat{\sigma}_{--} - \hat{\sigma}_{00} \rangle_{ss} & \text{for } k_B T \gg \hbar\omega_M \\ 2\langle \hat{\sigma}_{--} \rangle_{ss} & \text{for } k_B T \ll \hbar\omega_M \end{cases} \quad (25)$$

Note the qualitative difference between room temperature, where both spin transitions contribute to the force ($\delta_+ \approx \delta_-/2$), and cryogenic temperatures where only the $|0\rangle \leftrightarrow |- \rangle$ transition does as $\delta_+ \rightarrow 0$. As opposed to the frequency shifts δ_{\pm} , the force depends on the state of the paramagnetic spin.

The force Eq. (25) is displayed in Fig. 4(c) for an NV center at $T = 300$ K under optimal optical pumping (green line), at $T = 300$ K without optical pumping (purple line), and at $T = 100$ mK without optical pumping (orange line). At thermal equilibrium at room temperature the force Eq. (25) is smaller, as the steady-state occupations are very close to their zero-field values, i.e., $\langle \hat{\sigma}_{\pm\pm} \rangle_{ss} \approx \langle \hat{\sigma}_{00} \rangle_{ss} \approx 1/3$. This force can, however, be increased by several orders of magnitude via optical pumping, as evidenced by the green curve in Fig. 4(c). At cryogenic temperatures [orange curve in Fig. 4(c)], despite the paramagnetic spin being close to its ground state, the force remains of the same order as at room temperature as the field amplitude of the thermal spin waves, and hence their back-action on the paramagnetic spins, is largely reduced. In this case, moreover, the force cannot be significantly increased via conventional optical pumping. The spin wave induced forces are mostly repulsive at room temperature, a well-known feature of fluctuational forces on magnetic dipole transitions [94,95], and attractive at cryogenic temperatures. A detailed analysis and characterization of all these forces,

including their dependence with the applied field H_0 , is given in Appendix E.

The possibility of pumping the paramagnetic spin paves the way toward the detection of the spin wave induced force at room temperature. Measurements of such force (and hence indirect measurements of the frequency shift) could be performed using nanomechanical sensing devices. For instance, a nanodiamond containing either a single NV center or an ensemble of NV centers could be attached to a high- Q cantilever as schematically depicted in Fig. 4(a).⁸ In this setup, the spin wave induced force could be tracked through the shifts in the mechanical frequency of the cantilever [51,96,97]. For a single, optically pumped NV center at a distance $l \lesssim d/5 \approx 40$ nm, the forces in Fig. 4(c) lie within the sensitivity range (10^{-21} – 10^{-18} N Hz^{1/2}) of current ultrasensitive force detectors, based on membranes [98–100] or nanowire resonators and cantilevers [101–107] of diverse materials, including single-crystal diamond [108]. Moreover, the additive force experienced by nano-diamonds containing ensembles of as few as $N \sim 10^3$ NV centers could reach current experimental sensitivities for NV centers at room- and cryogenic-temperature thermal equilibrium, allowing to measure magnonic ground-state quantum fluctuations. Even larger mechanical forces could be achieved for different paramagnetic spins and/or more efficient pumping schemes.

V. CONCLUSION

We have developed a comprehensive macroscopic quantum theory of hybrid interfaces based on spin waves magnetically coupled to paramagnetic spins. In the first part of our work, we have applied this theory to characterize the effective spin wave dynamics induced by the back-action of the paramagnetic spins. This back-action results in a tuneable modification of the spin wave propagation properties. Specifically, it can induce full cancellation or enhancement of spin wave propagation length, as well as backward wave propagation for Damon-Eshbach modes. All these modifications are strong and measurable in state of the art setups. We have also quantified the impact of the paramagnetic spins back-action on the magnetic field fluctuations, specifically on the magnetic field power spectral density, outside the magnetic structure. Our results show the potential of electron spins as passive tools to engineer spin wave properties.

In the second part of our work, we have studied the opposite effect, namely, the back-action exerted by spin waves on nearby paramagnetic spins. This back-action results in a frequency shift of the paramagnetic spins transitions, a modification of the paramagnetic spin decay and decoherence lifetimes, and a spin wave-mediated interaction between different paramagnetic spins within an ensemble. All the above effects have been characterized in detail. The frequency shift of single paramagnetic spins can be measured in current experiments, with usual fluorescence techniques. In addition,

⁷For a spin below the film the force has opposite sign, see Appendix E.

⁸We assume that the cantilever is in thermal equilibrium with the diamond slab and the magnetic film, so that our equilibrium-based modeling of the temperature-dependent NV decoherence rates remains valid.

this shift is accompanied by a force that can be detected with state of the art mechanical sensing devices. These results evidence the further role of paramagnetic spins as active tools for probing and controlling spin waves.

The results presented in this work have many applications in spin wave-based technologies. The suppression of the spin wave propagation lengths could be used to devise spin wave mirrors, polarization filters, optically gated spin wave transistors, or magnonic crystals, among others. Similarly, the enhancement of the spin wave propagation could help reduce losses in spin wave information processing devices. All these capabilities can in principle be spatially tailored with state of the art techniques, such as by distributing the paramagnetic spins in a convenient spatial arrangement [27–29] or by using selective optical pumping with nanometric resolution [109]. Our results could thus pave the way toward back-action-based reconfigurable spin wave circuits. On the other hand, the reverse back-action of spin waves on paramagnetic spins evidences their potential for spin wave detection and for accurate measurement of distances. Moreover, it paves the way toward using paramagnetic spins as mediators between spin waves and electromagnetic or mechanical fields. A particularly interesting prospect is to enhance the spin wave induced force (for instance, through coherent driving of spin waves resonant with the paramagnetic spin transition) hence increasing the magnetomechanical coupling between spin waves and a mechanical resonator. This magnetomechanical coupling, whose promising quantum applications are only starting to be explored [4,6,24,62,110–112], might allow to integrate magnonic degrees of freedom in micro- and optomechanical systems, bringing new degrees of flexibility to magnonic technological platforms.

ACKNOWLEDGMENTS

C.G.B. and O.R.I. acknowledge support from the European Union’s Horizon 2020 research and innovation programme under Grant Agreement No. [863132] (IQLev). T.S. acknowledges support from the Dutch Research Council (NWO) through the Projectruimte Grant No. 680.91.115 and from the Kavli Institute of Nanoscience Delft.

APPENDIX A: SPIN WAVES IN A SLAB

In this Appendix, we give further details on the spin waves supported by a thin film. First, in Appendix A 1, we describe the Landau-Lifshitz equation governing the magnetization dynamics and its linearization. We then derive, in Appendix A 2, the spin wave eigenmode equation and cast it in a convenient form for a perturbative treatment, which we summarize in Appendix A 3. After, we discuss the spin wave eigenmode properties in detail in Appendix A 4. We complete the introduction of the spin wave formalism in Appendix A 5 by summarizing the spin wave quantization, the introduction of loss rates, and the computation of spin wave observables. In the last two sections of this Appendix, we extend our study by computing and analyzing the magnetic field power spectral densities outside the film (Appendix A 6), and by computing the magnetization and magnetic field operators to second order in magnon operators (Appendix A 7), which are required in Appendix C.

1. Equations of motion and linearization

We consider first a lossless insulating ferromagnet in the presence of a static magnetic field \mathbf{H}_0 . The fundamental equation governing the dynamics of the magnetization field $\mathbf{M}(\mathbf{r}, t)$ is the lossless Landau-Lifshitz equation [20],

$$\frac{d}{dt}\mathbf{M}(\mathbf{r}, t) = -|\gamma|\mu_0\mathbf{M}(\mathbf{r}, t) \times [\mathbf{H}_0 + \mathbf{H}'(\mathbf{M}, \mathbf{r}, t)], \quad (\text{A1})$$

with γ the gyromagnetic ratio and μ_0 the vacuum permittivity. This equation is identical to the equation of motion for the orientation of a single fixed magnetic dipole with moment \mathbf{M} , except for the additional nonlinear contribution $\mathbf{H}'(\mathbf{M}, \mathbf{r}, t)$, known as the effective field, which describes the many complex interactions arising inside the magnetic material. The effective field can be written as [19,20]

$$\mathbf{H}'(\mathbf{M}, \mathbf{r}, t) = \mathbf{H}_d(\mathbf{M}, \mathbf{r}, t) + \mathbf{H}_x(\mathbf{M}, \mathbf{r}, t) + \mathbf{H}_a(\mathbf{M}, \mathbf{r}, t). \quad (\text{A2})$$

The first term above, namely, the demagnetizing field, accounts for the dipole-dipole interaction. Under the magnetostatic approximation $\nabla \times \mathbf{H}_d(\mathbf{r}, t) \approx 0$, valid for spin wave wavelengths much shorter or much longer than the vacuum wavelength [20], the demagnetizing field is given by [113]

$$\mathbf{H}_d(\mathbf{M}, \mathbf{r}, t) = \frac{1}{4\pi} \nabla \int d^3\mathbf{r}' \frac{\nabla' \cdot \mathbf{M}(\mathbf{r}', t)}{|\mathbf{r} - \mathbf{r}'|}. \quad (\text{A3})$$

The remaining two contributions in Eq. (A2) describe the effect of exchange and magnetocrystalline anisotropy on the magnetization dynamics. Since they are effective terms, they do not correspond to genuine Maxwell fields, i.e., the total field appearing in Maxwell equations is given by $\mathbf{H}(\mathbf{r}, t) = \mathbf{H}_0 + \mathbf{H}_d(\mathbf{M}, \mathbf{r}, t)$. On the one hand, the exchange field \mathbf{H}_x accounting for the exchange interaction is given, for a material with a cubic lattice such as YIG, by the expression [20]

$$\mathbf{H}_x(\mathbf{M}, \mathbf{r}, t) = \alpha_x \nabla^2 \mathbf{M}(\mathbf{r}, t) \quad (\text{A4})$$

with α_x the exchange stiffness. On the other hand, \mathbf{H}_a accounts for the magnetocrystalline anisotropy interaction, and its form is not only sample- and geometry-dependent but widely tunable e.g., through rare earth dopants [114,115]. For undoped YIG thin films, anisotropy is generally small [25,26,57,60] and can be neglected for describing spin waves. Hereafter we will thus take $\mathbf{H}_a \approx 0$, although the effect of different kinds of anisotropies, such as e.g., uniaxial or cubic, could be included [116].

From the definitions above it is evident that a homogeneous magnetization profile $\mathbf{M}(\mathbf{r}, t) = M_S \mathbf{e}_z$ is a solution of the Landau-Lifshitz equation Eq. (A1). We seek spin wave solutions, i.e., solutions describing small fluctuations above such fully magnetized state,

$$\mathbf{M}(\mathbf{r}, t) = M_S \mathbf{e}_z + \mathbf{m}(\mathbf{r}, t), \quad (\text{A5})$$

with $|\mathbf{m}(\mathbf{r}, t)| \ll M_S$. By introducing the above expression into Eq. (A1) and neglecting the small quadratic terms $\mathcal{O}(\mathbf{m}^2)$ we obtain the linearized Landau-Lifshitz equations, namely,

$$\left[\frac{d}{dt} - \mathbf{e}_z \times (\omega_H - \omega_M \alpha_x \nabla^2) \right] \mathbf{m}(\mathbf{r}, t) = -\omega_M \mathbf{e}_z \times \mathbf{h}(\mathbf{r}, t). \quad (\text{A6})$$

where, by definition, the magnetic field associated to the magnetization field $\mathbf{m}(\mathbf{r}, t)$, i.e., the magnetic field of the spin wave, is given by

$$\begin{aligned} \mathbf{h}(\mathbf{r}, t) &= \frac{1}{4\pi} \nabla \int d^3 \mathbf{r}' \frac{\nabla' \cdot \mathbf{m}(\mathbf{r}', t)}{|\mathbf{r} - \mathbf{r}'|} \\ &\equiv \int d^3 \mathbf{r}' \bar{\bar{\mathcal{G}}}(\mathbf{r} - \mathbf{r}') \mathbf{m}(\mathbf{r}', t). \end{aligned} \quad (\text{A7})$$

The Green's tensor above is defined as

$$\bar{\bar{\mathcal{G}}}_{ij}(\mathbf{r} - \mathbf{r}') = \frac{-1}{4\pi |\mathbf{r} - \mathbf{r}'|^3} (\mathbf{r} - \mathbf{r}')_i \frac{\partial}{\partial r'_j}, \quad (\text{A8})$$

where the subindices $i, j = x, y, z$ indicate Cartesian components. The above expression is usually symmetrized by (i) making use of the vector identity $\nabla \cdot (f\mathbf{A}) = f\nabla \cdot \mathbf{A} + (\nabla f) \cdot \mathbf{A}$ and integrating by parts; (ii) applying the divergence theorem, and (iii) taking an integration volume enclosed by an area infinitely far away from the magnetic material. The resulting symmetrized expression reads

$$\bar{\bar{\mathcal{G}}}_{ij}(\mathbf{r} - \mathbf{r}') = \frac{-1}{4\pi} \frac{\partial}{\partial r'_i} \frac{\partial}{\partial r'_j} \frac{1}{|\mathbf{r} - \mathbf{r}'|}. \quad (\text{A9})$$

It is convenient, given our planar geometry, to express the Green's tensor in a plane-wave representation in the parallel coordinates. Using the identity

$$\frac{1}{|\mathbf{r} - \mathbf{r}'|} = \frac{1}{2\pi} \int d^2 \mathbf{q}_{\parallel} \frac{e^{i\mathbf{q}_{\parallel}(\mathbf{r}_{\parallel} - \mathbf{r}'_{\parallel})}}{q_{\parallel}} e^{-q_{\parallel} |x - x'|}, \quad (\text{A10})$$

with $\mathbf{q}_{\parallel} \equiv q_y \mathbf{e}_y + q_z \mathbf{e}_z$ and $\mathbf{r}_{\parallel} \equiv y \mathbf{e}_y + z \mathbf{e}_z$, we can write the Green's tensor as

$$\begin{aligned} \bar{\bar{\mathcal{G}}}(\mathbf{r} - \mathbf{r}') &= -\frac{1}{8\pi^2} \int d^2 \mathbf{q}_{\parallel} e^{i\mathbf{q}_{\parallel}(\mathbf{r}_{\parallel} - \mathbf{r}'_{\parallel})} e^{-q_{\parallel} |x - x'|} \\ &\times \begin{bmatrix} 2\delta(x - x') - q_{\parallel} & -iq_y \xi_{xx'} & -iq_z \xi_{xx'} \\ -iq_y \xi_{xx'} & q_y^2 / q_{\parallel} & q_y q_z / q_{\parallel} \\ -iq_z \xi_{xx'} & q_y q_z / q_{\parallel} & q_z^2 / q_{\parallel} \end{bmatrix}, \end{aligned} \quad (\text{A11})$$

where $\xi_{xx'} \equiv \text{sign}[x - x']$. Note that the above expression is still general, but expressed in a convenient form for a film.

The linearized Landau-Lifshitz equations Eq. (A6) together with the magnetostatic relation Eq. (A7) forms an integro-differential equation for the magnetization field $\mathbf{m}(\mathbf{r}, t)$. It is complemented by two sets of boundary conditions. On the one hand, the usual Maxwell boundary conditions, namely, the continuity of $\mathbf{e}_z \times \mathbf{h}(\mathbf{r}, t)$ and of $\mathbf{e}_z \cdot \mathbf{b}(\mathbf{r}, t) \equiv \mu_0 \mathbf{e}_z \cdot [\mathbf{h}(\mathbf{r}, t) + \mathbf{m}(\mathbf{r}, t)]$ across the two film boundaries (in our thin film geometry, at $x = 0$ and $x = d$). On the other hand, the boundary conditions imposed by the exchange interaction, which are geometry- and material-dependent. We choose free-pinning boundary conditions [61,117],

$$\left. \frac{\partial}{\partial x} \mathbf{m}(\mathbf{r}, t) \right|_{x=0,d} = 0, \quad (\text{A12})$$

which are best suited to thin films with $d \lesssim 500$ nm [118]. Our results can be generalized to other pinning conditions [57–59] with little change in the final mode structure, especially for thin films [60,119–123]. In some limiting cases the above integro-differential equation can be solved easily,

for instance when exchange is negligible (dipolar spin waves, corresponding to $\alpha_x \ll \lambda_{\text{sw}}^2$, with λ_{sw}^2 the wavelength of the spin wave) or when it largely dominates over the dipole-dipole interaction (exchange waves, $\alpha_x \gg \lambda_{\text{sw}}^2$). However, in many structures, including the thin films under study, both exchange and dipole-dipole interaction are relevant and their competition is responsible for the complex phenomenology of the so-called magnetostatic dipole-exchange spin waves [58,59].

2. Eigenmode equation

The dipole-exchange eigenmodes of the linearized Landau-Lifshitz equation Eq. (A6) can be computed in different forms [58,59], even exactly [120,121], although the exact solution is numerically demanding. Here we follow the perturbative approach by Kalinikos in Ref. [57] (see also Refs. [56,60,123]). The first part of the derivation consists on manipulating the equations into a suitable form for the perturbative expansion. We start by decomposing the magnetization field in terms of eigenmodes,

$$\mathbf{m}(\mathbf{r}, t) = \sum_{\beta} \mathbf{m}_{\beta}(\mathbf{r}) e^{-i\omega t} + \text{c.c.} \quad (\text{A13})$$

and making use of the translational invariance to write the magnetization mode functions as

$$\mathbf{m}_{\beta}(\mathbf{r}) = \mathbf{m}_{\beta}(x) e^{i\mathbf{k}_{\parallel} \mathbf{r}_{\parallel}}. \quad (\text{A14})$$

By introducing the above expressions into Eq. (A7) and using the Green's tensor Eq. (A11) we find the same dependence for the associated field of the spin waves, namely,

$$\mathbf{h}(\mathbf{r}, t) = \sum_{\beta} \mathbf{h}_{\beta}(\mathbf{r}) e^{-i\omega t} + \text{c.c.} \quad (\text{A15})$$

with

$$\mathbf{h}_{\beta}(\mathbf{r}) = \mathbf{h}_{\beta}(x) e^{i\mathbf{k}_{\parallel} \mathbf{r}_{\parallel}}, \quad (\text{A16})$$

and the following one-dimensional relation between the transverse profiles,

$$\mathbf{h}_{\beta}(x) = \int_0^d dx' \bar{\bar{\mathcal{G}}}_0(x - x') \mathbf{m}_{\beta}(x'). \quad (\text{A17})$$

The one-dimensional Green's function of the slab can be calculated by direct integration and reads

$$\begin{aligned} \bar{\bar{\mathcal{G}}}_0(x - x') &= \frac{e^{-k_{\parallel} |x - x'|}}{2} \\ &\times \begin{bmatrix} k_{\parallel} - 2\delta(x - x') & -ik_y \xi_{xx'} & -ik_z \xi_{xx'} \\ -ik_y \xi_{xx'} & -k_y^2 / k_{\parallel} & -k_y k_z / k_{\parallel} \\ -ik_z \xi_{xx'} & -k_y k_z / k_{\parallel} & -k_z^2 / k_{\parallel} \end{bmatrix}. \end{aligned} \quad (\text{A18})$$

Using the above relations, the linearized Landau-Lifshitz equation Eq. (A6) can be cast as the following matrix equation for the two-dimensional vector $\mathbf{m}_{\beta}(x) = m_{\beta x}(x) \mathbf{e}_x + m_{\beta y}(x) \mathbf{e}_y$:

$$\hat{N} \mathbf{m}_{\beta}(x) = i \frac{\omega}{\omega_M} \bar{\bar{T}} \mathbf{m}_{\beta}(x) + \int_0^d dx' \bar{\bar{\mathcal{G}}}_0(x - x') \mathbf{m}_{\beta}(x') \quad (\text{A19})$$

where we define the linear operator

$$\hat{N} \equiv \left[\frac{\omega_H}{\omega_M} + \alpha_x k_{\parallel}^2 - \alpha_x \frac{\partial^2}{\partial x^2} \right] \mathbb{1}_{3 \times 3} \quad (\text{A20})$$

and the matrix

$$\overline{\overline{T}} \equiv \begin{bmatrix} 0 & -1 & 0 \\ 1 & 0 & 0 \\ 0 & 0 & 0 \end{bmatrix}. \quad (\text{A21})$$

Note that the equations do not couple modes with different values of \mathbf{k}_{\parallel} , thus confirming that the parallel wave vector is a good mode index. The above system is combined with the free-spin boundary conditions

$$\partial_x \mathbf{m}_{\beta}(x)|_{x=0,d} = 0. \quad (\text{A22})$$

In the above form, the problem has been reduced from a four-variable (\mathbf{r}, t) to a one-variable (x) integro-differential equation.

The second step is to transform the above simplified integro-differential equation Eq. (A19) into a system of algebraic equations, by expressing it in a suitable orthogonal basis. Since in thin films exchange interaction is the most relevant, we choose as a basis the vector eigenmodes of the operator \hat{N} that satisfy the free-spin boundary conditions, i.e., $\mathbf{S}_n^p(x) = S_n(x)\mathbf{e}_p$ ($p = x, y$) with

$$S_n(x) \equiv \sqrt{\frac{2}{(1 + \delta_{n0})}} \cos\left(n\pi \frac{x}{d}\right). \quad (\text{A23})$$

It can be easily checked that the above functions are eigenmodes of \hat{N} with eigenvalue

$$N_n(k_{\parallel}) \equiv \frac{\omega_H}{\omega_M} + \alpha_x \left[k_{\parallel}^2 + \left(\frac{n\pi}{d}\right)^2 \right], \quad (\text{A24})$$

that they fulfill the boundary conditions Eq. (A22), and that they form an orthogonal basis and are normalized to the film thickness d ,

$$\int_0^d dx \mathbf{S}_n^p(x) \cdot \mathbf{S}_{n'}^{p'}(x) = d \delta_{nn'} \delta_{pp'}. \quad (\text{A25})$$

We now expand the magnetization vector in this basis as

$$\mathbf{m}_{\beta}(x) = \sum_n m_n^x \mathbf{S}_n^x(x) + m_n^y \mathbf{S}_n^y(x), \quad (\text{A26})$$

and seek an equation for the unknown two mode amplitudes $\mathbf{m}_n \equiv (m_n^x, m_n^y)^T$. Specifically, by using the orthogonality relation between the basis elements, we cast the integrodifferential equation Eq. (A19) into an infinite algebraic system of coupled equations for the amplitude vectors:

$$\overline{\overline{D}}^{(nm)} \mathbf{m}_n + \sum_{n' \neq n} \overline{\overline{R}}^{(nn')} \mathbf{m}_{n'} = 0, \quad (\text{A27})$$

where the 2×2 matrices above, which depend on the parallel wave vector \mathbf{k}_{\parallel} , are given by

$$\overline{\overline{D}}^{(nm)} = \begin{bmatrix} N_n(k_{\parallel}) - \Gamma_{nn}^{xx} & -\Gamma_{nn}^{xy} + i(\omega/\omega_M) \\ -\Gamma_{nn}^{yx} - i(\omega/\omega_M) & N_n(k_{\parallel}) - \Gamma_{nn}^{yy} \end{bmatrix}, \quad (\text{A28})$$

$$\overline{\overline{R}}^{(nn')} = \begin{bmatrix} -\Gamma_{nn'}^{xx} & -\Gamma_{nn'}^{xy} \\ -\Gamma_{nn'}^{yx} & -\Gamma_{nn'}^{yy} \end{bmatrix} \quad (\text{A29})$$

Note that the subindices n and n' in the matrices $\overline{\overline{D}}^{(nm)}$ and $\overline{\overline{R}}^{(nn')}$ are mode labels and do not represent the matrix indices. In the above expressions,

$$\Gamma_{nn'}^{pp'}(\mathbf{k}_{\parallel}) \equiv \frac{1}{d} \int_0^d dx \int_0^d dx' S_n(x) S_{n'}(x') \mathcal{G}_0^{pp'}(x - x') \quad (\text{A30})$$

represents the dipole-dipole interaction term expanded in the basis $\mathbf{S}_n^p(x)$. The dipole-dipole interaction appears in both matrices $\overline{\overline{D}}^{(nm)}$ and $\overline{\overline{R}}^{(nn')}$. On $\overline{\overline{D}}^{(nm)}$, it accounts for the self-dipole-dipole interaction of each eigenmode of \hat{N} . This contribution is important and will be taken into account fully, i.e., nonperturbatively. Conversely, the dipole-dipole interaction between different eigenmodes of \hat{N} is fully captured by the term $\overline{\overline{R}}^{(nn')}$ and will be treated perturbatively.

3. Perturbative eigenmode calculation

Let us briefly sketch the perturbative treatment of the above system of equations. By combining all the two-dimensional vectors \mathbf{m}_n into an infinite-dimensional vector $\mathcal{M} \equiv (\mathbf{m}_0, \mathbf{m}_1, \dots)^T$, we can cast the system of equations Eq. (A27) as

$$\mathcal{L} \mathcal{M} = 0, \quad (\text{A31})$$

where \mathcal{L} is an infinite-dimensional matrix. Note that throughout this section we reserve the double-bar tensor notation $(*)$ for 2×2 matrices for the sake of clarity. The 2×2 block entries of the matrix \mathcal{L} are given by

$$\overline{\overline{\mathcal{L}}}_{\{nn'\}} = \delta_{nn'} \overline{\overline{D}}^{(nm)} + (1 - \delta_{nn'}) \overline{\overline{R}}^{(nn')}. \quad (\text{A32})$$

Here, the indices given inside curly brackets denote 2×2 block entries, i.e., $\overline{\overline{\mathcal{L}}}_{\{nn'\}}$ is the 2×2 matrix occupying the $\{n, n'\}$ block of \mathcal{L} . The spin wave eigenmodes are in general a linear combination of all the modes \mathbf{m}_n . Their dispersion relations are given by the implicit equation

$$\det[\mathcal{L}] = 0. \quad (\text{A33})$$

We aim at keeping the diagonal 2×2 block entries of Eq. (A32) as our unperturbed matrix, and apply perturbation theory to include the blocks $\overline{\overline{R}}^{(nn')}$. We will do this through block-diagonalization.

Let us assume it is possible to block-diagonalize the matrix \mathcal{L} , i.e., that we can solve the following generalized block eigenvalue equation:

$$\mathcal{L} |\mathbf{V}_{l\alpha}\rangle = \Lambda_l |\mathbf{V}_{l\alpha}\rangle. \quad (\text{A34})$$

Here, l is an index labeling the block eigenvalues and the block eigenvectors. We define the infinite block-diagonal matrix Λ_l , whose 2×2 block entries are given by

$$\overline{\overline{[\Lambda_l]}}_{\{ij\}} = \delta_{ij} \overline{\overline{\lambda}}_l, \quad (\text{A35})$$

i.e., the diagonal blocks are all identical and equal to the 2×2 eigenblock $\overline{\overline{\lambda}}_l$. The block eigenvectors $|\mathbf{V}_{l\alpha}\rangle$, expressed in Dirac notation for convenience, are matrices formed by 2 infinite column vectors. Because in a block diagonalization there might be more than one linearly independent vector

corresponding to the same block eigenvalue, we have introduced an auxiliary index α labeling all the eigenvectors within each manifold l . If the block eigenvalue problem Eq. (A34) is solved, one can transform the coefficient matrix of our system of equations into a block-diagonal form,

$$\mathcal{L} \longrightarrow \mathcal{L}'. \quad (\text{A36})$$

The block 2×2 entries of the block-diagonal matrix \mathcal{L}' are given by

$$\overline{\overline{\mathcal{L}'}}_{\{ll\}} = \delta_{ll'} \overline{\overline{\lambda}}_l. \quad (\text{A37})$$

Due to this convenient structure the dispersion relations for the eigenmodes, Eq. (A33), are easily obtained as the determinant factorizes into a product of determinants of 2×2 matrices:

$$\det[\mathcal{L}] = \det[\mathcal{L}'] = \prod_{l=0}^{\infty} \det[\overline{\overline{\lambda}}_l] = 0. \quad (\text{A38})$$

Moreover, we can identify l as an additional good mode index labeling the eigenmodes. The magnetization mode functions corresponding to mode l can analogously be computed from the corresponding eigenvectors, $|\mathbf{V}_{l\alpha}\rangle$. The problem of finding the spin wave eigenmodes and eigenfrequencies is thus reduced to block-diagonalizing the original matrix \mathcal{L} .

The block-diagonalization of the matrix \mathcal{L} is carried out by dividing it into an unperturbed diagonal part \mathcal{L}_d and an off-diagonal perturbation \mathcal{L}_o , given in block form by

$$\overline{\overline{[\mathcal{L}_d]}}_{\{nm'\}} = \delta_{nm} \overline{\overline{D}}^{(nm)}, \quad (\text{A39})$$

$$\overline{\overline{[\mathcal{L}_o]}}_{\{nm'\}} = (1 - \delta_{nm'}) \overline{\overline{R}}^{(nm')}. \quad (\text{A40})$$

The diagonal part is already in a block-diagonal form, and hence the zeroth-order solution in the perturbation $\overline{\overline{R}}^{(nm')}$, namely, the block-eigenvalue matrix $\Lambda_l^{(0)}$, is simply given by

$$\overline{\overline{[\Lambda_l^{(0)}]}}_{\{ij\}} = \delta_{ij} \overline{\overline{\lambda}}_l^{(0)} = \delta_{ij} \overline{\overline{D}}^{(ll)}. \quad (\text{A41})$$

The zeroth-order block eigenvectors are similarly given by $|\mathbf{V}_{l\alpha}^{(0)}\rangle = (\overline{\overline{0}}, \overline{\overline{0}}, \dots, \overline{\overline{V}}_{l\alpha}^{(0)})^T$, i.e., they are zero except for a 2×2 block matrix at position l . Since this matrix is arbitrary we can identify four linearly independent block eigenvectors labeled by the index $\alpha = 1, \dots, 4$. Hereafter and for simplicity, we choose these eigenvectors such that they form an orthonormal basis according to the inner product

$$\langle \mathbf{V}_{l\alpha}^{(0)} | \mathbf{V}_{l'\beta}^{(0)} \rangle \equiv \text{Tr}(\overline{\overline{0}}, \overline{\overline{0}}, \dots, \overline{\overline{V}}_{l\alpha}^{(0)\dagger}, \dots) \begin{pmatrix} \overline{\overline{0}} \\ \vdots \\ \overline{\overline{V}}_{l'\beta}^{(0)} \\ \vdots \end{pmatrix} = \delta_{ll'} \delta_{\alpha\beta}. \quad (\text{A42})$$

Note that the above condition amounts to choosing the matrices $\overline{\overline{V}}_{l\alpha}^{(0)}$ to form an orthonormal basis in the space of complex 2×2 matrices.

Once the above orthogonality relations and the zeroth-order solution are defined, we can proceed in an analogous

way as in usual perturbation theory. First, we expand the block-diagonalization equation (A34) in orders of the perturbation as

$$(\mathcal{L}_d + \mathcal{L}_o)(|\mathbf{V}_{l\alpha}^{(0)}\rangle + |\mathbf{V}_{l\alpha}^{(1)}\rangle + \dots) = (\Lambda_l^{(0)} + \Lambda_l^{(1)} + \Lambda_l^{(2)} \dots)(|\mathbf{V}_{l\alpha}^{(0)}\rangle + |\mathbf{V}_{l\alpha}^{(1)}\rangle \dots), \quad (\text{A43})$$

where the terms with super-index n are of n th order. To obtain the first-order correction to the equation, we discard all the terms of order 2 or larger, obtaining

$$\mathcal{L}_d |\mathbf{V}_{l\alpha}^{(1)}\rangle + \mathcal{L}_o |\mathbf{V}_{l\alpha}^{(0)}\rangle = \Lambda_l^{(0)} |\mathbf{V}_{l\alpha}^{(1)}\rangle + \Lambda_l^{(1)} |\mathbf{V}_{l\alpha}^{(0)}\rangle. \quad (\text{A44})$$

We can now overlap on the left with $\langle \mathbf{V}_{l\beta}^{(0)} |$ and use the hermiticity properties of the zeroth-order solution and the orthogonality relation (A42) to obtain

$$\langle \mathbf{V}_{l\beta}^{(0)} | \Lambda_l^{(1)} | \mathbf{V}_{l\alpha}^{(0)} \rangle = \langle \mathbf{V}_{l\beta}^{(0)} | \mathcal{L}_o | \mathbf{V}_{l\alpha}^{(0)} \rangle = 0, \quad (\text{A45})$$

where the last equality stems from the block-off-diagonal character of \mathcal{L}_o . Since the above equation holds for any α and β and the matrices $\overline{\overline{V}}_{l\alpha}^{(0)}$ form an orthonormal basis, we conclude that the first-order correction to the block eigenvalues is zero,

$$\Lambda_l^{(1)} = 0 \rightarrow \overline{\overline{\lambda}}_l^{(1)} = \overline{\overline{0}}. \quad (\text{A46})$$

By following the usual route in perturbation theory, one can easily find the first correction to the eigenvectors as

$$|\mathbf{V}_{l\alpha}^{(1)}\rangle = \sum_{l' \neq l, \beta} \frac{\langle \mathbf{V}_{l'\beta}^{(0)} | \mathcal{L}_o | \mathbf{V}_{l\alpha}^{(0)} \rangle}{\det[\overline{\overline{D}}^{(ll)}] - \det[\overline{\overline{D}}^{(l'l')}] } |\mathbf{V}_{l'\beta}^{(0)}\rangle. \quad (\text{A47})$$

In a similar way, it is possible to obtain eigenvalues and eigenvectors up to any order in perturbation theory [57].

4. Mode properties

To describe the properties of the spin waves in thin films, where exchange interaction dominates over dipole-dipole coupling, it is usually sufficient to include the dipole-dipole coupling up to first order in perturbation theory [25,26,57,58]. Here, since the first-order correction to the block eigenvalues is zero, the eigenfrequency equation reads

$$\det[\mathcal{L}'] = \prod_{n=0}^{\infty} \det[\overline{\overline{D}}^{(nn)}] = 0 + \mathcal{O}([\overline{\overline{R}}^{(nm')}]^2), \quad (\text{A48})$$

and hence we can still identify the index n introduced in Eq. (A23) as a good mode index labeling different spin wave bands. We can now group the three mode indices of a spin wave, namely, n and the parallel wave vector \mathbf{k}_{\parallel} , into a single compound index

$$\beta \equiv \{n, \mathbf{k}_{\parallel}\}. \quad (\text{A49})$$

The dispersion relation of band n is given by

$$\det[\overline{\overline{D}}^{(nn)}] = \det \begin{bmatrix} v_{\beta x} & i\omega/\omega_M \\ -i\omega/\omega_M & v_{\beta y} \end{bmatrix} = 0. \quad (\text{A50})$$

Here, we have used the expression of the matrix $\overline{\overline{D}}^{(nm)}$ Eq. (A28) and calculated the elements $\Gamma_{nm}^{pp'}$ [Eq. (A30)] explicitly. Specifically, $\Gamma_{nm}^{xy} = 0$, and we define

$$v_{\beta x} \equiv N_n(k_{\parallel}) - \Gamma_{nm}^{xx}(k_{\parallel}) = N_n(k_{\parallel}) + 1 - P_{nm}(k_{\parallel}), \quad (\text{A51})$$

$$v_{\beta y} \equiv N_n(k_{\parallel}) - \Gamma_{nm}^{yy}(\mathbf{k}_{\parallel}) = N_n(k_{\parallel}) + \frac{k_y^2}{k_{\parallel}^2} P_{nm}(k_{\parallel}), \quad (\text{A52})$$

with

$$\begin{aligned} P_{nm}(k_{\parallel}) &\equiv \frac{k_{\parallel}}{d} \int_0^d dx \int_0^d dx' \frac{e^{-k_{\parallel}|x-x'|}}{2} S_n(x) S_n(x') \\ &= \frac{\delta_{n0}}{2} + \left[\frac{k_{\parallel} d}{(k_{\parallel} d)^2 + (n\pi)^2} \right]^2 \\ &\quad \times \frac{[(k_{\parallel} d)^2 + (n\pi)^2 - 2k_{\parallel} d(1 - (-1)^n e^{-k_{\parallel} d})]}{1 + \delta_{n0}}. \end{aligned} \quad (\text{A53})$$

The dispersion relation of band n is thus compactly written as

$$\omega_{\beta} = \omega_n(\mathbf{k}_{\parallel}) = \omega_M \sqrt{v_{\beta x} v_{\beta y}}. \quad (\text{A54})$$

These frequencies correspond to the curves in Fig. 1(b).

Let us briefly explore the properties of the spin wave frequencies. First, we consider the insightful long- and short-wavelength limits $k_{\parallel} d \ll 1$ and $k_{\parallel} d \gg 1$, which correspond to $P_{nm} \approx 0$ and $P_{nm} \approx 1$, respectively. In the long wavelength limit, the dispersion relation in the case of negligible exchange (i.e., moderate n and $\alpha_x/d^2 \lesssim 1$) tends to the expression of the uniformly precessing mode in the absence of exchange [20],

$$\omega_n(\mathbf{k}_{\parallel}) \approx \sqrt{\omega_H(\omega_H + \omega_M)}. \quad (\text{A55})$$

On the other hand, if exchange is relevant (i.e., large n and $\alpha_x/d^2 \gtrsim 1$), then $N_n(k_{\parallel}) \gg 1$ and the long-wavelength limit becomes a quadratic function of the wave number [123] [see also Eq. (A24)]

$$\omega_n(\mathbf{k}_{\parallel}) \approx \omega_M \left[N_n(k_{\parallel}) + \frac{1}{2} \right]. \quad (\text{A56})$$

For short wavelength modes, the exchange interaction always dominates and one obtains, for $n \ll k_{\parallel} d/\pi$, the dispersion of exchange spin waves in a bulk material [59],

$$\omega_n(\mathbf{k}_{\parallel}) \approx (\omega_H + \omega_M \alpha_x k_{\parallel}^2) \sqrt{1 + \frac{\omega_M \sin^2 \phi_k}{\omega_H + \omega_M \alpha_x k_{\parallel}^2}}. \quad (\text{A57})$$

Second, note that, aside from the three dimensionless mode indices n , $k_{\parallel} d$, ϕ_k , the spin wave eigenfrequencies depend explicitly on H_0 and the film thickness d . As shown by Fig. 5, increasing H_0 leads to the bands shifting to higher frequencies [see Eq. (A55)], while decreasing d leads to the band becoming increasingly parabolic as exchange interaction becomes more relevant.

Let us now focus on the magnetization eigenmodes. Since for thin films the different bands are usually very spaced in energies [see e.g., Fig. 1(b)], the first-order corrections Eq. (A47), which are inversely proportional to $\omega_n(\mathbf{k}_{\parallel}) - \omega_n(\mathbf{k}'_{\parallel})$, are typically small and become only relevant at the band crossings where they result in a lifting of the degeneracy via mode splitting [57]. Here we will work far from these

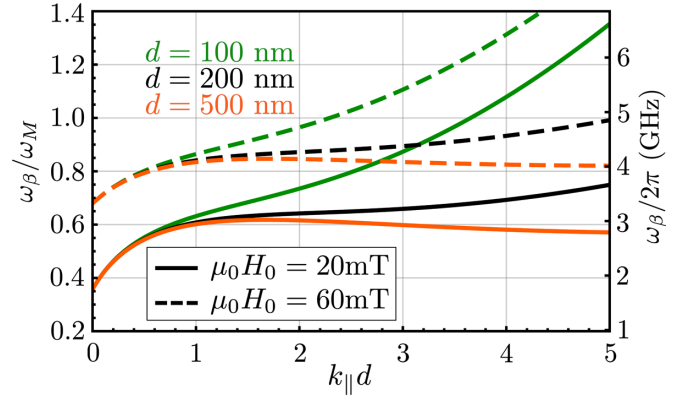


FIG. 5. $n = 0$ spin wave band of a YIG film for $\mu_0 H_0 = 20$ mT (solid lines) and $\mu_0 H_0 = 60$ mT (dashed lines), and for three values of the film thickness, namely, $d = 100$ (green), 200 (black), and 500 nm (orange).

particular points and thus describe the eigenmodes through their zeroth-order expression [25,123], given by the diagonal part of Eq. (A27)

$$\overline{\overline{D}}^{(nn)} \mathbf{m}_n = 0. \quad (\text{A58})$$

Combining the above equation with Eqs. (A50) and (A54) we obtain the following relation for the spin wave amplitudes,

$$\mathbf{m}_n \propto \begin{bmatrix} -i\sqrt{v_{\beta y}} \\ \sqrt{v_{\beta x}} \end{bmatrix}. \quad (\text{A59})$$

The magnetization mode function of an eigenmode is thus obtained directly from its definition Eq. (A14), together with Eqs. (A23) and (A26):

$$\mathbf{m}_{\beta}(\mathbf{r}) = \sqrt{\frac{2}{(1 + \delta_{n0})}} \cos\left(n\pi \frac{x}{d}\right) e^{i\mathbf{k}_{\parallel} \cdot \mathbf{r}_{\parallel}} \begin{bmatrix} \sqrt{v_{\beta y}} \\ i\sqrt{v_{\beta x}} \\ 0 \end{bmatrix} \quad (\text{A60})$$

in Cartesian coordinates, up to an arbitrary normalization constant. Finally, the magnetic field mode functions are obtained using the identities (A16)–(A18). Here we focus on the fields outside the film, and introduce an additional index $\eta \equiv \text{sign}[x]$ to differentiate between the field above and below the film [$\eta = +1$ and -1 , respectively, see Fig. 6(a)]. The mode functions outside the film can be written in a compact form as

$$\mathbf{h}_{\beta\eta}(\mathbf{r}) = \mathbf{h}_{n\eta}(\mathbf{k}_{\parallel}, \mathbf{r}) = h_{\beta\eta 0} e^{i\mathbf{k}_{\parallel} \cdot \mathbf{r}_{\parallel}} e^{-k_{\parallel} l} \begin{bmatrix} 1 \\ -i\eta k_y/k_{\parallel} \\ -i\eta k_z/k_{\parallel} \end{bmatrix} \quad (\text{A61})$$

where we have defined the absolute distance from the surface of the film,

$$l \equiv \begin{cases} x - d & \text{for } x > d \\ -x & \text{for } x < 0 \end{cases}. \quad (\text{A62})$$

The amplitudes in Eq. (A61) are given by

$$\begin{aligned} h_{\beta\eta 0} &= \sqrt{\frac{2}{(1 + \delta_{n0})}} \left(\sqrt{v_{\beta y}} + \eta \frac{k_y}{k_{\parallel}} \sqrt{v_{\beta x}} \right) \frac{\eta^n}{2} \\ &\quad \times \frac{(k_{\parallel} d)^2}{(k_{\parallel} d)^2 + (n\pi)^2} (-e^{-k_{\parallel} d} + (-1)^n). \end{aligned} \quad (\text{A63})$$

Note that $h_{\beta\eta 0}$ is real and fulfills the symmetry properties

$$h_{n+0}(k_y, k_z) = h_{n+0}(k_y, -k_z) \quad (\text{A64})$$

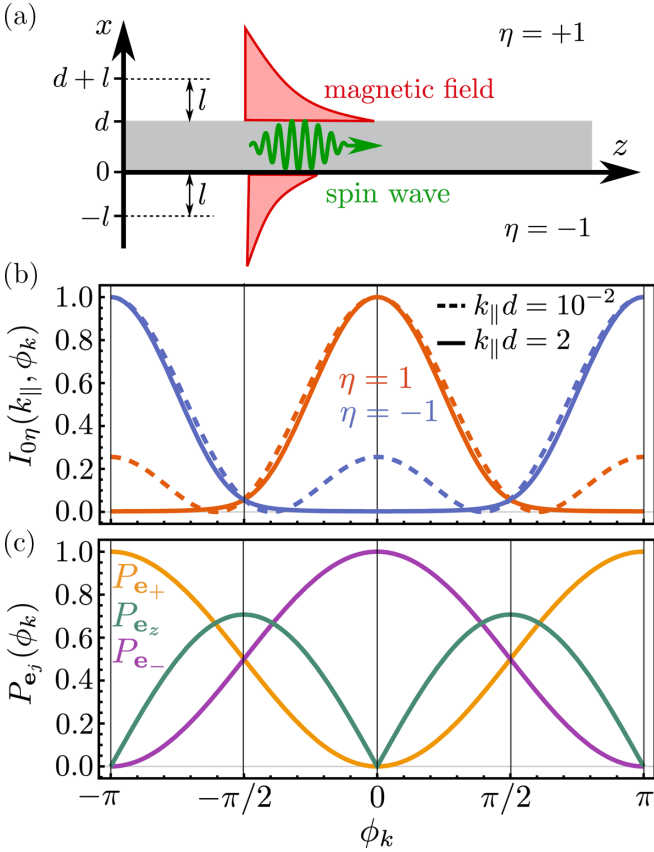


FIG. 6. (a) The magnetic field of a spin wave decays exponentially with the vertical distance from the film, l , and is different above ($\eta = +1$) and below ($\eta = -1$) the film. (b) Normalized field intensity (see text for details) of the spin wave above/below a YIG film (red/blue lines, respectively) as a function of propagation direction ϕ_k , for $n = 0$, $\mu_0 H_0 = 20$ mT, and $k_{\parallel} d = 2$ (solid lines) and 10^{-2} (dashed lines). (c) Degree of polarization of the spin wave field above the film along the cylindrical basis vectors Eq. (A66).

and

$$h_{n+0}(k_y, k_z) = (-1)^n h_{n-0}(-k_y, k_z), \quad (\text{A65})$$

which will be useful in the following sections.

It is insightful, especially regarding the coupling of spin waves to paramagnetic spins, to explore the properties of the magnetic field mode functions. According to Eq. (A61) the modal field has a plane-wave dependence on the y and z coordinates and decays exponentially with the distance to the film l [see Fig. 6(a) or Eq. (A62) in the main text]. Both its polarization and its amplitude depend on wave number k_{\parallel} , propagation direction ϕ_k , and film side η , giving rise to rich phenomenology [58,59]. To gain insight into it, we define two position-independent quantities describing the field intensity and direction. First, the normalized field intensity $I_{n\eta}(k_{\parallel}, \phi_k) \equiv |h_{\beta\eta 0}|^2 / \max_{k_{\parallel}, \phi_k} |h_{\beta\eta 0}|^2$, displayed in Fig. 6(b) for the fundamental band $n = 0$ (similar results are obtained for higher n). As shown by this figure, the field intensity is different on both sides of the film except in the parallel propagation case, $\phi_k = \pm\pi/2$. Additionally, as evidenced by the differences between solid and dashed lines, the ratio between the field intensities on each side of the film depends

on $k_{\parallel} d$. This so-called *modal-profile nonreciprocity* is well known in the literature [57,60] and, for spin waves fulfilling $\sqrt{v_{\beta y}} = -\eta \cos(\phi_k) \sqrt{v_{\beta x}}$, reaches its most pronounced manifestation as the field completely vanishes on one side of the film. In the relevant limits $k_{\parallel} d \gtrsim 1$ [solid lines in Fig. 6(b)] or $d^2/\alpha_x \lesssim k_{\parallel} d \lesssim 1$,⁹ this maximum asymmetry is reached for Damon-Eshbach propagation, $\phi_k = 0, \pi$ (see, e.g., Refs. [60,123]). To quantify the direction of the modal field, we define its degree of polarization along a unit vector \mathbf{e}_j above the film ($\eta = +1$) as $P_{\mathbf{e}_j}(\phi_k) \equiv |\mathbf{e}_j^* \cdot \mathbf{h}_{\beta+}(\mathbf{r})| / |\mathbf{h}_{\beta+}(\mathbf{r}) \cdot \mathbf{h}_{\beta+}(\mathbf{r})|^{1/2}$, which by definition depends exclusively on the angle ϕ_k . Note that the above quantity completely determines the polarization also below the film, since from Eq. (A61), we can deduce that the degree of polarization along \mathbf{e}_j below the film is given by $P_{\mathbf{e}_j}(-\phi_k)$. A further useful property derived from such equation is $\mathbf{h}_{\beta+}^*(\mathbf{r}) \cdot \mathbf{h}_{\beta-}(\mathbf{r}) = 0$, i.e., the field polarizations above and below the film are always orthogonal. In Fig. 6(c), we display the degree of polarization as a function of ϕ_k for the three cylindrical basis vectors

$$\{\mathbf{e}_+, \mathbf{e}_-, \mathbf{e}_z\} \equiv \left\{ \frac{\mathbf{e}_x + i\mathbf{e}_y}{\sqrt{2}}, \frac{\mathbf{e}_x - i\mathbf{e}_y}{\sqrt{2}}, \mathbf{e}_z \right\}. \quad (\text{A66})$$

Whereas for parallel propagation ($\phi_k = \pm\pi/2$) the modal field has components along all the basis vectors,¹⁰ in the Damon-Eshbach configuration the field is exactly polarized along one of the cylindrical vectors \mathbf{e}_{\pm} , with exactly the opposite helicity on the other side of the film. This polarization structure has a strong impact on the spin wave dynamics in the presence of spin qubits as we discuss in the main text.

5. Quantization, magnon dynamics, and magnon decay rates

We carry out the quantization of the spin waves following the procedure established by Mills for finite samples [61]. We do not show the details of this quantization as it has been discussed in detail in the literature [62]. For an infinitely extended film, we can extend this formalism following the quantization-in-a-box procedure common in quantum optics. First, we assume the film has an extension L along y and along z , and obeys periodic boundary conditions at the film edges $y = \pm L/2$ and $z = \pm L/2$. We then proceed with the quantization and take the continuum limit $L \rightarrow \infty$ when computing observables. In this limit, no observable will depend on the quantization length L . Following this procedure, we write the magnetization of the spin wave in the Schrödinger picture as

$$\hat{\mathbf{m}}(\mathbf{r}) = \sum_{\beta} \mathcal{M}_{0\beta} [\mathbf{m}_{\beta}(\mathbf{r}) \hat{s}_{\beta} + \text{H.c.}], \quad (\text{A67})$$

where the ladder operators, which describe the creation and annihilation of spin wave quanta (magnons), obey bosonic commutation relations,

$$[\hat{s}_{\beta}, \hat{s}_{\beta'}^{\dagger}] = \delta_{\beta\beta'}; \quad [\hat{s}_{\beta}, \hat{s}_{\beta'}] = 0, \quad (\text{A68})$$

⁹Note that the regime $d^2/\alpha_x \lesssim k_{\parallel} d \lesssim 1$ is not realizable with the parameters in Table I as $d^2/\alpha_x \approx 130$.

¹⁰As a matter of fact, for parallel propagation the spin wave is circularly polarized in the x - z plane, i.e., it has a longitudinal component of the same magnitude as its transverse component.

and the zero-point magnetization is given by

$$\mathcal{M}_{0\beta} \equiv \sqrt{\frac{\hbar|\gamma|M_S\omega_M}{2L^2d\omega_\beta}}. \quad (\text{A69})$$

The magnetic field operator has a similar expression, namely,

$$\hat{\mathbf{h}}(\mathbf{r}) = \sum_{\beta} \mathcal{M}_{0\beta} [\mathbf{h}_{\beta}(\mathbf{r})\hat{s}_{\beta} + \text{H.c.}]. \quad (\text{A70})$$

Finally, the Hamiltonian operator for the spin waves reads

$$\hat{H}_{\text{sw}} = \hbar \sum_{\beta} \omega_{\beta} \hat{s}_{\beta}^{\dagger} \hat{s}_{\beta}. \quad (\text{A71})$$

To properly account for the dynamics of spin waves, it is necessary to include their dissipation. In a quantum framework, losses are included after quantization of the lossless classical system. In particular, we add a dissipative term $\mathcal{D}[\hat{\rho}_{\text{sw}}]$ to the von Neumann equation for the spin wave density matrix, ρ_{sw} [68],

$$\frac{d}{dt} \hat{\rho}_{\text{sw}} = -\frac{i}{\hbar} [\hat{H}_{\text{sw}}, \hat{\rho}_{\text{sw}}] + \mathcal{D}_{\text{sw}}[\hat{\rho}_{\text{sw}}]. \quad (\text{A72})$$

We choose the most common form for the dissipator, namely,

$$\mathcal{D}_{\text{sw}}[\hat{\rho}] = \sum_{\beta} \gamma_{\beta} (\bar{n}_{\beta} \mathcal{L}_{\hat{s}_{\beta} \hat{s}_{\beta}^{\dagger}}[\hat{\rho}] + (1 + \bar{n}_{\beta}) \mathcal{L}_{\hat{s}_{\beta}^{\dagger} \hat{s}_{\beta}}[\hat{\rho}]), \quad (\text{A73})$$

which describes absorption and decay into a thermal bath at temperature T , in terms of Lindblad superoperators defined as

$$\mathcal{L}_{\hat{a}\hat{b}}[\hat{\rho}] \equiv \hat{a}\hat{\rho}\hat{b} - \frac{1}{2}\{\hat{b}\hat{a}, \hat{\rho}\}, \quad (\text{A74})$$

with γ_{β} the magnon decay rate and $\bar{n}_{\beta} = [\exp(\hbar\omega_{\beta}/k_B T) - 1]^{-1}$ the Bose-Einstein distribution at the magnon frequency. This dissipator can be rigorously derived by tracing out a reservoir coupled to spin waves via particle-conserving interactions, e.g., a phononic reservoir or a bath of two-level impurities [62,68,84].

All the spin wave phenomenology is captured by the Master equation (A73). First, it can be shown that the steady state of the spin waves is thermal, $\hat{\rho}_{\text{sw,ss}} \propto \exp(-\hat{H}_{\text{sw}}/k_B T)$. Second, regarding the spin wave dynamics, we can compute the equation of motion for the expected value of any magnon operator \hat{O} as

$$\frac{d}{dt} \langle \hat{O} \rangle(t) = \frac{d}{dt} \text{Tr}[\hat{O} \hat{\rho}_{\text{sw}}(t)]. \quad (\text{A75})$$

Furthermore, if the master equation is quadratic, as is the case for Eq. (A72), the above equations of motion form a closed system of differential equations and can thus be solved exactly [68,90]. Here we compute the equations of motion for single magnon operators and for two-operator products, which are given by

$$\frac{d}{dt} \langle \hat{s}_{\beta} \rangle(t) = \left(-i\omega_{\beta} - \frac{\gamma_{\beta}}{2} \right) \langle \hat{s}_{\beta} \rangle(t), \quad (\text{A76})$$

$$\frac{d}{dt} \langle \hat{s}_{\beta} \hat{s}_{\beta'} \rangle(t) = \left[-i(\omega_{\beta} + \omega_{\beta'}) - \frac{\gamma_{\beta} + \gamma_{\beta'}}{2} \right] \langle \hat{s}_{\beta} \hat{s}_{\beta'} \rangle(t), \quad (\text{A77})$$

$$\begin{aligned} \frac{d}{dt} \langle \hat{s}_{\beta}^{\dagger} \hat{s}_{\beta'} \rangle(t) &= \left[i(\omega_{\beta} - \omega_{\beta'}) - \frac{\gamma_{\beta} + \gamma_{\beta'}}{2} \right] \langle \hat{s}_{\beta}^{\dagger} \hat{s}_{\beta'} \rangle(t) \\ &+ \gamma_{\beta} \bar{n}_{\beta} \delta_{\beta\beta'}. \end{aligned} \quad (\text{A78})$$

Finally, we can use the above results, together with the quantum regression formula [90], to calculate the steady-state two-time correlators of the magnon operators, which determine the effective dynamics of NV centers as shown in Appendix E. Specifically, for a thermal state, correlators between two creation or two annihilation operators vanish, i.e.,

$$\langle \hat{s}_{\beta}(t) \hat{s}_{\beta'}(t-s) \rangle_{\text{ss}} = 0 \quad \forall s. \quad (\text{A79})$$

On the other hand, correlators between a creation and an annihilation operator are given, for $s \geq 0$, by

$$\langle \hat{s}_{\beta}^{\dagger}(t) \hat{s}_{\beta'}(t-s) \rangle_{\text{ss}} = \delta_{\beta\beta'} \bar{n}_{\beta} e^{i(\omega_{\beta} - \gamma_{\beta}/2)s}, \quad (\text{A80})$$

$$\langle \hat{s}_{\beta}(t) \hat{s}_{\beta'}^{\dagger}(t-s) \rangle_{\text{ss}} = \delta_{\beta\beta'} (1 + \bar{n}_{\beta}) e^{-i(\omega_{\beta} - \gamma_{\beta}/2)s}. \quad (\text{A81})$$

The corresponding correlators for negative s are obtained from the above expressions using the time-translational definitory property of the steady state, i.e.,

$$\langle \hat{O}_1(t) \hat{O}_2(t-s) \rangle_{\text{ss}} = \langle \hat{O}_1(t+s) \hat{O}_2(t) \rangle_{\text{ss}} \quad (\text{A82})$$

for any two operators \hat{O}_1 and \hat{O}_2 .

Once we have shown how to extract all the dynamical information of the spin waves from the master equation, the only step left is to relate the quantum decay rate, γ_{β} , to the measured spin wave lifetimes which are usually defined and measured in the classical limit. Classically, the losses of spin waves are modelled by adding the Gilbert damping term $(\alpha_G/M_S)\mathbf{M}(\mathbf{r}, t) \times (d/dt)\mathbf{M}(\mathbf{r}, t)$ to the right-hand side of the Landau Lifshitz equation Eq. (A1), with α_G the adimensional Gilbert damping parameter [19,20]. Together with the mode frequency ω_{β} , the damping α_G determines the lifetime of a given spin wave mode β [19,20,67]. Classically, the lifetime or relaxation time τ_{β} of a spin wave eigenmode β is defined as the time required for the amplitude of its magnetization to decay by a factor $1/e$ [20]. Here we use the expression provided by phenomenological loss theory [20,69,70],

$$\frac{1}{\tau_{\beta}} = \alpha_G \omega_{\beta} \frac{\partial \omega_{\beta}}{\partial \omega_H}, \quad (\text{A83})$$

which applies for small α_G (for YIG, $\alpha_G = 10^{-4}$ [69]) and is known to be a good description of propagation loss in thin films and stripes [69]. The relaxation time is usually inferred by coherently driving a selected spin wave mode through diverse methods and observing the decay of their amplitude [25,26,67,124–126]. We thus compute, using the equations of motion Eqs. (A76)–(A78), the expected value of the magnetization for a coherently populated single mode β_0 , i.e., for an initial magnon state fulfilling $\langle \hat{s}_{\beta}(t=0) \rangle = \alpha_0 \delta_{\beta\beta_0}$:

$$\langle \hat{\mathbf{m}}(\mathbf{r}, t) \rangle_{\text{coh}} \propto e^{-\gamma_{\beta_0} t/2} \text{Re}[\alpha_0 \mathbf{m}_{\beta_0}(\mathbf{r}) e^{-i\omega_{\beta_0} t}]. \quad (\text{A84})$$

Combining this equation, the definition of τ_{β} , and its expression Eq. (A83), we establish a correspondence between the

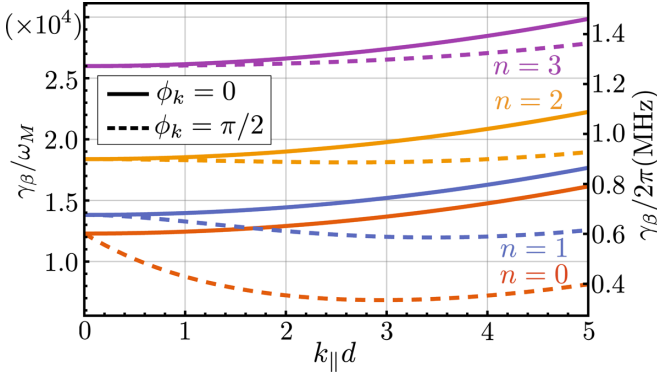


FIG. 7. Magnon decay rate Eq. (A86) for the first four bands of YIG and the parameters of Table I. Solid and dashed lines correspond to Damon-Eshbach and parallel propagation, respectively.

spin wave relaxation time τ_β and its decay rate through¹¹

$$\gamma_\beta = \frac{2}{\tau_\beta}. \quad (\text{A85})$$

The following explicit expression can be obtained from Eqs. (A83) and (A54),

$$\gamma_\beta = \alpha \omega_M (v_{\beta x} + v_{\beta y}). \quad (\text{A86})$$

This expression is displayed in Fig. 7 for the Damon-Eshbach ($\phi_k = 0$) and parallel ($\phi_k = \pi/2$) propagation modes. As evidenced by the figure, γ_β lies in the MHz range, correspond-

ing to a spin wave lifetime of around $\tau_\beta \sim 300$ ns, which agrees with experiments. Finally, note that γ_β displays the relevant symmetries $\gamma_n(k_y, k_z) = \gamma_n(-k_y, k_z) = \gamma_n(k_y, -k_z)$, which will be used in the next sections.

6. Magnon power spectral densities.

The potential of spin waves is conditioned to the degree of precision with which they can be measured. Usually, measurements are carried out on the spin wave magnetic field, and thus the figure of merit for sensing is the magnetic field power spectral density. We define the power spectral density of the magnetic field as¹²

$$S_{\mathbf{e}_j \mathbf{e}_k}(\mathbf{r}, \omega) \equiv \frac{1}{2\pi} \int_{-\infty}^{\infty} dse^{i\omega s} \times \langle (\mathbf{e}_j^\dagger \cdot \hat{\mathbf{h}}(\mathbf{r}, t)) (\hat{\mathbf{h}}(\mathbf{r}, t-s) \cdot \mathbf{e}_k) \rangle_{\text{ss}}, \quad (\text{A87})$$

i.e., as the Fourier transform of the steady-state two-time correlator of two arbitrary vector components of the spin wave magnetic field. Hereafter we will focus on the steady state of Eq. (A72), namely, a thermal state, but we remark that the power spectral density can be computed for arbitrary steady states such as e.g., a spin wave coherent state. Note that, as can be easily shown, the power spectral density of the total magnetic field $\hat{\mathbf{H}}(\mathbf{r}) \equiv \mathbf{H}_0 + \hat{\mathbf{h}}(\mathbf{r})$ is also given by Eq. (A87) for all $\omega \neq 0$, as the only effect of the homogeneous component \mathbf{H}_0 appears at $\omega = 0$.¹³

To compute the power spectral densities, we first calculate the two-time correlators of two arbitrary components of the spin wave magnetic field using Eqs. (A70), (A61), and (A63),

$$\langle (\mathbf{e}_j^\dagger \cdot \hat{\mathbf{h}}(\mathbf{r}, t)) (\hat{\mathbf{h}}(\mathbf{r}, t-s) \cdot \mathbf{e}_k) \rangle_{\text{ss}} = \sum_{\beta} \mathcal{M}_{0\beta}^2 h_{\beta\eta}^2 e^{-2k_{\parallel} l} [\bar{\Lambda}_{jk}(\eta, \mathbf{k}_{\parallel}) \langle \hat{s}_{\beta}^{\dagger}(t) \hat{s}_{\beta}^{\dagger}(t-s) \rangle_{\text{ss}} + \bar{\Lambda}_{jk}(-\eta, \mathbf{k}_{\parallel}) \langle \hat{s}_{\beta}^{\dagger}(t) \hat{s}_{\beta}(t-s) \rangle_{\text{ss}}]. \quad (\text{A88})$$

Here, we have defined the matrix elements $\bar{\Lambda}_{jk}(\eta, \mathbf{k}_{\parallel}) \equiv [\mathbf{e}_j^* \cdot \mathbf{v}_{\eta}(\mathbf{k}_{\parallel})][\mathbf{v}_{\eta}^*(\mathbf{k}_{\parallel}) \cdot \mathbf{e}_k]$, with $\mathbf{v}_{\eta}(\mathbf{k}_{\parallel}) \equiv [1, -i\eta k_y/k_{\parallel}, -i\eta k_z/k_{\parallel}]^T$. By explicitly introducing the magnon correlators Eqs. (A80) and (A81), integrating over the delay s , and using the symmetry $\bar{\Lambda}_{jk}(\eta, \mathbf{k}_{\parallel}) = \bar{\Lambda}_{kj}^*(\eta, \mathbf{k}_{\parallel})$, we compute the power spectral density as

$$S_{\mathbf{e}_j \mathbf{e}_k}(l, \omega) = \frac{1}{2\pi} \sum_{\beta} \mathcal{M}_{0\beta}^2 h_{\beta\eta}^2 e^{-2k_{\parallel} l} \gamma_{\beta} \left[\bar{\Lambda}_{jk}(\eta, \mathbf{k}_{\parallel}) \frac{\bar{n}_{\beta} + 1}{(\omega - \omega_{\beta})^2 + (\gamma_{\beta}/2)^2} + \bar{\Lambda}_{jk}(-\eta, \mathbf{k}_{\parallel}) \frac{\bar{n}_{\beta}}{(\omega + \omega_{\beta})^2 + (\gamma_{\beta}/2)^2} \right]. \quad (\text{A89})$$

The above expression is valid for any two vectors \mathbf{e}_j and \mathbf{e}_k . Here, we are interested on the (relatively simpler) power spectral density expressed in the cylindrical basis $\{\mathbf{e}_+, \mathbf{e}_-, \mathbf{e}_z\}$ defined by Eq. (A66). In this basis, the above matrix takes the form

$$\bar{\Lambda}(\eta, \mathbf{k}_{\parallel}) = \frac{1}{2k_{\parallel}^2} \begin{bmatrix} (k_{\parallel} - \eta k_y)^2 & k_z^2 & i\eta\sqrt{2}k_z(k_{\parallel} - \eta k_y) \\ k_z^2 & (k_{\parallel} + \eta k_y)^2 & i\eta\sqrt{2}k_z(k_{\parallel} + \eta k_y) \\ -i\eta\sqrt{2}k_z(k_{\parallel} - \eta k_y) & -i\eta\sqrt{2}k_z(k_{\parallel} + \eta k_y) & 2k_z^2 \end{bmatrix}. \quad (\text{A90})$$

¹¹The factor 2 in this definition stems from our use of the usual convention in open quantum systems, according to which the “natural” or most fundamental decay rate is the decay rate of the energy or, equivalently, of the occupation $\langle \hat{s}_{\beta}^{\dagger} \hat{s}_{\beta} \rangle \propto \exp(-\gamma_{\beta} t)$.

¹²Although for magnetic field sensing we are interested on the power spectral density of the magnetic field evaluated at same positions, one can also define the nonlocal power spectral densities $S_{\mathbf{e}_j \mathbf{e}_k}(\mathbf{r}_1, \mathbf{r}_2, \omega)$ and compute them in an analogous way.

¹³This can be easily proven for time-independent Liouvillians using the time-translational invariance of the steady state.

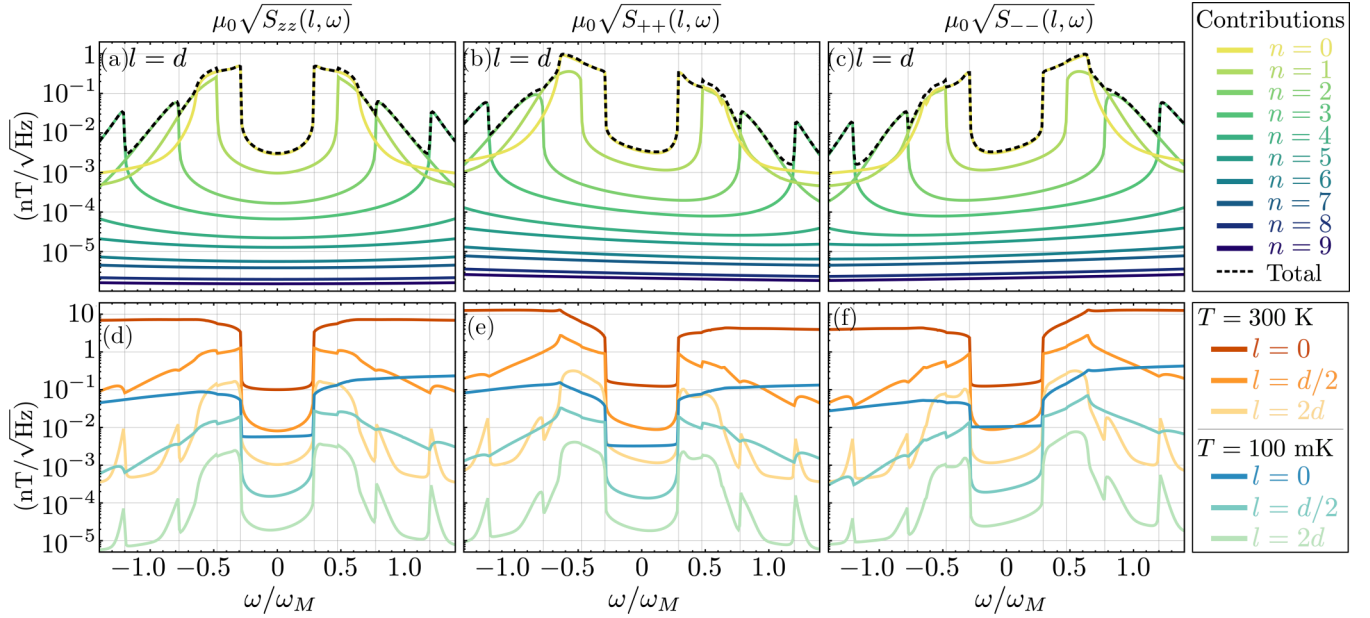


FIG. 8. [(a)–(c)] Power spectral densities of the spin wave magnetic field components along \mathbf{e}_z (a), \mathbf{e}_+ (b), and \mathbf{e}_- (c), at a distance $l = d = 200$ nm above the YIG film, $T = 300$ K and $\mu_0 H_0 = 20$ mT. The dashed line shows the total power spectral density, whereas the colored lines depict the contribution of each band n , i.e., the power spectral density computed using only the spin wave modes from a single band n . [(d)–(f)] Total power spectral densities at room ($T = 300$ K, warm-colored lines) and cryogenic temperatures ($T = 100$ mK, cool-colored lines), at three different distances l above the film.

Using this expression, and expressing the sum in mode indices β explicitly in integral form as

$$\sum_{\beta} \rightarrow \left(\frac{L}{2\pi}\right)^2 \sum_n \int d^2 \mathbf{k}_{\parallel}, \quad (\text{A91})$$

we can numerically compute the power spectral densities.

Due to the symmetries Eq. (A64) and (A65) and the invariance of γ_{β} and ω_{β} under change of sign of k_y or k_z , the following properties for the power spectral densities can be proven.

(1) The power spectral densities depend only on the vertical distance to the film, l (see Fig. 6), and are independent on the y and z coordinates.

(2) On each side of the film, the power spectral densities fulfill

$$S_{\mathbf{e}_{\pm}\mathbf{e}_z}(l, \omega) = S_{\mathbf{e}_z\mathbf{e}_{\pm}}(l, \omega) = 0, \quad (\text{A92})$$

$$S_{\mathbf{e}_+\mathbf{e}_-}(l, \omega) = S_{\mathbf{e}_-\mathbf{e}_+}(l, \omega) = \frac{1}{2} S_{\mathbf{e}_z\mathbf{e}_z}(l, \omega). \quad (\text{A93})$$

(3) In the high-temperature limit ($\bar{n}_{\beta} \gg 1$), the power spectral density along \mathbf{e}_z is an even function,

$$S_{\mathbf{e}_z\mathbf{e}_z}(l, \omega) = S_{\mathbf{e}_z\mathbf{e}_z}(l, -\omega) \quad \text{for } \bar{n}_{\beta} \gg 1. \quad (\text{A94})$$

Conversely, the functions $S_{\mathbf{e}_+\mathbf{e}_+}$ and $S_{\mathbf{e}_-\mathbf{e}_-}$ are not even due to the nonreciprocal modal properties discussed above. However, they are related through

$$S_{\mathbf{e}_+\mathbf{e}_+}(\mathbf{r}, -\omega) = S_{\mathbf{e}_-\mathbf{e}_-}(\mathbf{r}, \omega) \quad \text{for } \bar{n}_{\beta} \gg 1. \quad (\text{A95})$$

(4) The power spectral densities on different sides of the film are related through

$$\begin{bmatrix} S_{\mathbf{e}_+\mathbf{e}_+}(l, \omega) \\ S_{\mathbf{e}_-\mathbf{e}_-}(l, \omega) \\ S_{\mathbf{e}_z\mathbf{e}_z}(l, \omega) \end{bmatrix}_{\eta=-1} = \begin{bmatrix} S_{\mathbf{e}_-\mathbf{e}_-}(l, \omega) \\ S_{\mathbf{e}_+\mathbf{e}_+}(l, \omega) \\ S_{\mathbf{e}_z\mathbf{e}_z}(l, \omega) \end{bmatrix}_{\eta=1}. \quad (\text{A96})$$

Because of the above relations, we can focus on the three independent power spectral densities $S_{\mathbf{e}_+\mathbf{e}_+}(\mathbf{r}, \omega)$, $S_{\mathbf{e}_-\mathbf{e}_-}(\mathbf{r}, \omega)$, and $S_{\mathbf{e}_z\mathbf{e}_z}(\mathbf{r}, \omega)$ above the film ($\eta = 1$). In Figs. 8(a)–8(c), we display the square root of these three quantities at room temperature ($T = 300$ K), for $\mu_0 H_0 = 20$ mT and $l = d = 200$ nm. The involved form of the total power spectral densities (dashed lines) is a consequence of adding the contributions from each spin wave band n , displayed by the different colored lines. At frequencies below the cutoffs of each spin wave band, the power spectral densities are suppressed due to the absence of resonant eigenmodes. At the cutoff frequency of each band, indicated by the vertical grid lines in the figure, the power spectral density shows a sharp jump due to the sudden increase in the density of states $\propto (d\omega_{\beta}/dk_{\parallel})^{-1}$, followed by a smooth decrease as such density of states is reduced. Finally, note that as discussed above the power spectral density $S_{zz}(l, \omega)$ is an even function of frequency, whereas the functions $S_{\pm\pm}(l, \omega)$ are strongly asymmetric and, above cutoff, their values at positive and negative frequencies differ by roughly an order of magnitude. This asymmetry stems directly from the nonreciprocal spin wave mode properties. The above basic features of the power spectral densities remain unchanged at low temperature or at different positions l above the film, as evidenced by Figs. 8(d)–8(f). As shown by this figure, the power spectral densities decrease both at lower temperature and at larger distances from the

film l , following the reduction of the thermal amplitude of the spin wave magnetic field. As a final remark, note that the power spectral densities shown in Fig. 8 are experimentally measurable as they lie well above the sensitivity limit ($\sim 10^{-4}$ – 10^{-6} nT/ $\sqrt{\text{Hz}}$) of ultra-sensitive room-temperature magnetometry techniques based, e.g., on ensembles of NV centers [127,128] or on atomic vapor cells [128–130].

7. Second-order correction to the spin wave fields

In order to evaluate the spin wave induced dephasing of the NV centers in the following sections, the expressions of the spin wave magnetization and magnetic fields have to be computed to second order in magnon operators. This is equivalent to considering the lowest-order nonlinear terms in the spin wave approximation (A5). We proceed in the standard way [4,62] by writing the total magnetization as

$$\mathbf{M}(\mathbf{r}, t) = m_x(\mathbf{r}, t)\mathbf{e}_x + m_y(\mathbf{r}, t)\mathbf{e}_y + \sqrt{M_S^2 - m_x^2(\mathbf{r}, t) - m_y^2(\mathbf{r}, t)}\mathbf{e}_z, \quad (\text{A97})$$

and expanding to second order in the spin wave amplitudes m_x and m_y ,

$$\mathbf{M}(\mathbf{r}, t) = M_S\mathbf{e}_z + \mathbf{m}(\mathbf{r}, t) - \frac{\mathbf{m}(\mathbf{r}, t) \cdot \mathbf{m}(\mathbf{r}, t)}{2M_S}\mathbf{e}_z + \mathcal{O}(\mathbf{m}^3). \quad (\text{A98})$$

Here, $\mathbf{m}(\mathbf{r}, t) = m_x(\mathbf{r}, t)\mathbf{e}_x + m_y(\mathbf{r}, t)\mathbf{e}_y$ is the first-order spin wave amplitude, i.e., the solution of the linearized Landau-Lifshitz equation (A6). By substituting it by the corresponding quantum operator $\hat{\mathbf{m}}(\mathbf{r})$, Eq. (4), we obtain the expression for the total magnetization operator,

$$\hat{\mathbf{M}}(\mathbf{r}) = M_S\mathbf{e}_z + \hat{\mathbf{m}}^{(2)}(\mathbf{r}) + \mathcal{O}(\hat{\mathbf{m}}^3), \quad (\text{A99})$$

where $\hat{\mathbf{m}}^{(2)}(\mathbf{r})$ is the spin wave magnetization up to second order in magnon operators, namely

$$\hat{\mathbf{m}}^{(2)}(\mathbf{r}) = \hat{\mathbf{m}}(\mathbf{r}) + \delta\hat{\mathbf{m}}(\mathbf{r}), \quad (\text{A100})$$

with a second-order correction given by

$$\delta\hat{\mathbf{m}}(\mathbf{r}) = -\mathbf{e}_z \sum_{\beta\beta'} \frac{\mathcal{M}_{0\beta}\mathcal{M}_{0\beta'}}{2M_S} [\mathbf{m}_\beta(\mathbf{r}) \cdot \mathbf{m}_{\beta'}(\mathbf{r})\hat{s}_\beta\hat{s}_{\beta'} + \mathbf{m}_\beta(\mathbf{r}) \cdot \mathbf{m}_{\beta'}^*(\mathbf{r})\hat{s}_\beta\hat{s}_{\beta'}^\dagger + \text{H.c.}], \quad (\text{A101})$$

From Eq. (A100), we can compute the corresponding spin wave magnetic field as, within the magnetostatic approximation, it is always related to the magnetization through the Green's tensor by Eq. (A7). Thus, to second order in magnon operators, the spin wave field operator reads

$$\hat{\mathbf{h}}^{(2)}(\mathbf{r}) = \hat{\mathbf{h}}(\mathbf{r}) + \delta\hat{\mathbf{h}}(\mathbf{r}), \quad (\text{A102})$$

with $\hat{\mathbf{h}}(\mathbf{r})$ being the first-order magnetic field given by Eq. (A70), and a second-order correction given by

$$\delta\hat{\mathbf{h}}(\mathbf{r}) = \sum_{\beta\beta'} [\mathbf{X}_{\beta\beta'}^+(\mathbf{r})\hat{s}_\beta\hat{s}_{\beta'} + \mathbf{X}_{\beta\beta'}^-(\mathbf{r})\hat{s}_\beta\hat{s}_{\beta'}^\dagger + \text{H.c.}], \quad (\text{A103})$$

where we define the vectors

$$\begin{aligned} \begin{bmatrix} \mathbf{X}_{\beta\beta'}^+(\mathbf{r}) \\ \mathbf{X}_{\beta\beta'}^-(\mathbf{r}) \end{bmatrix} &\equiv -\frac{\mathcal{M}_{0\beta}\mathcal{M}_{0\beta'}}{2M_S} \int d^3\mathbf{r}' \bar{\mathcal{G}}(\mathbf{r} - \mathbf{r}') \\ &\times \mathbf{e}_z \begin{bmatrix} \mathbf{m}_\beta(\mathbf{r}') \cdot \mathbf{m}_{\beta'}(\mathbf{r}') \\ \mathbf{m}_\beta(\mathbf{r}') \cdot \mathbf{m}_{\beta'}^*(\mathbf{r}') \end{bmatrix}. \end{aligned} \quad (\text{A104})$$

In order to compute the coefficients $\mathbf{X}_{\beta\beta'}^\pm(\mathbf{r})$, we introduce the expression of the magnetization mode functions, Eq. (A60), into Eq. (A104) and rearrange the terms to write in a compact form

$$\mathbf{X}_{\beta\beta'}^\pm = \frac{\mathcal{M}_{0\beta}\mathcal{M}_{0\beta'}}{M_S} X_{0\beta\beta'}^\pm \mathbf{x}_{nm'}(\mathbf{r}, \mathbf{k}_\parallel \pm \mathbf{k}'_\parallel), \quad (\text{A105})$$

where

$$X_{0\beta\beta'}^\pm = \frac{-1}{\sqrt{(1 + \delta_{n0})(1 + \delta_{n'0})}} (\sqrt{\nu_{\beta y}\nu_{\beta' y}} \mp \sqrt{\nu_{\beta x}\nu_{\beta' x}}) \quad (\text{A106})$$

with $\nu_{\beta x}$ and $\nu_{\beta y}$ given by Eqs. (A51) and (A52), and

$$\begin{aligned} \mathbf{x}_{nm'}(\mathbf{r}, \mathbf{q}) &\equiv \int_{\text{slab}} d^3\mathbf{r}' \bar{\mathcal{G}}(\mathbf{r} - \mathbf{r}') \mathbf{e}_z \cos \left[n\pi \frac{x'}{d} \right] \\ &\times \cos \left[n'\pi \frac{x'}{d} \right] e^{i\mathbf{q}\mathbf{r}'_\parallel}. \end{aligned} \quad (\text{A107})$$

We now focus on a position \mathbf{r} outside the slab, and introduce the Green's tensor Eq. (A11) to find the following expression for the above integral:

$$\begin{aligned} \mathbf{x}_{nm'}(\mathbf{r}, \mathbf{q}) &= e^{i\mathbf{q}_\parallel \mathbf{r}_\parallel} e^{-q_\parallel l} (-1)^{n+n'} \frac{q_z d}{4} \begin{bmatrix} i\eta q_\parallel d \\ -q_y d \\ -q_z d \end{bmatrix} (1 - e^{-q_\parallel d}) \\ &\times \sum_{\lambda=\pm} \frac{1}{\pi^2 (n' + \lambda n)^2 + (q_\parallel d)^2}, \end{aligned} \quad (\text{A108})$$

where we have introduced the absolute distance to the slab, l , as in Eq. (A62), and the variable η to differentiate between positions \mathbf{r} above and below the slab. Note that, importantly, the above function decays exponentially with the modulus of \mathbf{q}_\parallel , and

$$\mathbf{x}_{nm'}(\mathbf{r}, 0) \rightarrow 0. \quad (\text{A109})$$

This, combined with Eqs. (A105) and (A106), leads to the result

$$\mathbf{X}_{\beta\beta'}^- = 0, \quad (\text{A110})$$

which will be important in the following sections.

APPENDIX B: NITROGEN-VACANCY CENTERS

This Appendix is devoted to the analysis of the NV centers and their dynamics. First, in Appendix B 1, we theoretically describe the Hamiltonian and dissipative mechanisms governing the dynamics of a single NV center in thermal equilibrium. We derive the equations of motion for all the observables and rigorously define the dissipation rates in terms of the lifetimes T_1 and T_2^* , and we compute the two-time correlators for NV center observables. Then, in Appendix B 2, we extend our analysis to optically pumped NV centers. We compute the

dynamics of the NV observables and determine the optimal pumping rate. Finally, we compute both the two-time correlators and the NV correlation time in the presence of optical pumping.

1. Dynamics of a single isolated NV center in thermal equilibrium

In this section, we study the dynamics of a single NV center in thermal equilibrium. As in the main text, we assume the symmetry axis of the NV center is oriented parallel to the z axis, and a static magnetic field $\mathbf{H}_0 = H_0 \mathbf{e}_z$ is applied along this axis. The ground state manifold is a spin triplet with total spin $S = 1$, thus containing three states $|0\rangle$, $|+\rangle$, and $|-\rangle$ corresponding to the eigenstates of the spin operator \hat{S}_z with eigenvalue $m_S = 0, +\hbar$, and $-\hbar$, respectively. In the absence of optical pumping, excited states are uncoupled and we can describe the NV center through the Hamiltonian of the ground state manifold [10,11,63–65]:

$$\hat{H}_{\text{ps}} = \hbar^{-1} D_0 \hat{S}_z^2 + \omega_H \hat{S}_z = \hbar \sum_{\alpha=\pm} \omega_\alpha \hat{\sigma}_{\alpha\alpha}, \quad (\text{B1})$$

where we define the transition matrices $\hat{\sigma}_{\alpha\alpha'} \equiv |\alpha\rangle\langle\alpha'|$ and the frequencies $\omega_\pm \equiv D_0 \pm \omega_H$ and $\omega_H \equiv |\gamma_s| \mu_0 H_0$, and the z component of the spin operator is given by $\hat{S}_z/\hbar = \hat{\sigma}_{++} - \hat{\sigma}_{--}$. For an NV center the gyromagnetic factor is $\gamma_s = \gamma$ (see Table I). The density matrix of the NV center obeys the von Neumann equation

$$\frac{d}{dt} \hat{\rho}_{\text{ps}} = -\frac{i}{\hbar} [\hat{H}_{\text{ps}}, \hat{\rho}_{\text{ps}}] + \mathcal{D}_{\text{ps}}[\hat{\rho}_{\text{ps}}], \quad (\text{B2})$$

where the second term accounts for dissipation, namely, decay and dephasing. In principle, there are different approaches to describe these processes [63–65,71]. Here we choose the description given by the dissipator

$$\mathcal{D}_{\text{ps}}[\hat{\rho}] = \frac{\kappa_2}{\hbar^2} \mathcal{L}_{\hat{S}_z \hat{S}_z}[\hat{\rho}] + \kappa_1 \sum_{\alpha=\pm} (\bar{n}_\alpha \mathcal{L}_{\hat{\sigma}_{\alpha 0} \hat{\sigma}_{0\alpha}}[\hat{\rho}] + (\bar{n}_\alpha + 1) \mathcal{L}_{\hat{\sigma}_{0\alpha} \hat{\sigma}_{\alpha 0}}[\hat{\rho}]). \quad (\text{B3})$$

The first term above describes dephasing at a rate κ_2 , whereas the second line describes decay and absorption at a rate κ_1 along the two NV transitions, namely, $|0\rangle \leftrightarrow |\pm\rangle$, induced by a bosonic thermal reservoir at temperature T , with $\bar{n}_\alpha = [\exp(\hbar\omega_\alpha/k_B T) - 1]^{-1}$.

The equations of motion for the spin observables can be obtained from the above equation. On the one hand, the two independent quantities describing the level occupations $\langle \hat{\sigma}_{\alpha\alpha} \rangle$ obey the coupled system of equations [64,71,72]

$$\frac{d}{dt} \begin{bmatrix} \langle \hat{\sigma}_{00} \rangle \\ \langle \hat{S}_z/\hbar \rangle \end{bmatrix} = \begin{bmatrix} \kappa_1 + \gamma_+ \\ \gamma_- \end{bmatrix} - \bar{M}_0 \begin{bmatrix} \langle \hat{\sigma}_{00} \rangle \\ \langle \hat{S}_z/\hbar \rangle \end{bmatrix}, \quad (\text{B4})$$

with

$$\bar{M}_0 = \begin{bmatrix} \kappa_1 + 3\gamma_+ & \gamma_- \\ 3\gamma_- & \kappa_1 + \gamma_+ \end{bmatrix} \quad (\text{B5})$$

and

$$\gamma_\pm \equiv \frac{\kappa_1}{2} (\bar{n}_- \pm \bar{n}_+). \quad (\text{B6})$$

The general solution of the above equation is given by

$$\begin{bmatrix} \langle \hat{\sigma}_{00}(t) \rangle \\ \langle \hat{S}_z(t)/\hbar \rangle \end{bmatrix} = \begin{bmatrix} \langle \hat{\sigma}_{00} \rangle_{\text{ss}} \\ \langle \hat{S}_z/\hbar \rangle_{\text{ss}} \end{bmatrix} + \frac{e^{-(\kappa_1 + 2\gamma_+)t}}{3\gamma_-} \bar{M}(t) \times \begin{bmatrix} \langle \hat{\sigma}_{00} \rangle(0) - \langle \hat{\sigma}_{00} \rangle_{\text{ss}} \\ \langle \hat{S}_z/\hbar \rangle(0) - \langle \hat{S}_z/\hbar \rangle_{\text{ss}} \end{bmatrix}, \quad (\text{B7})$$

with

$$\bar{M}(t) \equiv \begin{bmatrix} (\gamma_+ - s_d) e^{s_d t} & (\gamma_+ + s_d) e^{-s_d t} \\ 3\gamma_- e^{s_d t} & 3\gamma_- e^{-s_d t} \end{bmatrix} \quad (\text{B8})$$

and $s_d \equiv \sqrt{\gamma_+^2 + 3\gamma_-^2}$. The steady-state solution reads

$$\begin{bmatrix} \langle \hat{\sigma}_{00} \rangle_{\text{ss}} \\ \langle \hat{S}_z/\hbar \rangle_{\text{ss}} \end{bmatrix} = \frac{1}{(\kappa_1 + \gamma_+)(\kappa_1 + 3\gamma_+) - 3\gamma_-^2} \times \begin{bmatrix} (\kappa_1 + \gamma_+)^2 - \gamma_-^2 \\ -2\gamma_- \kappa_1 \end{bmatrix}. \quad (\text{B9})$$

On the other hand, the system coherences remain uncoupled and obey the equations

$$\frac{d\langle \hat{\sigma}_{0\pm} \rangle}{dt} = \left[-i\omega_\pm - \frac{\kappa_1 + 3\gamma_+ \mp \gamma_-}{2} - \frac{\kappa_2}{2} \right] \langle \hat{\sigma}_{0\pm} \rangle, \quad (\text{B10})$$

$$\frac{d\langle \hat{\sigma}_{+-} \rangle}{dt} = [i(\omega_+ - \omega_-) - (\gamma_+ + \kappa_1) - 2\kappa_2] \langle \hat{\sigma}_{+-} \rangle. \quad (\text{B11})$$

From the above equations it is evident that all coherences are zero in the steady state and that they decay and dephase at different rates.

a. Definition of T_1 and T_2^*

Since the rates γ_\pm depend on the externally applied field through the frequencies ω_\pm , the decay time of the expected values $\langle \hat{\sigma}_{\alpha\alpha} \rangle$ also does. For this reason, the intrinsic T_1 and T_2^* are defined in the zero-field limit $H_0 \rightarrow 0$ [71,72]. In this limit, $\gamma_- \rightarrow 0$ and

$$\gamma_+ \rightarrow \kappa_1 \bar{n}_0 \quad (\text{B12})$$

with $\bar{n}_0 = [\exp(\hbar D_0/k_B T) - 1]^{-1}$ the Bose-Einstein distribution evaluated at the zero-field splitting frequency D_0 . The decay time T_1 is defined as the inverse of the equilibration rate of the NV occupations after initialization in the ground state $|0\rangle$ [71,72]. For such an initial state $\langle \hat{S}_z/\hbar \rangle(t) = 0$ and the occupations of all levels obey a single exponential behavior,

$$\langle \hat{\sigma}_{00}(t) \rangle = [1 - \langle \hat{\sigma}_{00} \rangle_{\text{ss}}] e^{-(\kappa_1 + 3\gamma_+)t} + \langle \hat{\sigma}_{00} \rangle_{\text{ss}}, \quad (\text{B13})$$

$$\langle \hat{\sigma}_{++}(t) \rangle = \langle \hat{\sigma}_{--}(t) \rangle = \frac{1 - \langle \hat{\sigma}_{00}(t) \rangle}{2}. \quad (\text{B14})$$

From the above expressions the relaxation time T_1 is defined as

$$T_1^{-1} \equiv \kappa_1 + 3\gamma_+ = \kappa_1(1 + 3\bar{n}_0). \quad (\text{B15})$$

The above definition allows to fix a value for κ_1 from experimentally measured values of T_1 .

The second relevant timescale, namely, the decoherence time T_2^* , is defined through the decay of the coherences $\langle \hat{\sigma}_{0,\pm} \rangle$, which in the zero-field limit obey the same exponential decay,

$$\langle \hat{\sigma}_{0,\pm}(t) \rangle = \langle \hat{\sigma}_{0,\pm}(0) \rangle e^{[-i\omega_\pm - (\kappa_2 + \kappa_1 + 3\gamma_+)/2]t}. \quad (\text{B16})$$

From the above expression, we define

$$[T_2^*]^{-1} = \frac{\kappa_2}{2} + \frac{\kappa_1 + 3\gamma_+}{2} = \frac{T_1^{-1}}{2} + \frac{\kappa_2}{2}. \quad (\text{B17})$$

Note that T_2^* has contributions from decay and dephasing rates κ_1 and κ_2 , which gives rise to the fundamental limit $T_2^* \leq 2T_1$ [63,72,73].

b. Two-time correlators of NV operators

In a similar fashion as for the magnon operators, we can compute the two-time correlators of products of NV operators, which will determine the effective spin wave dynamics as we will see below. We compute such correlators from the equations of motion Eqs. (B4), (B10), and (B11) and the quantum regression theorem [90]. The simplest correlators are those involving the coherences, which for a general operator \hat{O} and for $s \geq 0$ read

$$\langle \hat{\sigma}_{0\pm}(t)\hat{O}(t-s) \rangle_{\text{ss}} = e^{-s[i\omega_{\pm} + (\kappa_1 + 3\gamma_+ \mp \gamma_- + \kappa_2)/2]} \langle \hat{\sigma}_{0\pm}\hat{O} \rangle_{\text{ss}}, \quad (\text{B18})$$

$$\langle \hat{\sigma}_{\pm 0}(t)\hat{O}(t-s) \rangle_{\text{ss}} = e^{-s[-i\omega_{\pm} + (\kappa_1 + 3\gamma_+ \mp \gamma_- + \kappa_2)/2]} \langle \hat{\sigma}_{\pm 0}\hat{O} \rangle_{\text{ss}}. \quad (\text{B19})$$

$$\langle \hat{\sigma}_{+-}(t)\hat{O}(t-s) \rangle_{\text{ss}} = e^{s[i(\omega_+ - \omega_-) - \kappa_1 - \gamma_+ - 2\kappa_2]} \langle \hat{\sigma}_{+-}\hat{O} \rangle_{\text{ss}}, \quad (\text{B20})$$

$$\langle \hat{\sigma}_{-+}(t)\hat{O}(t-s) \rangle_{\text{ss}} = e^{s[-i(\omega_+ - \omega_-) - \kappa_1 - \gamma_+ - 2\kappa_2]} \langle \hat{\sigma}_{-+}\hat{O} \rangle_{\text{ss}}. \quad (\text{B21})$$

Regarding the occupations, the quantities of interest are usually not the operators $\langle \hat{\sigma}_{00} \rangle$ or $\langle \hat{S}_z \rangle$ themselves, but the fluctuations over their expected value, defined as

$$\begin{bmatrix} \langle \tilde{\sigma}_{00} \rangle \\ \langle \tilde{S}_z/\hbar \rangle \end{bmatrix} \equiv \begin{bmatrix} \langle \hat{\sigma}_{00} \rangle \\ \langle \hat{S}_z/\hbar \rangle \end{bmatrix} - \begin{bmatrix} \langle \hat{\sigma}_{00} \rangle_{\text{ss}} \\ \langle \hat{S}_z/\hbar \rangle_{\text{ss}} \end{bmatrix}. \quad (\text{B22})$$

For any operator \hat{O} and any $s \geq 0$, the correlators involving these operators are coupled,

$$\begin{bmatrix} \langle \tilde{\sigma}_{00}(t)\hat{O}(t-s) \rangle \\ \langle (\tilde{S}_z/\hbar)(t)\hat{O}(t-s) \rangle \end{bmatrix} = \frac{e^{-(\kappa_1 + 2\gamma_+)s}}{3\gamma_-} \overline{\overline{M}}(s) \begin{bmatrix} \langle \tilde{\sigma}_{00}\hat{O} \rangle_{\text{ss}} \\ \langle (\tilde{S}_z/\hbar)\hat{O} \rangle_{\text{ss}} \end{bmatrix}, \quad (\text{B23})$$

where the matrix $\overline{\overline{M}}(s)$ is defined in Eq. (B8).

2. Dynamics of a single optically pumped NV centre

One of the multiple advantages of NV centers is the possibility to optically initialize them at room temperature, by a procedure known as optical pumping [44,78–83]. In order to describe and understand this procedure one must consider the extended energy level structure of NV centers depicted in Fig. 9(a). The states $|0\rangle$ and $|\pm\rangle$ introduced in the previous sections correspond to the ground-state manifold 3A . The excited state manifold 3E is also a spin triplet with zero-field splitting $D_1 \neq D_0$ (see Table II), here described as two states $|3\rangle$ and $|4\rangle$ for the sake of simplicity [78,80,82]. These two states spontaneously decay into the ground-state manifold, with decay rates γ_c and $\gamma_{nc} \ll \gamma_c$ for spin-conserving

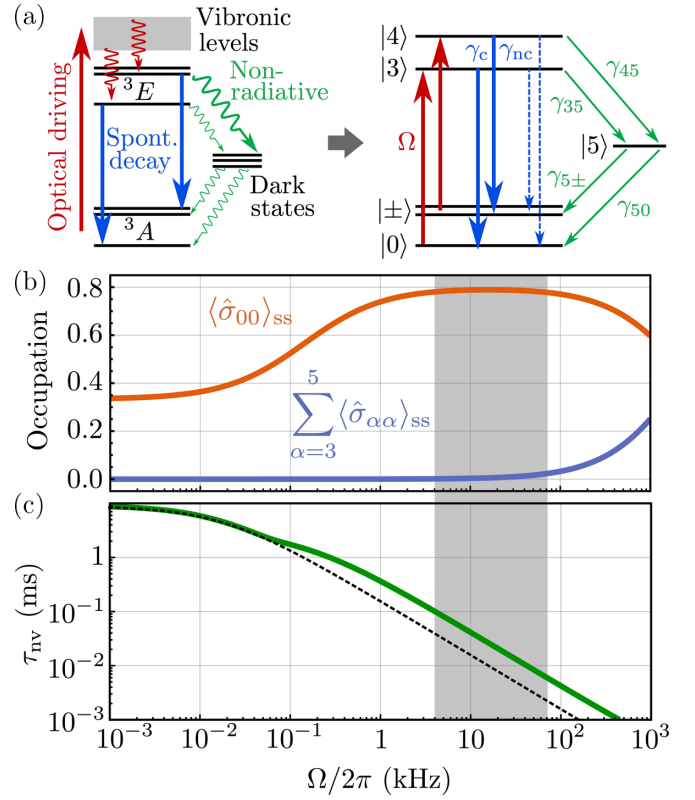


FIG. 9. (a) Left: illustration of the main processes involved in optical pumping. Straight and wiggly lines indicate radiative and nonradiative processes respectively. Right: modeling of the optical pumping and the relevant states. (b) Ground-state occupation (red) and total occupation outside the ground-state manifold (blue) as a function of pumping rate. (c) Correlation time of the NV center occupations, Eq. (B43) as a function of pumping rate. The dashed curve displays the timescale $(\kappa_1 + \gamma_+ + \Omega)^{-1}$. The gray area indicates the optimal region for optical pumping. For (b) and (c), we take $\mu_0 H_0 = 20$ mT, and the results do not change appreciably within the range $0 \leq \mu_0 H_0 \leq 100$ mT.

and spin nonconserving transitions, respectively. For optical pumping a coherent, linearly polarized (i.e., m_S -conserving) driving is applied to the transition ${}^3A \rightarrow {}^3E$. Since this driving mostly excites vibronic transitions which rapidly and stochastically decay to the zero-phonon line, the effective pumping of

TABLE II. Room temperature values for the rates involved in the optical pumping cycle of an NV center [78–80,82].

Rate	Value
D_1	$2\pi \times 1.423$ GHz
γ_c	$2\pi \times 9.7$ MHz
γ_{nc}	$\approx 10^{-2}\gamma_c$
γ_{45}	$2\pi \times 12$ MHz
γ_{35}	$2\pi \times 1.74$ MHz
$\gamma_{5\pm}$	$2\pi \times 0.21$ MHz
γ_{50}	$2\pi \times 0.49$ MHz
κ_ϕ	$2\pi \times 10^6$ MHz
α_d	0.45 mHz W ⁻¹ m ²

occupation into the excited-state manifold is incoherent [80,82]. Finally, in addition to their spontaneous decay, the states |3) and |4) can decay nonradiatively (incoherently) into a manifold of intermediate “dark” states, here modelled as a single state |5) [80,82,83], which in turn decay nonradiatively to the ground state manifold. This decay is largely imbalanced: specifically, the decay rate from state |4) into state |5) is much faster than any other decay rates into or out of the dark state |5), i.e., $\gamma_{45} \gg \gamma_{35}, \gamma_{5\pm}, \gamma_{50}$ (see Table II). As a result of this imbalance, part of the initial occupation of states with nonzero spin, $|\pm\rangle$, is *pumped* into the zero-spin state |0), thus driving the NV center toward its ground state.

We describe optical pumping of NV centers through the following master equation for the six-level system illustrated in Fig. 9(a):

$$\frac{d\hat{\rho}}{dt} = -i[\hat{H}_{\text{ps}} + \hat{H}_{\text{ps}}^{(2)}, \hat{\rho}] + \mathcal{D}_{\text{ps}}[\hat{\rho}] + \mathcal{D}_{\text{op}}[\hat{\rho}]. \quad (\text{B24})$$

Here, \hat{H}_{ps} and \mathcal{D}_{ps} represent the Hamiltonian and the dissipator of the ground-state manifold, and are given by Eqs. (B1) and (B3). The second coherent contribution corresponds to the Hamiltonian of the additional levels, i.e.,

$$\hat{H}_{\text{ps}}^{(2)} = \hbar \sum_{\alpha=3}^5 \omega_{\alpha} \hat{\sigma}_{\alpha\alpha}. \quad (\text{B25})$$

The values of the frequencies $\omega_{3,4,5}$ are irrelevant for the dynamics of the ground state manifold as we will see below. Regarding the additional dissipator, it can be split into three contributions,

$$\mathcal{D}_{\text{op}}[\hat{\rho}] = \mathcal{D}_{\text{p}}[\hat{\rho}] + \mathcal{D}_{\text{s}}[\hat{\rho}] + \mathcal{D}_{\phi}[\hat{\rho}]. \quad (\text{B26})$$

The first term above represents the spin-conserving incoherent pumping from all the states in the ground state manifold into all states in the excited state manifold,

$$\mathcal{D}_{\text{p}}[\hat{\rho}] = \hbar\Omega \left(\mathcal{L}_{\hat{\sigma}_{30}\hat{\sigma}_{03}}[\hat{\rho}] + \sum_{\alpha=\pm} \mathcal{L}_{\hat{\sigma}_{4\alpha}\hat{\sigma}_{\alpha 4}}[\hat{\rho}] \right). \quad (\text{B27})$$

The incoherent driving rate Ω is related to the applied optical intensity I_d through $\Omega = \alpha_d I_d$, where $\alpha_d = 0.2 - 0.7 \text{mHz W}^{-1} \text{m}^2$ is the optical pumping parameter (see

Table II). The second contribution in the dissipator Eq. (B26) describes all the spontaneous decay processes illustrated in Fig. 9(a),

$$\begin{aligned} \mathcal{D}_{\text{s}}[\hat{\rho}] = & \gamma_{\text{c}} \left(\mathcal{L}_{\hat{\sigma}_{03}\hat{\sigma}_{30}}[\hat{\rho}] + \frac{1}{2} \sum_{\alpha=\pm} \mathcal{L}_{\hat{\sigma}_{\alpha 4}\hat{\sigma}_{4\alpha}}[\hat{\rho}] \right) \\ & + \gamma_{\text{nc}} \left(\mathcal{L}_{\hat{\sigma}_{04}\hat{\sigma}_{40}}[\hat{\rho}] + \frac{1}{2} \sum_{\alpha=\pm} \mathcal{L}_{\hat{\sigma}_{\alpha 3}\hat{\sigma}_{3\alpha}}[\hat{\rho}] \right) \\ & + \gamma_{50} \mathcal{L}_{\hat{\sigma}_{05}\hat{\sigma}_{50}}[\hat{\rho}] + \gamma_{5\pm} \sum_{\alpha=\pm} \mathcal{L}_{\hat{\sigma}_{\alpha 5}\hat{\sigma}_{5\alpha}}[\hat{\rho}] \\ & + \gamma_{45} \mathcal{L}_{\hat{\sigma}_{54}\hat{\sigma}_{45}}[\hat{\rho}] + \gamma_{35} \mathcal{L}_{\hat{\sigma}_{53}\hat{\sigma}_{35}}[\hat{\rho}]. \end{aligned} \quad (\text{B28})$$

The factors 1/2 in the first two lines ensure that the total radiative decay rate of both states |3) and |4) is the same, namely, $\gamma_{\text{c}} + \gamma_{\text{nc}}$. Finally, the last term in the dissipator Eq. (B26) describes the additional fast dephasing of the excited-state manifold [79],

$$\mathcal{D}_{\phi}[\hat{\rho}] = \frac{\kappa_{\phi}}{\hbar^2} \mathcal{L}_{\hat{\sigma}_{44}\hat{\sigma}_{44}}[\hat{\rho}]. \quad (\text{B29})$$

Room temperature values for all the relevant additional rates appearing in the above master equation are given in Table II. Note that we neglect spontaneous (thermal) decay and absorption between the excited states |3) and |4), as these processes are negligible in comparison with the much faster spontaneous emission described by γ_{c} and γ_{nc} .

From the master equation (B24), we can obtain the equations of motion for the expected values of transition matrices, $\langle \hat{\sigma}_{\alpha\alpha'} \rangle = \rho_{\alpha\alpha'}$. Since all the processes involved in the dynamics are dissipative, the diagonal elements $\langle \hat{\sigma}_{\alpha\alpha} \rangle$ decouple from the coherences and form a closed 5×5 system, which we can write as

$$\frac{d}{dt} \begin{bmatrix} \langle \hat{\sigma}_{00} \rangle \\ \langle \hat{S}_z / \hbar \rangle \\ \langle \hat{\sigma}_{33} \rangle \\ \langle \hat{\sigma}_{44} \rangle \\ \langle \hat{\sigma}_{55} \rangle \end{bmatrix} = \overline{\overline{M}}_{\text{op}} \begin{bmatrix} \langle \hat{\sigma}_{00} \rangle \\ \langle \hat{S}_z / \hbar \rangle \\ \langle \hat{\sigma}_{33} \rangle \\ \langle \hat{\sigma}_{44} \rangle \\ \langle \hat{\sigma}_{55} \rangle \end{bmatrix} + \begin{bmatrix} \kappa_1 + \gamma_+ \\ \gamma_- \\ 0 \\ \Omega \\ 0 \end{bmatrix} \quad (\text{B30})$$

with a coefficient matrix

$$\overline{\overline{M}}_{\text{op}} = \begin{bmatrix} -\kappa_1 - 3\gamma_+ - \Omega & -\gamma_- & \gamma_{\text{c}} - \kappa_1 - \gamma_+ & \gamma_{\text{nc}} - \kappa_1 - \gamma_+ & \gamma_{50} - \kappa_1 - \gamma_+ \\ -3\gamma_- & -\kappa_1 - \gamma_+ - \Omega & -\gamma_- & -\gamma_- & -\gamma_- \\ \Omega & 0 & -\gamma_{\text{c}} - \gamma_{\text{nc}} - \gamma_{35} & 0 & 0 \\ -\Omega & 0 & -\Omega & -\gamma_{\text{c}} - \gamma_{\text{nc}} - \gamma_{45} - \Omega & -\Omega \\ 0 & 0 & \gamma_{35} & \gamma_{45} & -\gamma_{50} - 2\gamma_{5\pm} \end{bmatrix}. \quad (\text{B31})$$

The occupation of the levels $|+\rangle$ and $|-\rangle$ is obtained from the solution of the above equations through the norm conservation identity

$$\langle \hat{\sigma}_{\pm\pm} \rangle = \frac{1}{2} \left(1 - \langle \hat{\sigma}_{00} \rangle - \sum_{\alpha=3}^5 \langle \hat{\sigma}_{\alpha\alpha} \rangle \pm \langle \hat{S}_z / \hbar \rangle \right). \quad (\text{B32})$$

Note that the occupations depend neither on the frequencies ω_{α} of the states |3), |4), and |5), nor on the dephasing rate κ_{ϕ} . Since the spontaneous decay rates are fixed material

parameters (see Table II), the only additional parameter determining the occupation dynamics is the driving strength Ω . As evidenced by the red curve in Fig. 9(b), the steady-state

occupation of the ground state $|0\rangle$ increases as a function of Ω up to a maximum value $\langle\hat{\sigma}_{00}\rangle_{ss} \approx 0.8$, consistent with experimental observations [44,81]. For too large driving strengths the efficiency of the optical pumping decreases since the higher states $|3\rangle$, $|4\rangle$, and $|5\rangle$ become occupied in the steady state, as evidenced by the blue curve in Fig. 9(b). The optimal driving strength for optical pumping is $\Omega \approx 2\pi \times 10$ kHz, corresponding to an optical intensity of $I_d \approx 0.13$ GW m $^{-2}$,¹⁴ or, equivalently, to an optical power of $P_d \approx 3$ μ W at 532 nm focused through a lens of numerical aperture ~ 1.4 .

Equations of motion for the expected values of the coherences can analogously be obtained. Here we focus on the coherences of interest regarding the interaction with spin waves, namely, the coherences of the ground-state manifold whose evolution is given by

$$\frac{d\langle\hat{\sigma}_{0\pm}\rangle}{dt} = \left[-i\omega_{\pm} - \frac{\kappa_1 + 3\gamma_+ \mp \gamma_-}{2} - \frac{\kappa_2}{2} - \Omega \right] \langle\hat{\sigma}_{0\pm}\rangle, \quad (\text{B33})$$

$$\frac{d\langle\hat{\sigma}_{+-}\rangle}{dt} = [i(\omega_+ - \omega_-) - (\gamma_+ + \kappa_1) - 2\kappa_2 - \Omega] \langle\hat{\sigma}_{+-}\rangle. \quad (\text{B34})$$

These equations are, except for the factor proportional to Ω , identical to the corresponding equations in the absence of optical pumping, namely, Eqs. (B10) and (B11). Indeed, since the driving is incoherent, it contributes only to the decay of the coherences and does not result in any steady-state coherence, i.e.,

$$\langle\hat{\sigma}_{0\pm}\rangle_{ss} = \langle\hat{\sigma}_{+-}\rangle_{ss} = 0, \quad (\text{B35})$$

in analogy to an NV center in thermal equilibrium discussed in the previous section. Note that as a consequence, and regarding only the coherences above, an optically pumped NV center can be interpreted as a thermal NV center at an effective, lower, Ω -dependent temperature.

a. Two-time correlators of NV operators

Let us finally derive the two-time correlation functions of an optically pumped NV center. We consider first the correlation functions involving the coherences which, due to the convenient structure of Eqs. (B33) and (B34), can be easily derived using the quantum regression theorem:

$$\langle\hat{\sigma}_{0\pm}(t)\hat{O}(t-s)\rangle_{ss} = e^{-s[i\omega_{\pm} + (\kappa_1 + 3\gamma_+ \mp \gamma_- + \kappa_2)/2 + \Omega]} \langle\hat{\sigma}_{0\pm}\hat{O}\rangle_{ss}, \quad (\text{B36})$$

$$\langle\hat{\sigma}_{\pm 0}(t)\hat{O}(t-s)\rangle_{ss} = e^{-s[-i\omega_{\pm} + (\kappa_1 + 3\gamma_+ \mp \gamma_- + \kappa_2)/2 + \Omega]} \langle\hat{\sigma}_{\pm 0}\hat{O}\rangle_{ss}, \quad (\text{B37})$$

¹⁴Although not the case for the results in the main text, note that in the presence of spin waves the lifetimes of the NV centers, and hence the rates in the master equation Eq. (B24), might be significantly altered (see next sections). As a consequence the optimum driving intensity might be very different or, in extreme situations, optical pumping might even become unfeasible.

$$\langle\hat{\sigma}_{+-}(t)\hat{O}(t-s)\rangle_{ss} = e^{s[i(\omega_+ - \omega_-) - \kappa_1 - \gamma_+ - 2\kappa_2 - \Omega]} \langle\hat{\sigma}_{+-}\hat{O}\rangle_{ss}, \quad (\text{B38})$$

$$\langle\hat{\sigma}_{-+}(t)\hat{O}(t-s)\rangle_{ss} = e^{s[-i(\omega_+ - \omega_-) - \kappa_1 - \gamma_+ - 2\kappa_2 - \Omega]} \langle\hat{\sigma}_{-+}\hat{O}\rangle_{ss}. \quad (\text{B39})$$

Regarding the correlators involving the occupations, they obey the following equation of motion, which can be derived from Eq. (B30) using the quantum regression theorem:

$$\frac{d}{ds} \langle\hat{O}_1(t)\hat{v}_j(t+s)\hat{O}_2(t)\rangle_{ss} = \overline{\overline{M}}_{\text{op}} \langle\hat{O}_1(t)\hat{v}_j(t+s)\hat{O}_2(t)\rangle_{ss}. \quad (\text{B40})$$

In this equation, valid for $s \geq 0$, \hat{O}_1 and \hat{O}_2 are two arbitrary NV center operators, and \hat{v}_j ($j = 1, \dots, 5$) is the j component of the vector

$$\hat{v} \equiv \begin{bmatrix} \hat{\sigma}_{00} - \langle\hat{\sigma}_{00}\rangle_{ss} \\ \hat{S}_z/\hbar - \langle\hat{S}_z/\hbar\rangle_{ss} \\ \hat{\sigma}_{33} - \langle\hat{\sigma}_{33}\rangle_{ss} \\ \hat{\sigma}_{44} - \langle\hat{\sigma}_{44}\rangle_{ss} \\ \hat{\sigma}_{55} - \langle\hat{\sigma}_{55}\rangle_{ss} \end{bmatrix}. \quad (\text{B41})$$

The above differential equation has the following general solution:

$$\langle\hat{O}_1(t)\hat{v}_j(t+s)\hat{O}_2(t)\rangle_{ss} = \sum_{i=1}^5 e^{\lambda_i s} \Lambda_{ji} [\overline{\overline{\Lambda}}]^{-1} \langle\hat{O}_1\hat{v}_j\hat{O}_2\rangle_{ss} |j\rangle. \quad (\text{B42})$$

Here, λ_i are the eigenvalues of $\overline{\overline{M}}_{\text{op}}$ and $\overline{\overline{\Lambda}}$ a matrix whose i th column contains the corresponding eigenvector. The inverses of the real part of the eigenvalues, $1/\text{Re}[\lambda_i]$, determine the timescales at which the correlators decay to zero. We define the correlation time of the NV centers τ_{nv} as the largest of these timescales,

$$\tau_{\text{nv}} \equiv \max_i \left| \frac{1}{\text{Re}[\lambda_i]} \right| \sim (\kappa_1 + \gamma_+ + \Omega)^{-1}, \quad (\text{B43})$$

where the absolute value is taken to ensure positiveness, as $\text{Re}[\lambda_i] < 0$. The right-hand side is an estimation based on direct inspection of the decay rates of $\langle\hat{\sigma}_{00}\rangle$ and $\langle\hat{S}_z\rangle$ in Eqs. (B30) and (B31). The correlation time defined by Eq. (B43) represents an upper bound to the decay time of the two-time correlators involving the occupations $\hat{\sigma}_{\alpha\alpha}$, and its value is relevant for deriving the reduced dynamics of the spin waves in Appendix F. In Fig. 9(c), we display the correlation time (green curve) as a function of the driving strength Ω at $\mu_0 H_0 = 20$ mT and for the parameters in Tables I and II. The results do not change appreciably within the range of magnetic fields considered in this work. As evidenced by Fig. 9(c), optical pumping of the NV centers results in a reduction of the correlation time for the occupations. At optimal optical pumping conditions, $\Omega \approx 2\pi \times 10$ kHz the correlation times take values $\tau_{\text{nv}} \approx 50$ μ s, a decrease of three orders of magnitude with respect to a NV center in thermal equilibrium. Finally, the approximation on the right-hand side of Eq. (B43), namely, $\tau_{\text{nv}} \sim (\kappa_1 + \gamma_+ + \Omega)^{-1}$, is a reasonable order-of-magnitude estimation as shown by the dashed line in Fig. 9(c).

APPENDIX C: DERIVATION OF THE RESONANT SPIN WAVE-PARAMAGNETIC SPIN INTERACTION AND EXTENSION TO AN ENSEMBLE OF PARAMAGNETIC SPINS

In this section, we derive the resonant interaction Hamiltonian between a paramagnetic spin at a position \mathbf{r}_0 and the spin waves, Eq. (7), from the general form of the magnetic dipole interaction. We start by writing the magnetic dipole interaction between the paramagnetic spin and the spin wave magnetic field in the general form

$$\hat{V} = -\mu_0 \hat{\boldsymbol{\mu}}_{\text{ps}} \cdot [\hat{\mathbf{H}}(\mathbf{r}_0) - \mathbf{H}_0]. \quad (\text{C1})$$

Here, $\hat{\mathbf{H}}(\mathbf{r}_0)$ represents the total magnetic field operator. We subtract the applied field \mathbf{H}_0 whose effect, namely, the Zeeman splitting of the NV transitions, has already been included in \hat{H}_{ps} , Eq. (B1). The resulting field $\hat{\mathbf{H}}(\mathbf{r}_0) - \mathbf{H}_0$ corresponds to the field generated by the spin waves at position \mathbf{r}_0 , in principle up to arbitrary order in magnon operators. As we will see below, for studying the spin wave induced modification of *both* paramagnetic spin timescales, namely, T_1 and T_2^* , the field must be included up to second order in magnon operators, i.e.,

$$\hat{\mathbf{H}}(\mathbf{r}) - \mathbf{H}_0 \approx \hat{\mathbf{h}}^{(2)}(\mathbf{r}) = \hat{\mathbf{h}}(\mathbf{r}) + \delta\hat{\mathbf{h}}(\mathbf{r}), \quad (\text{C2})$$

where we have used the definition of the spin wave field up to second order, $\hat{\mathbf{h}}^{(2)}(\mathbf{r})$, as given by Eq. (A102). The first and second field contributions above are linear and quadratic in magnon operators, respectively, and have been calculated in Appendix A. We can consider each contribution separately by splitting the interaction Hamiltonian into linear and quadratic parts as

$$\hat{V} = \hat{V}_1 + \hat{V}_2, \quad (\text{C3})$$

with

$$\hat{V}_1 \equiv -\mu_0 \hat{\boldsymbol{\mu}}_{\text{ps}} \cdot \hat{\mathbf{h}}(\mathbf{r}_0) \quad (\text{C4})$$

and

$$\hat{V}_2 \equiv -\mu_0 \hat{\boldsymbol{\mu}}_{\text{ps}} \cdot \delta\hat{\mathbf{h}}(\mathbf{r}_0). \quad (\text{C5})$$

Let us focus on the linear interaction term \hat{V}_1 . By using the identity $\hat{\boldsymbol{\mu}}_{\text{ps}} = -|\gamma|\hat{\mathbf{S}}$, we cast this interaction as

$$\hat{V}_1 = \sum_{\beta} \hat{s}_{\beta} \left[g_{\beta}^{+} \frac{\hat{S}_{+}}{\sqrt{2}} + g_{\beta}^{-} \frac{\hat{S}_{-}}{\sqrt{2}} + g_{\beta}^z \hat{S}_z \right] + \text{H.c.} \quad (\text{C6})$$

Here, we have introduced the expression for the spin wave field $\hat{\mathbf{h}}(\mathbf{r})$, Eq. (A70), and defined the raising and lowering spin operators

$$\hat{S}_{\pm} \equiv \hat{S}_x \pm i\hat{S}_y = \hbar\sqrt{2}(\hat{\sigma}_{\pm 0} + \hat{\sigma}_{0\mp}) \quad (\text{C7})$$

as well as the coupling rates

$$g_{\beta}^k \equiv \mu_0 |\gamma_s| \mathcal{M}_{0\beta} \mathbf{e}_k^{\dagger} \cdot \mathbf{h}_{\beta}(\mathbf{r}_0). \quad (\text{C8})$$

In the interaction picture with respect to the free Hamiltonian $\hat{H}_{\text{ps}} + \hat{H}_{\text{sw}}$ [see Eq. (2)], the above interaction takes the

form

$$\begin{aligned} \frac{\hat{V}_1(t)}{\hbar} = & \sum_{\beta} \hat{s}_{\beta} e^{-i\omega_{\beta} t} [g_{\beta}^{+} (\hat{\sigma}_{+0} e^{i\omega_{+} t} + \hat{\sigma}_{0-} e^{-i\omega_{-} t}) \\ & + g_{\beta}^{-} (\hat{\sigma}_{0+} e^{-i\omega_{+} t} + \hat{\sigma}_{-0} e^{i\omega_{-} t}) + g_{\beta}^z \hat{S}_z] + \text{H.c.} \quad (\text{C9}) \end{aligned}$$

We now undertake a rotating wave approximation [68,90], i.e., we neglect all the rapidly oscillating terms to obtain

$$\begin{aligned} \frac{\hat{V}_1(t)}{\hbar} \approx & \sum_{\beta} \hat{s}_{\beta} e^{-i\omega_{\beta} t} [g_{\beta}^{+} \hat{\sigma}_{+0} e^{i\omega_{+} t} \\ & + g_{\beta}^{-} \hat{\sigma}_{-0} e^{i\omega_{-} t} + g_{\beta}^z \hat{S}_z] + \text{H.c.} \quad (\text{C10}) \end{aligned}$$

This approximation is valid provided that

$$g_{\beta}^{\pm}, |\omega_{\beta} - \omega_{\pm}| \ll |\omega_{\beta} + \omega_{\pm}|. \quad (\text{C11})$$

These conditions are well satisfied in our system due to the lower cutoff for the spin wave bands [see Fig. 1(b)], as opposed to other reservoirs where it might be compromised by the presence of low-frequency modes [66].

The Hamiltonian can be further simplified by noting that only the spin waves with a low wave number k_{\parallel} will be significantly coupled to the transitions of the paramagnetic spin, as the coupling strengths $g_{\beta}^k \propto \mathbf{e}_k^{\dagger} \cdot \mathbf{h}_{\beta}(\mathbf{r}_0)$ decay exponentially with the spin wave wavenumber [see e.g., Eq. (A61)]. For $\gamma_s \sim \gamma$, and in the range of slab thicknesses and applied fields we focus on in this work, namely, $d \gtrsim 50$ nm and $\mu_0 H_0 \sim 10$ –35 mT, the spin wave modes with low wave number, say for definiteness $k_{\parallel} d < 1$, are far detuned with respect to the $|0\rangle \leftrightarrow |+\rangle$ transition frequency, by a detuning of at least $0.1\omega_M \sim 2\pi \times 0.5$ GHz. This is illustrated in Fig. 10(a), where we display the transition frequencies ω_{\pm} for the specific case of NV centers as a function of applied field, and compare them with the frequency range spanned by the first three spin wave bands in the low-wave-number range $k_{\parallel} d \in [0, 1]$. As evidenced by this figure, the spin wave modes near resonance with ω_{+} are high-wave-number modes, thus resulting in very weak coupling rates. Conversely, the lower NV transition $|0\rangle \leftrightarrow |-\rangle$ is resonant with low-wave-number spin waves for a wide range of applied fields H_0 . We thus conclude that

$$|\omega_{\beta} - \omega_{-}|_{(k_{\parallel} d \lesssim 1)} \ll |\omega_{\beta} - \omega_{+}|_{(k_{\parallel} d \lesssim 1)}, \quad \omega_{\beta}|_{(k_{\parallel} d \lesssim 1)}. \quad (\text{C12})$$

Noting that the condition Eq. (C11) is valid also for g_{β}^z , i.e., $g_{\beta}^z \ll \omega_{\beta}$, this allows us to discard the negligible terms $\propto \hat{S}_z, \hat{\sigma}_{+0}, \hat{\sigma}_{0+}$ in the interaction Hamiltonian (C10). Back in the Schrödinger picture, we can finally write the first-order interaction as

$$\hat{V}_1 \approx \hbar \sum_{\beta} (g_{\beta}^{-} \hat{s}_{\beta} \hat{\sigma}_{-0} + \text{H.c.}). \quad (\text{C13})$$

We now follow a similar procedure for the nonlinear interaction term \hat{V}_2 . By introducing the expression for the second-order field correction (A103), we cast this contribution as

$$\begin{aligned} \hat{V}_2 = & \sum_{\beta\beta'} \hat{s}_{\beta} \hat{s}_{\beta'} \left[\tilde{g}_{\beta\beta'}^{'+} \frac{\hat{S}_{+}}{\sqrt{2}} + \tilde{g}_{\beta\beta'}^{-} \frac{\hat{S}_{-}}{\sqrt{2}} + \tilde{g}_{\beta\beta'}^z \hat{S}_z \right] + \sum_{\beta\beta'} \hat{s}_{\beta} \hat{s}_{\beta'}^{\dagger} \\ & \times \left[\tilde{g}_{\beta\beta'}^{+} \frac{\hat{S}_{+}}{\sqrt{2}} + \tilde{g}_{\beta\beta'}^{-} \frac{\hat{S}_{-}}{\sqrt{2}} + \tilde{g}_{\beta\beta'}^z \hat{S}_z \right] + \text{H.c.}, \quad (\text{C14}) \end{aligned}$$

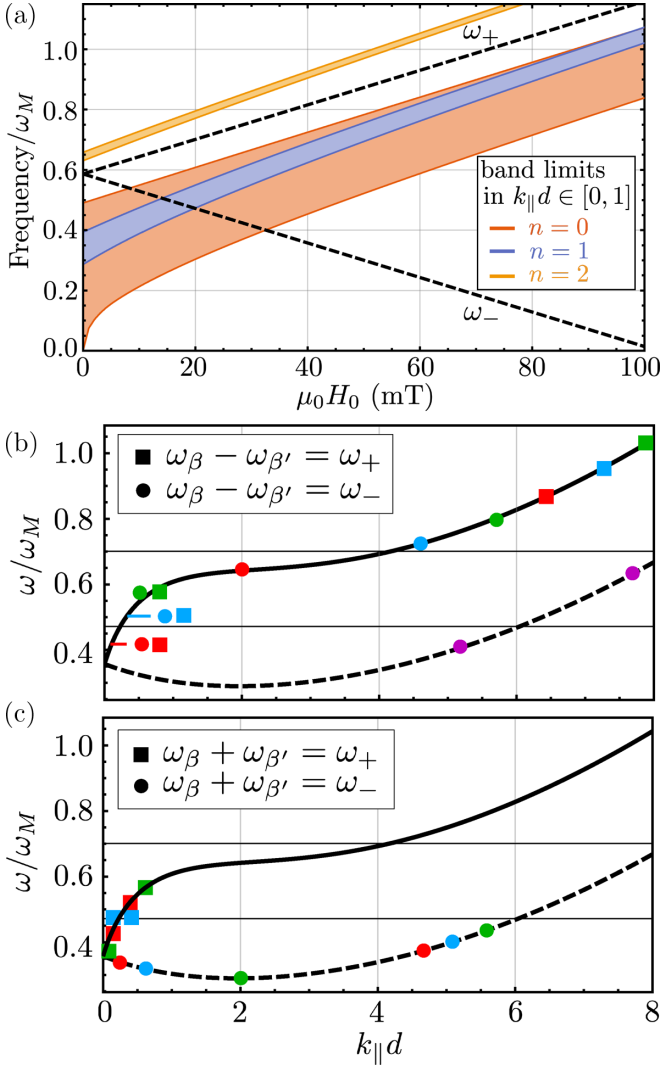


FIG. 10. (a) Frequencies of the two transitions of the NV center (dashed lines) as a function of external field H_0 . The three colored stripes represent the range of spin wave eigenfrequencies spanned by the bands $n = 0, 1$, and 2 corresponding to significant coupling to the NV center, i.e., in the low-wave-number region $0 \leq k_{\parallel}d \leq 1$. Specifically, the stripes correspond to the regions $\min_{\phi_k, k_{\parallel}} \omega_n(k_{\parallel}, \phi_k)|_{k_{\parallel}d \in [0, 1]} \leq \omega \leq \max_{\phi_k, k_{\parallel}} \omega_n(k_{\parallel}, \phi_k)|_{k_{\parallel}d \in [0, 1]}$, for $d = 200$ nm. [(b) and (c)] Illustration of the three-operator resonance conditions appearing in the nonlinear interaction term \hat{V}_2 . In each panel, symbols of the same color mark the energies of magnon pairs β and β' whose frequency difference (a) or sum (b) is equal to ω_+ (squares) or ω_- (circles). The solid and dashed lines represent the $n = 0$ spin wave bands in Damon-Eshbach and parallel propagation, respectively, whereas the horizontal gridlines mark the frequencies ω_+ and ω_- . For this figure, we choose $d = 200$ nm and $\mu_0 H_0 = 20$ mT.

where

$$\tilde{g}_{\beta\beta'}^k \equiv \mu_0 |\gamma_s| \mathbf{e}_k^{\dagger} \cdot \mathbf{X}_{\beta\beta'}^+(\mathbf{r}_0) \quad (\text{C15})$$

and

$$\tilde{g}_{\beta\beta'}^k \equiv \mu_0 |\gamma_s| \mathbf{e}_k^{\dagger} \cdot \mathbf{X}_{\beta\beta'}^-(\mathbf{r}_0), \quad (\text{C16})$$

with the vectors $\mathbf{X}_{\beta\beta'}^{\pm}(\mathbf{r})$ defined in Eq. (A104). We now transform \hat{V}_2 to the interaction picture with respect to $\hat{H}_{\text{sw}} + \hat{H}_{\text{ps}}$, and undertake the rotating wave approximation.

(1) First, we neglect the rapidly oscillating terms at frequencies $\omega_{\beta} + \omega_{\beta'}$ and $\omega_{\beta} + \omega_{\beta'} + \omega_{\pm}$. This is justified on the basis of the first rotating wave approximation (C11) and on the observation that all the coupling rates in the above Hamiltonian are second order and thus smaller than the first-order rates g_{β}^k .

(2) Second, we neglect the terms oscillating at frequencies $\omega_{\beta} - \omega_{\beta'} + \omega_{\pm}$, since they are resonant only for magnon pairs β and β' whose frequency difference is equal to the transition frequencies ω_{\pm} of the paramagnetic spin. It can be checked that, in the range of parameters we focus on in this work, magnon pairs fulfilling this resonance condition have very different wavenumbers, i.e., $(k_{\parallel} - k'_{\parallel})d \gg 1$, see Fig. 10(b) for an example in the case of NV centers. These terms will thus be very weakly coupled since the coupling rates decay exponentially with this difference, i.e., since $\tilde{g}_{\beta\beta'}^k \propto \exp(-l|\mathbf{k}_{\parallel} - \mathbf{k}'_{\parallel}|)$ [see Eqs. (A105) and (A108)].

(3) Third, we neglect the terms oscillating at frequencies $\omega_{\beta} + \omega_{\beta'} - \omega_{\pm}$, since they are resonant only for magnon pairs β and β' whose frequencies add up to the paramagnetic spin transition frequency ω_{\pm} . As evidenced by the circles in Fig. 10(c), which show the specific case of NV centers, the magnon pairs fulfilling this resonance condition also fulfill $(k_{\parallel} + k'_{\parallel})d \gg 1$, their coupling rate $\tilde{g}_{\beta\beta'}^k \propto \exp(-l|\mathbf{k}_{\parallel} + \mathbf{k}'_{\parallel}|)$ thus becoming negligible [see Eqs. (A105) and (A108)].

(4) Two kind of terms remain at this point: on the one hand, terms $\propto \hat{s}_{\beta}\hat{s}_{\beta'}\hat{\sigma}_{\pm 0}$, oscillating at frequencies $\omega_{\beta} + \omega_{\beta'} - \omega_{\pm}$, whose resonance condition is met for several low-wavenumber magnon pairs [square symbols in Fig. 10(c)]. On the other hand, terms $\propto \hat{s}_{\beta}\hat{s}_{\beta'}^{\dagger}\hat{S}_z$, oscillating at $\omega_{\beta} - \omega_{\beta'}$, whose resonance condition is met for near-resonant magnon pairs of an arbitrary wave number. The terms oscillating at $\omega_{\beta} + \omega_{\beta'} - \omega_{\pm}$ are neglected for the following reasons: (a) their coupling rate $\tilde{g}_{\beta\beta'}^k \propto \exp(-l|\mathbf{k}_{\parallel} + \mathbf{k}'_{\parallel}|)$ decays much faster than the coupling rate $\tilde{g}_{\beta\beta'}^k \propto \exp(-l|\mathbf{k}_{\parallel} - \mathbf{k}'_{\parallel}|)$ of the terms $\propto \hat{s}_{\beta}\hat{s}_{\beta'}^{\dagger}\hat{S}_z$, thus making the interaction relevant over a much narrower wave-number range. (b) While the terms proportional to \hat{S}_z describe a new spin wave induced decoherence mechanism (dephasing), the terms containing $\hat{\sigma}_{\pm 0}$ represent a small correction to the decay lifetime T_1 , whose main effect is already accounted for at first order (i.e., by \hat{V}_1).

Under the above simplifications, the second-order correction to the spin wave-paramagnetic spin interaction Eq. (C14) reduces to

$$\hat{V}_2 = \hat{S}_z \sum_{\beta\beta'} [\hat{s}_{\beta}\hat{s}_{\beta'}^{\dagger}\tilde{g}_{\beta\beta'}^z + \text{H.c.}]. \quad (\text{C17})$$

Finally, by using the commutation relations (A68) and the property (A110), we can write the above expression in the form

$$\hat{V}_2 = \hat{S}_z \sum_{\beta\beta'} \hat{s}_{\beta}^{\dagger}\hat{s}_{\beta'}\tilde{g}_{\beta\beta'}, \quad (\text{C18})$$

where we define

$$\tilde{g}_{\beta\beta'} = \tilde{g}_{\beta\beta'}^* \equiv \tilde{g}_{\beta\beta'}^z + \tilde{g}_{\beta\beta'}^*. \quad (\text{C19})$$

By introducing Eqs. (C13) and (C18) into Eq. (C3), we obtain the interaction Hamiltonian given by Eq. (7) in the main text.

The equations of motion derived for a single paramagnetic spin in Appendices B and C can be generalized to an ensemble of paramagnetic spins situated at positions \mathbf{r}_j , $j = 1, \dots, N$. We assume the paramagnetic spins to be independent, that is, we neglect any interaction between them, either direct (e.g., dipole-dipole) or mediated by their corresponding thermal reservoirs. This approximation is valid for the densities of NV centers considered in this work ($\leq 10^5 \mu\text{m}^{-3}$), as experiments show no significant dipole-dipole-induced modification of the coherence times T_2^* for ensembles of NV centers within this range of densities [76,77]. Under this assumption the Hamiltonian of the paramagnetic spins and the interaction with the spin waves are written as

$$\hat{H}_{\text{ps}} = \sum_{j=1}^N \hat{H}_{\text{ps}}^{(j)}; \quad \hat{V} = \sum_{j=1}^N \hat{V}^{(j)}. \quad (\text{C20})$$

The expressions of $\hat{H}_{\text{ps}}^{(j)}$ and $\hat{V}^{(j)}$ are identical to Eqs. (6) and (7), respectively, i.e.,

$$\hat{H}_{\text{ps}}^{(j)} = \hbar \sum_{\alpha=\pm} \omega_{\alpha}^{(j)} \hat{\sigma}_{\alpha\alpha}^{(j)} \quad (\text{C21})$$

and

$$\hat{V}^{(j)} = \hbar \sum_{\beta} (g_{j\beta} \hat{\delta}_{\beta} \hat{\sigma}_{-0}^{(j)} + \text{H.c.}) + \hat{S}_z^{(j)} \sum_{\beta\beta'} \tilde{g}_{j\beta\beta'} \hat{\delta}_{\beta}^{\dagger} \hat{\delta}_{\beta'}, \quad (\text{C22})$$

this time with paramagnetic spin-dependent transition matrices $\hat{\sigma}_{\alpha\alpha'}^{(j)} \equiv |\alpha\rangle_j \langle\alpha'|$, transition frequencies $\omega_{\alpha}^{(j)}$, and coupling rates $g_{j\beta}$ and $\tilde{g}_{j\beta\beta'}$. These coupling rates are given respectively by identical expressions as Eqs. (9) and (10) under the substitution $\mathbf{r}_0 \rightarrow \mathbf{r}_j$, i.e.,

$$g_{j\beta} \equiv \mu_0 |\gamma_s| \mathcal{M}_{0\beta} \int d^3\mathbf{r} [\mathbf{e}_-^* \cdot \overline{\overline{\mathcal{G}}}(\mathbf{r}_j - \mathbf{r}) \cdot \mathbf{m}_{\beta}(\mathbf{r})], \quad (\text{C23})$$

$$\begin{aligned} \tilde{g}_{j\beta\beta'} &= -\mu_0 |\gamma_s| \frac{\mathcal{M}_{0\beta} \mathcal{M}_{0\beta'}}{M_S} \int d^3\mathbf{r} [\mathbf{m}_{\beta}^*(\mathbf{r}) \cdot \mathbf{m}_{\beta'}(\mathbf{r})] \\ &\times \text{Re}[\mathbf{e}_z \cdot \overline{\overline{\mathcal{G}}}(\mathbf{r}_j - \mathbf{r}) \cdot \mathbf{e}_z]. \end{aligned} \quad (\text{C24})$$

The dissipation of the NV centers is generalized in a similar way,

$$\begin{aligned} \mathcal{D}_{\text{ps}}[\hat{\rho}] &= \sum_j \frac{\kappa_{2j}}{\hbar^2} \mathcal{L}_{\hat{S}_z^{(j)} \hat{S}_z^{(j)}}[\hat{\rho}] + \sum_j \sum_{\alpha=\pm} \\ &\times \kappa_{1j} (\bar{n}_{\alpha}^{(j)} \mathcal{L}_{\hat{\sigma}_{\alpha 0}^{(j)} \hat{\sigma}_{0\alpha}^{(j)}}[\hat{\rho}] + (\bar{n}_{\alpha}^{(j)} + 1) \mathcal{L}_{\hat{\sigma}_{0\alpha}^{(j)} \hat{\sigma}_{\alpha 0}^{(j)}}[\hat{\rho}]), \end{aligned} \quad (\text{C25})$$

with $\bar{n}_{\alpha}^{(j)} = [\exp(\hbar\omega_{\alpha}^{(j)}/k_B T) - 1]^{-1}$. Note that, although in the above expressions we have allowed the characteristic rates ω_{\pm} , κ_1 , and κ_2 to be different for each paramagnetic spin, in this paper, we consider identical paramagnetic spins for the sake of simplicity.

APPENDIX D: TRACING OUT PROCEDURE

In this Appendix, we summarize briefly the open quantum systems techniques employed to obtain the effective dynamics

in the successive appendices. We begin by considering a system and a bath with free Hamiltonians \hat{H}_S and \hat{H}_B respectively, which interact through a general interaction potential \hat{V} . The total Hamiltonian of the compound system+bath is

$$\hat{H} = \hat{H}_S + \hat{H}_B + \hat{V}. \quad (\text{D1})$$

Here we assume for simplicity that \hat{H} is time-independent. We also assume that system and bath form a closed system, so that the dynamics of the total density matrix $\hat{\rho}_T$ is given by the Von Neumann equation

$$\dot{\hat{\rho}}_T = -\frac{i}{\hbar} [\hat{H}, \hat{\rho}_T]. \quad (\text{D2})$$

The procedure below can be generalized to the case where system and/or bath are open, i.e., they undergo additional dissipative dynamics, in the case where the baths generating this dynamics are independent.¹⁵ In the interaction picture with respect to $\hat{H}_S + \hat{H}_B$, we rewrite the von Neumann equation in integro-differential form as

$$\begin{aligned} \dot{\hat{\rho}}_T &= -\frac{i}{\hbar} [\hat{V}(t), \hat{\rho}_T(0)] \\ &- \frac{1}{\hbar^2} \int_0^t ds [\hat{V}(t), [\hat{V}(t-s), \hat{\rho}_T(t-s)]]. \end{aligned} \quad (\text{D3})$$

The above equation is still exact, but cast in a suitable form for approximations.

1. Born-Markov master equation

The most usual tracing out procedure [68] consists on the following steps: (i) undertaking the weak-coupling or Born approximation $\hat{\rho}_T(t) \approx \hat{\rho}(t) \otimes \hat{\rho}_{\text{ss}}$ with $\hat{\rho}(t)$ the reduced density matrix of the system and $\hat{\rho}_{\text{ss}}$ the steady-state density matrix of the bath. (ii) Undertaking the Markov approximation by taking $\hat{\rho}(t-s) \approx \hat{\rho}(t)$ inside the integral. The Markov approximation is justified if the two-time correlators of bath operators, i.e., the correlators appearing in Eq. (D11), decay with the delay s much faster than the timescale associated to the evolution of the density matrix in the interaction picture [68]. In the following sections, we will check the validity of the Markov approximation in our system. (iii) Taking the partial trace over the bath modes and assuming $\text{Tr}_B[\hat{V}(t), \hat{\rho}_T(0)] = 0$.¹⁶ As a result, the following equation of motion for the system density matrix is obtained,

$$\dot{\hat{\rho}} \approx -\frac{1}{\hbar^2} \text{Tr}_B \int_0^{\infty} ds [\hat{V}(t), [\hat{V}(t-s), \hat{\rho}(t) \otimes \hat{\rho}_{\text{ss}}]]. \quad (\text{D4})$$

The above equation can then be manipulated by writing the interaction potential in the form

$$\frac{1}{\hbar} \hat{V}(t) = \sum_{\alpha} \hat{O}_{s,\alpha}(t) \otimes \hat{B}_{\alpha}(t) + \text{H.c.}, \quad (\text{D5})$$

¹⁵This is achieved by means of projection operator techniques [68]. For a derivation using a similar system as ours, see, e.g., Ref [84].

¹⁶This condition can always be fulfilled if one writes $\hat{V} = \hat{V}' - \text{Tr}_B[\hat{V}] + \text{Tr}_B[\hat{V}]$ and re-absorbs the second term into the system Hamiltonian. One can then work with the interaction \hat{V}' which by definition fulfills $\text{Tr}_B[\hat{V}'] = 0$.

with $\hat{O}_{s,\alpha}(t)$ and $\hat{B}_\alpha(t)$ being system and bath operators, respectively. We choose the above representation such that the system operators $\hat{O}_{s,\alpha}(t)$ in the interaction picture always evolve with a trivial phase, i.e.,

$$\hat{O}_{s,\alpha}(t) = \hat{O}_{s,\alpha} e^{-i\Omega_\alpha t} \quad (\text{D6})$$

with $\hat{O}_{s,\alpha}$ the corresponding Schrödinger Picture operator and $\Omega_\alpha \in \mathbb{R}$. By introducing Eq. (D5) into Eq. (D4) and assuming $[\hat{H}_B, \hat{\rho}_{ss}] = 0$, we can cast the master equation in the convenient Lindblad form [68]. In the Schrödinger picture, this Lindblad master equation reads

$$\begin{aligned} \dot{\hat{\rho}} = & -\frac{i}{\hbar} [\hat{H}_S + \hat{H}_{\text{eff}}, \hat{\rho}] + \sum_{\alpha\alpha'} \left\{ \Gamma_{\alpha\alpha'}^{(n)} \mathcal{L}_{\hat{O}_{s,\alpha'} \hat{O}_{s,\alpha}^\dagger} [\hat{\rho}] \right. \\ & \left. + \Gamma_{\alpha\alpha'}^{(a)} \mathcal{L}_{\hat{O}_{s,\alpha'}^\dagger \hat{O}_{s,\alpha}} [\hat{\rho}] + \left(\Gamma_{\alpha\alpha'}^{(s)} \mathcal{L}_{\hat{O}_{s,\alpha'} \hat{O}_{s,\alpha}} [\hat{\rho}] + \text{H.c.} \right) \right\}. \quad (\text{D7}) \end{aligned}$$

The bath-induced coherent dynamics is captured by the effective Hamiltonian

$$\begin{aligned} \hat{H}_{\text{eff}} = & \hbar \sum_{\alpha\alpha'} G_{\alpha\alpha'}^a \hat{O}_{s,\alpha} \hat{O}_{s,\alpha'}^\dagger + G_{\alpha\alpha'}^n \hat{O}_{s,\alpha}^\dagger \hat{O}_{s,\alpha} \\ & + \left(G_{\alpha\alpha'}^s \hat{O}_{s,\alpha} \hat{O}_{s,\alpha'} + \text{H.c.} \right), \quad (\text{D8}) \end{aligned}$$

whereas the dissipative dynamics is represented by the Lindblad superoperators, defined in Eq. (12). The rates involved in the master equation can be written in compact form as

$$\begin{bmatrix} \Gamma_{\alpha\alpha'}^{(n)} \\ \Gamma_{\alpha\alpha'}^{(a)} \\ \Gamma_{\alpha\alpha'}^{(s)} \end{bmatrix} \equiv 2\pi \begin{bmatrix} \bar{S}_{\alpha\alpha'}^{(n)}(\Omega_{\alpha'}) + \bar{S}_{\alpha'\alpha}^{(n)*}(\Omega_\alpha) \\ \bar{S}_{\alpha\alpha'}^{(a)}(-\Omega_{\alpha'}) + \bar{S}_{\alpha'\alpha}^{(a)*}(-\Omega_\alpha) \\ \bar{S}_{\alpha\alpha'}^{(-)}(\Omega_{\alpha'}) + \bar{S}_{\alpha'\alpha}^{(+)*}(-\Omega_\alpha) \end{bmatrix} \quad (\text{D9})$$

and

$$\begin{bmatrix} G_{\alpha\alpha'}^n \\ G_{\alpha\alpha'}^a \\ G_{\alpha\alpha'}^s \end{bmatrix} \equiv -i\pi \begin{bmatrix} \bar{S}_{\alpha\alpha'}^{(n)}(\Omega_{\alpha'}) - \bar{S}_{\alpha'\alpha}^{(n)*}(\Omega_\alpha) \\ \bar{S}_{\alpha\alpha'}^{(a)}(-\Omega_{\alpha'}) - \bar{S}_{\alpha'\alpha}^{(a)*}(-\Omega_\alpha) \\ \bar{S}_{\alpha\alpha'}^{(-)}(\Omega_{\alpha'}) - \bar{S}_{\alpha'\alpha}^{(+)*}(-\Omega_\alpha) \end{bmatrix}. \quad (\text{D10})$$

Here, we define the one-sided power spectral densities of the bath, that capture the whole effect of the bath on the system dynamics, as

$$\begin{bmatrix} \bar{S}_{\alpha\alpha'}^{(n)}(\omega) \\ \bar{S}_{\alpha\alpha'}^{(a)}(\omega) \\ \bar{S}_{\alpha\alpha'}^{(+)}(\omega) \\ \bar{S}_{\alpha\alpha'}^{(-)}(\omega) \end{bmatrix} \equiv \int_0^\infty \frac{ds}{2\pi} e^{i\omega s} \begin{bmatrix} \langle \hat{B}_\alpha^\dagger(t) \hat{B}_{\alpha'}(t-s) \rangle_{ss} \\ \langle \hat{B}_\alpha(t) \hat{B}_{\alpha'}^\dagger(t-s) \rangle_{ss} \\ \langle \hat{B}_\alpha^\dagger(t) \hat{B}_{\alpha'}^\dagger(t-s) \rangle_{ss} \\ \langle \hat{B}_\alpha(t) \hat{B}_{\alpha'}(t-s) \rangle_{ss} \end{bmatrix}. \quad (\text{D11})$$

The above expressions are very general and, in the following sections, we will apply them to the two cases detailed in the main text.

2. Frozen bath model

The Born-Markov master equation derived above is valid when the bath correlation times are much shorter than the typical timescales associated with the system-bath interaction. It is also possible to obtain effective dynamics in the opposite limit, the so-called ‘‘frozen bath’’ regime [131]. In this regime, the evolution of the bath is much slower than the timescale associated to the system evolution in the interaction picture.

In this limit, the effective dynamics can be obtained directly from Eq. (D2), by undertaking the Born approximation and by substituting [131,132]

$$\hat{V}(t) \approx \text{Tr}_B[\hat{V}(t)]. \quad (\text{D12})$$

Within this approximation the bath is perceived, from the point of view of the system, as a stationary driving term given by the time-independent (‘‘frozen’’) expected value of the interaction potential. The frozen bath regime is not common in theory of open quantum systems as, in this limit, the bath does not induce any dissipation in the system as we will see below. However, we will make use of this regime to include the effect of the slow occupation dynamics of the NV center on the spin wave master equation, in Sec. III and Appendix F.

APPENDIX E: EFFECTIVE DYNAMICS OF PARAMAGNETIC SPINS

In this section, we apply the general formalism derived in Appendix D to derive the effective dynamics of a system of paramagnetic spins interacting with a spin wave bath. Since the derivation, specifically the justification of the Markov approximation, relies on the particular values of T_1 and T_2^* , we take the specific values for NV centers and will for simplicity refer to the paramagnetic spins as ‘‘NV centers’’ in this section. The results derived below hold for any species of paramagnetic spin with similar values of T_1 and T_2^* . Extending our derivation to other paramagnetic spins is also possible. This Appendix is organized as follows: first, we provide the master equation for the NV centers and give the expressions for all the involved rates in Appendix E 1. In the following sections, we analyze the different effective dynamics separately: in Appendix E 2, we study the modification of the occupation (T_1) and coherence (T_2^*) lifetimes for a single NV center. Then, in Appendix E 3, we derive the expressions for the frequency shift and spin wave induced force analyzed in the main text. Finally, in Appendix E 4, we analyze the spin wave-mediated couplings between different NV centers in an ensemble.

1. Derivation of the general master equation and equations of motion

We consider for generality an ensemble of NV centers at arbitrary positions \mathbf{r}_j outside the YIG film. Our starting point is the interaction Hamiltonian in the Interaction Picture, given by

$$\begin{aligned} \hat{V} = & \hat{V}_1 + \hat{V}_2 \\ = & \sum_{j\beta} g_{j\beta} \hat{s}_\beta(t) \hat{\sigma}_{-0}^{(j)} e^{i\omega t} + \text{H.c.} \\ & + \sum_j \frac{\hat{S}_z^{(j)}}{\hbar} \frac{1}{2} \sum_{\beta\beta'} \tilde{g}_{j\beta\beta'} \hat{s}_\beta^\dagger(t) \hat{s}_{\beta'}(t) + \text{H.c.} \quad (\text{E1}) \end{aligned}$$

with $\hat{s}_\beta(t) = \hat{s}_\beta \exp(-i\omega_\beta t)$. As shown in Appendix A 5, the spin waves are governed by the master equation (A72), whose steady state is thermal. By applying the quantum regression formula [90], one can prove that the two-time correlators between three magnon operators cancel out in a thermal

state:

$$\langle \hat{s}_\beta(t) \hat{s}_{\beta'}^\dagger(t-s) \hat{s}_{\beta''}(t-s) \rangle_{ss} = 0 \quad \forall s, \quad (\text{E2})$$

$$\langle \hat{s}_\beta^\dagger(t) \hat{s}_{\beta'}^\dagger(t-s) \hat{s}_{\beta''}(t-s) \rangle_{ss} = 0 \quad \forall s. \quad (\text{E3})$$

As a consequence, the two terms in the interaction, \hat{V}_1 and \hat{V}_2 , are independent from each other and can be treated separately. The two-time correlators of the magnon operators appearing on each of these terms decay at similar rates $\sim \gamma_\beta$, whereas the system evolution in the interaction picture is dominated by the timescale $\sim T_2^*$. We treat both interaction terms within the Born-Markov approximation, valid for $\gamma_\beta T_2^* \gg 1$. This condition is well fulfilled for all spin wave bands with $n > 0$. The lowest band $n = 0$ lies at the boundary of this validity regime $\gamma_\beta T_2^* \approx 1$, and hence small non-Markovian corrections to the effective dynamics of the NV centers could be expected, especially for NV transition frequencies near the lower cutoff of a spin wave band [133]. Although outside the scope of our work, exploring these dynamics beyond the Markov approximation is an interesting outlook to our work.¹⁷

Under the above approximations, the resulting master equation for the ensemble of NV centers in the Schrödinger picture reads

$$\begin{aligned} \frac{d}{dt} \hat{\rho}_{ps} = & -\frac{i}{\hbar} [\hat{H}_{ps} + \hat{H}_{\text{eff},1} + \hat{H}_{\text{eff},2}, \hat{\rho}_{ps}] + \mathcal{D}_{ps}[\hat{\rho}_{ps}] \\ & + \mathcal{D}_{\text{op}}[\hat{\rho}_{ps}] + \mathcal{D}_1[\hat{\rho}_{ps}] + \mathcal{D}_2[\hat{\rho}_{ps}]. \end{aligned} \quad (\text{E4})$$

where the subindices 1 and 2 indicate the contributions stemming from \hat{V}_1 and \hat{V}_2 , respectively. Let us first focus on the contribution from \hat{V}_1 . By applying the general formalism of Appendix D, we obtain an effective Hamiltonian

$$\begin{aligned} \frac{1}{\hbar} \hat{H}_{\text{eff},1} = & \sum_{j \neq j'} G_{jj'}^a \hat{\sigma}_{-0}^{(j)} \hat{\sigma}_{0-}^{(j')} + G_{jj'}^n \hat{\sigma}_{0-}^{(j)} \hat{\sigma}_{-0}^{(j')} \\ & + \sum_j \sum_{\alpha=\pm} \delta_{1\alpha}^{(j)} \hat{\sigma}_{\alpha\alpha}^{(j)}, \end{aligned} \quad (\text{E5})$$

with

$$\begin{bmatrix} G_{jj'}^a \\ G_{jj'}^n \end{bmatrix} = \sum_\beta \frac{-\Delta_\beta}{\Delta_\beta^2 + (\gamma_\beta/2)^2} \begin{bmatrix} (1 + \bar{n}_\beta) g_{j\beta} g_{j'\beta}^* \\ -\bar{n}_\beta g_{j\beta}^* g_{j'\beta} \end{bmatrix}, \quad (\text{E6})$$

where $\Delta_\beta \equiv \omega_\beta - \omega_-$, and with first-order frequency shifts given by

$$\delta_{1-}^{(j)} \equiv G_{jj}^a - G_{jj}^n; \quad \delta_{1+}^{(j)} \equiv -G_{jj}^n. \quad (\text{E7})$$

Note that in writing down the Hamiltonian (E5), we have neglected a constant term $-\sum_j \delta_{1+}^{(j)}(\mathbf{r}_j)$ that we must include when computing the induced force. The corresponding dissi-

pator reads

$$\begin{aligned} \mathcal{D}_1[\hat{\rho}] = & \sum_j \kappa_a^{(j)} \mathcal{L}_{\hat{\sigma}_{-0}^{(j)} \hat{\sigma}_{0-}^{(j)}}[\hat{\rho}] + \kappa_d^{(j)} \mathcal{L}_{\hat{\sigma}_{0-}^{(j)} \hat{\sigma}_{-0}^{(j)}}[\hat{\rho}] \\ & + \sum_{j \neq j'} \Gamma_{jj'}^{(n)} \mathcal{L}_{\hat{\sigma}_{-0}^{(j')} \hat{\sigma}_{0-}^{(j)}}[\hat{\rho}] + \Gamma_{jj'}^{(a)} \mathcal{L}_{\hat{\sigma}_{0-}^{(j')} \hat{\sigma}_{-0}^{(j)}}[\hat{\rho}] \end{aligned} \quad (\text{E8})$$

with

$$\begin{bmatrix} \Gamma_{jj'}^{(a)} \\ \Gamma_{jj'}^{(n)} \end{bmatrix} = \sum_\beta \frac{\gamma_\beta}{\Delta_\beta^2 + (\gamma_\beta/2)^2} \begin{bmatrix} (1 + \bar{n}_\beta) g_{j\beta} g_{j'\beta}^* \\ \bar{n}_\beta g_{j\beta}^* g_{j'\beta} \end{bmatrix}, \quad (\text{E9})$$

and decay and absorption rates given by

$$\kappa_a^{(j)} \equiv \Gamma_{jj}^{(n)}; \quad \kappa_d^{(j)} \equiv \Gamma_{jj}^{(a)}. \quad (\text{E10})$$

Regarding the contribution \hat{V}_2 , one can largely simplify it by noting that, in the representation Eq. (D5), the bath operator

$$\hat{B}_\alpha(t) \rightarrow \hat{B}_j(t) \equiv \frac{1}{2} \sum_{\beta\beta'} \tilde{g}_{j\beta\beta'} \hat{s}_\beta^\dagger(t) \hat{s}_{\beta'}(t) \quad (\text{E11})$$

is Hermitian, and hence all the one-sided power spectral densities in Eq. (D11) are equal. Their value at zero frequency reads

$$\bar{S}_{jj'}(0) = \frac{-1}{8\pi} \sum_{\beta\beta'} \frac{\bar{n}_\beta(1 + \bar{n}_{\beta'}) \tilde{g}_{j\beta\beta'} \tilde{g}_{j'\beta'\beta}}{i(\omega_\beta - \omega_{\beta'}) - (\gamma_\beta + \gamma_{\beta'})/2}. \quad (\text{E12})$$

Furthermore, the system operator $\hat{O}_{s,\alpha}$ is also Hermitian, allowing us to simplify the final master equation. Specifically, the coherent contribution reads

$$\frac{\hat{H}_{\text{eff},2}}{\hbar} = \sum_j \sum_{\alpha=\pm} \delta_{2\alpha}^{(j)} \hat{\sigma}_{\alpha\alpha}^{(j)} + \sum_{j \neq j'} \frac{G_{2,jj'}}{\hbar^2} \hat{S}_z^{(j)} \hat{S}_z^{(j')}, \quad (\text{E13})$$

with

$$G_{2,jj'} \equiv -2\pi i [\bar{S}_{jj'}(0) - \bar{S}_{j'j}^*(0)] \quad (\text{E14})$$

and second-order frequency shifts given by

$$\delta_{2\pm}^{(j)} \equiv G_{2,jj} = 4\pi \text{Im}[\bar{S}_{jj}(0)]. \quad (\text{E15})$$

On the other hand, the dissipative contribution reads

$$\mathcal{D}_2[\hat{\rho}] = \sum_j \frac{\kappa_2^{(j)}}{\hbar^2} \mathcal{L}_{\hat{S}_z^{(j)} \hat{S}_z^{(j)}}[\hat{\rho}] + \sum_{j \neq j'} \frac{\Gamma_{2,jj'}}{\hbar^2} \mathcal{L}_{\hat{S}_z^{(j')} \hat{S}_z^{(j)}}[\hat{\rho}], \quad (\text{E16})$$

with the rates

$$\Gamma_{2,jj'} \equiv 2\pi [3\bar{S}_{jj'}(0) + 3\bar{S}_{j'j}^*(0) + \bar{S}_{j'j}(0) + \bar{S}_{jj}^*(0)], \quad (\text{E17})$$

and the additional dephasing rate

$$\kappa_2^{(j)} \equiv \Gamma_{2,jj} = 16\pi \text{Re}[\bar{S}_{jj}(0)]. \quad (\text{E18})$$

It is insightful to compute the equations of motion for the expected value of an arbitrary transition operator of a given NV center, $\langle \hat{\sigma}_{\alpha\alpha'}^{(j)} \rangle$, as given by the complete master equation Eq. (E4). For simplicity, we will assume NV centers in thermal equilibrium, i.e., $\Omega = 0$. The extension to optically pumped NV centers can be done following the derivation in

¹⁷Note that these corrections are expectedly small, because the band $n = 0$ represents only one among many contributions to the effective dynamics of the NV centers [specifically, to the rates appearing in the master Eq. (E4)]. The contributions from higher bands ($n = 1, 2, \dots$), which are significant especially at fields $H_0 \lesssim 15$ mT, are well within the validity regime of the Markov approximation.

Appendix B 2. The equations of motion for the ground state manifold can be written in compact form in the following way:

$$\begin{aligned} \frac{d}{dt} \langle \hat{\sigma}_{00}^{(j)} \rangle &= -(2\gamma_+ + \kappa_a^{(j)}) \langle \hat{\sigma}_{00}^{(j)} \rangle + \kappa_1 (1 + \bar{n}_+) \langle \hat{\sigma}_{++}^{(j)} \rangle \\ &\quad + [\kappa_1 (1 + \bar{n}_-) + \kappa_d^{(j)}] \langle \hat{\sigma}_{--}^{(j)} \rangle \\ &\quad - \sum_{k \neq j} [\Gamma_{d,jk} \langle \hat{\sigma}_{0-}^{(k)} \hat{\sigma}_{-0}^{(j)} \rangle + \text{c.c.}], \end{aligned} \quad (\text{E19})$$

$$\frac{d}{dt} \langle \hat{\sigma}_{++}^{(j)} \rangle = \kappa_1 \bar{n}_+ \langle \hat{\sigma}_{00}^{(j)} \rangle - \kappa_1 (1 + \bar{n}_+) \langle \hat{\sigma}_{++}^{(j)} \rangle, \quad (\text{E20})$$

$$\begin{aligned} \frac{d}{dt} \langle \hat{\sigma}_{--}^{(j)} \rangle &= [\kappa_1 \bar{n}_- + \kappa_a^{(j)}] \langle \hat{\sigma}_{00}^{(j)} \rangle - [\kappa_1 (1 + \bar{n}_-) \\ &\quad + \kappa_d^{(j)}] \langle \hat{\sigma}_{--}^{(j)} \rangle + \sum_{k \neq j} [\Gamma_{d,jk} \langle \hat{\sigma}_{0-}^{(k)} \hat{\sigma}_{-0}^{(j)} \rangle + \text{c.c.}], \end{aligned} \quad (\text{E21})$$

$$\begin{aligned} \frac{d}{dt} \langle \hat{\sigma}_{0+}^{(j)} \rangle &= \left[-i(\omega_+ + \delta_+^{(j)}) - \frac{\kappa_2 + \kappa_2^{(j)}}{2} \right. \\ &\quad \left. - \frac{\kappa_1 + 3\gamma_+ - \gamma_- + \kappa_d^{(j)}}{2} \right] \langle \hat{\sigma}_{0+}^{(j)} \rangle \\ &\quad - \sum_{k \neq j} \frac{\Gamma_{z,jk}}{\hbar} \langle \hat{\sigma}_{0+}^{(j)} \hat{S}_z^{(k)} \rangle - \sum_{k \neq j} \Gamma_{d,jk} \langle \hat{\sigma}_{-+}^{(j)} \hat{\sigma}_{0-}^{(k)} \rangle, \end{aligned} \quad (\text{E22})$$

$$\begin{aligned} \frac{d}{dt} \langle \hat{\sigma}_{0-}^{(j)} \rangle &= \left[-i(\omega_- + \delta_-^{(j)}) - \frac{\kappa_2 + \kappa_2^{(j)}}{2} \right. \\ &\quad \left. - \frac{\kappa_1 + 3\gamma_+ + \gamma_- + \kappa_d^{(j)} + \kappa_a^{(j)}}{2} \right] \langle \hat{\sigma}_{0-}^{(j)} \rangle \\ &\quad + \sum_{k \neq j} \frac{\Gamma_{z,jk}}{\hbar} \langle \hat{\sigma}_{0-}^{(j)} \hat{S}_z^{(k)} \rangle \\ &\quad - \sum_{k \neq j} \Gamma_{d,jk} \langle (\hat{\sigma}_{--}^{(j)} - \hat{\sigma}_{00}^{(j)}) \hat{\sigma}_{0-}^{(k)} \rangle, \end{aligned} \quad (\text{E23})$$

$$\begin{aligned} \frac{d}{dt} \langle \hat{\sigma}_{+-}^{(j)} \rangle &= \left[i(\omega_+ + \delta_+^{(j)} - \omega_- - \delta_-^{(j)}) \right. \\ &\quad \left. - 2(\kappa_2 + \kappa_2^{(j)}) - \frac{2\kappa_1 + 2\gamma_+ + \kappa_d^{(j)}}{2} \right] \langle \hat{\sigma}_{+-}^{(j)} \rangle \\ &\quad + 2 \sum_{k \neq j} \frac{\Gamma_{z,jk}}{\hbar} \langle \hat{\sigma}_{+-}^{(j)} \hat{S}_z^{(k)} \rangle + \sum_{k \neq j} \Gamma_{d,jk} \langle \hat{\sigma}_{+0}^{(j)} \hat{\sigma}_{0-}^{(k)} \rangle, \end{aligned} \quad (\text{E24})$$

where γ_+ and γ_- are defined in Eq. (B6). We define the total frequency shifts

$$\delta_{\pm}^{(j)} \equiv \delta_{1\pm}^{(j)} + \delta_{2\pm}^{(j)} \quad (\text{E25})$$

and the total coupling rates between NV centers,

$$\Gamma_{d,jk} \equiv \frac{\Gamma_{jk}^{(n)} - \Gamma_{kj}^{(a)}}{2} - i(G_{jk}^n + G_{kj}^a), \quad (\text{E26})$$

$$\Gamma_{z,jk} \equiv \frac{\Gamma_{2,jk} - \Gamma_{2,kj}}{2} + iG_{2,jk} + iG_{2,kj}. \quad (\text{E27})$$

In the above equations of motion, it is evident that all the interaction terms between different NV centers, both dissipative

and coherent, combine into the single interaction rates $\Gamma_{d,jk}$ and $\Gamma_{z,jk}$, which are the relevant quantities describing the spin wave induced interaction. Let us analyze each of the spin wave induced dynamics separately.

2. Spin wave induced modification of T_1 and T_2^* for a single NV center in thermal equilibrium

Here we focus on the modification of the decay and dephasing rates, which are defined in thermal equilibrium (i.e., no optical pumping). We thus consider a single NV center by making $\Gamma_{d,jk} = \Gamma_{z,jk} = 0$ in the equations of motion Eqs. (E19)–(E24), and take $\Omega = 0$. The resulting equations of motion have a similar form as for the NV center in the absence of spin waves, Eqs. (B4), (B10), and (B11), allowing us to define the new decay and dephasing times. Let us first discuss the dynamics of the occupations of the NV levels, namely, $\langle \hat{\sigma}_{\alpha\alpha} \rangle(t)$, which are independent on the dephasing rates κ_2 and κ_2' . The dynamics of these occupations are given by

$$\begin{aligned} \frac{d}{dt} \begin{bmatrix} \langle \hat{\sigma}_{00} \rangle \\ \langle \hat{S}_z / \hbar \rangle \end{bmatrix} &= \begin{bmatrix} \kappa_1 + \gamma_+ + (\Gamma_+ + \Gamma_-)/2 \\ \gamma_- + (\Gamma_+ + \Gamma_-)/2 \end{bmatrix} \\ &\quad - (\bar{M}_0 + \bar{M}') \begin{bmatrix} \langle \hat{\sigma}_{00} \rangle \\ \langle \hat{S}_z / \hbar \rangle \end{bmatrix}, \end{aligned} \quad (\text{E28})$$

with

$$\bar{M}' = \frac{1}{2} \begin{bmatrix} 3\Gamma_+ - \Gamma_- & \Gamma_+ + \Gamma_- \\ 3\Gamma_+ - \Gamma_- & \Gamma_+ + \Gamma_- \end{bmatrix}. \quad (\text{E29})$$

Here, we have defined the sum and difference of the spin wave induced decay rates as

$$\begin{aligned} \Gamma_{\pm} &\equiv \frac{\kappa_d \pm \kappa_a}{2} = v^2 \sum_n \int d^2 \mathbf{k}_{\parallel} \frac{\omega_M}{\omega_{\beta}} \left[1 + \eta \frac{k_y}{k_{\parallel}} \right]^2 \\ &\quad \times \frac{\gamma_{\beta} |h_{\beta\eta 0}|^2 e^{-2k_{\parallel} l}}{(\omega_- - \omega_{\beta})^2 + (\gamma_{\beta}/2)^2} [1 + \bar{n}_{\beta} \pm \bar{n}_{\beta}], \end{aligned} \quad (\text{E30})$$

where the last expression has been obtained by substituting the coupling rate from Eq. (9), the zero-point magnetization from Eq. (5), the modal fields from Eq. (A61), and taking the continuum limit Eq. (A91). We have also defined the coefficient

$$v^2 \equiv \frac{\mu_0^2 |\gamma| \gamma_s^2 \hbar M_S}{16\pi^2 d}, \quad (\text{E31})$$

which has dimensions of velocity squared. Note that at not too low temperatures ($T \gtrsim 10$ K) the above decay rates fulfill $|\Gamma_+| \gg |\Gamma_-|$ due to the difference in the thermal factors appearing on each quantity.

As detailed in Appendix B 1, in the absence of spin waves, at zero applied field H_0 and for an initially polarized NV center ($\langle \hat{S}_z \rangle(t=0) = 0$), the system of equations Eq. (E28) decouples and hence all the occupations decay to their steady state value exponentially with a lifetime T_1 given by Eq. (B15). This behavior is altered in the presence of spin waves or at $H_0 \neq 0$, where the evolution of the occupations follows a double exponential decay

$$\langle \hat{\sigma}_{\alpha\alpha} \rangle(t) \sim ae^{-t/T_{1a}} + be^{-t/T_{1b}}, \quad (\text{E32})$$

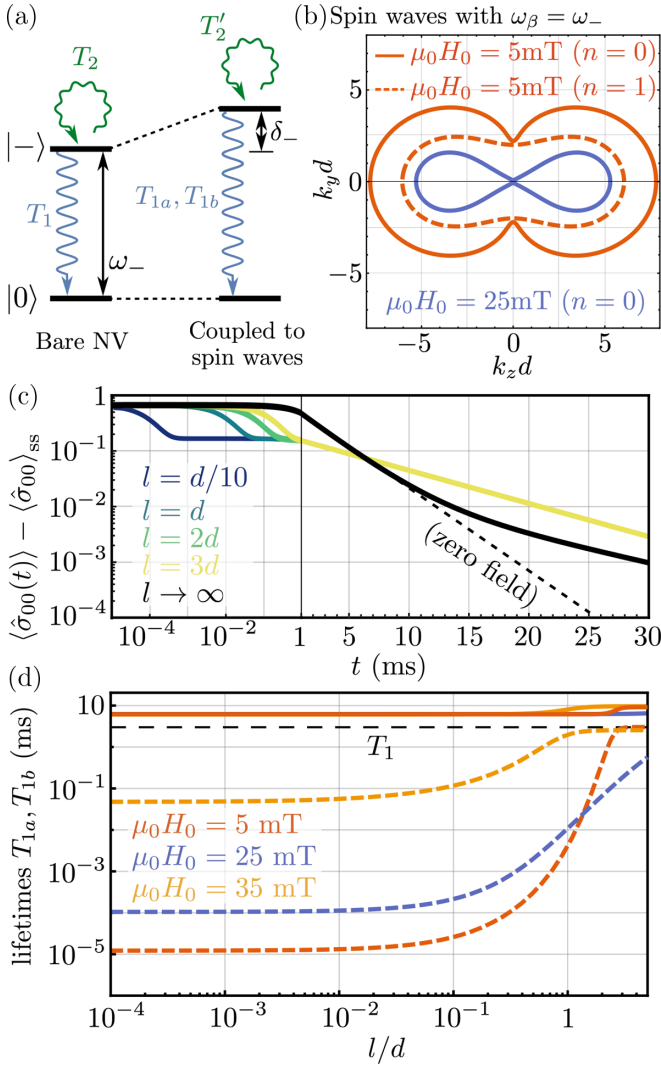


FIG. 11. (a) Spin waves cause a frequency shift δ_- of the NV transition frequency and decrease of the lifetimes T_1 and T_2^* . (b) Spin waves resonant with the $|0\rangle \leftrightarrow |- \rangle$ transition of the NV: at $\mu_0 H_0 = 5$ mT spin waves in both $n = 0$ (solid red line) and $n = 1$ bands (dashed red line) are resonant, whereas for $\mu_0 H_0 = 25$ mT (blue lines) only the $n = 0$ spin waves are, and for $\mu_0 H_0 \gtrsim 30$ mT no spin wave is resonant. (c) Evolution of the ground state occupation of the NV after initialization in the $|0\rangle$ state, for different NV-film separations and $\mu_0 H_0 = 25$ mT. The dashed line shows the single exponential decay for an isolated NV at $H_0 = 0$, which defines the timescale T_1 . (d) The two timescales describing the evolution of the NV occupations in the presence of spin waves (solid and dashed lines, respectively) as a function of NV-film distance l , for the three values of static fields H_0 considered in (b). The horizontal dashed line indicates the original T_1 . In all three panels we take $T = 300$ K and the parameters in Table I.

for any initial state [see Fig. 11(a)]. The inverse rates T_{1a}^{-1} and T_{1b}^{-1} are given by the eigenvalues of the 2×2 matrix $\bar{M}_0 + \bar{M}'$ appearing in Eq. (E28), namely,

$$\lambda_{\pm} = 2\gamma_+ + \kappa_1 + \Gamma_+ \pm [\gamma_+^2 + 3\gamma_-^2 + \Gamma_+^2 + \Gamma_+(\gamma_+ + \gamma_-) + \Gamma_-(\gamma_+ - \gamma_-)]^{1/2}. \quad (\text{E33})$$

Note that from Eq. (E30), Eq. (A65), and the even parity of ω_{β} and γ_{β} under the reflection $k_y \rightarrow -k_y$, one can easily show that the eigenvalues λ_{\pm} , and thus the modification of the occupation dynamics, are the same on both sides of the slab and depend only on the vertical separation from its surface, l . In Fig. 11(c), we show the evolution of the ground-state occupation of the NV center at $\mu_0 H_0 = 25$ mT, for an NV at different separations from the YIG film. In the absence of spin waves, i.e., at $l \rightarrow \infty$ (solid black line), the evolution of $\langle \hat{\sigma}_{00}(t) \rangle$ is very well approximated by a single exponential decay with slope T_1 , as it only deviates from the zero-field case (dashed line) at very long times where the steady state is practically reached. This justifies the use of the timescale T_1 , technically defined only at $H_0 = 0$, to describe also NV centers in the presence of weak applied fields. However, when the NV center is placed close to the YIG film, the deviation from an exponential decay becomes very relevant. The evolution of $\langle \hat{\sigma}_{00} \rangle$ is in this case characterized by a fast decay to a metastable value $\langle \hat{\sigma}_{00} \rangle \approx \langle \hat{\sigma}_{00} \rangle_{ss} + 0.2$, followed by a slow decay toward the steady state. Since both these processes are relevant, one must consider the two relaxation times T_{1a} and T_{1b} separately.

The two relaxation times T_{1a} and T_{1b} are displayed in Fig. 11(d), in solid and dashed lines, for three different values of the applied field H_0 and for the parameters in Table I. The most striking effect is given by the lowest lifetime (dashed lines), which is orders of magnitude smaller than the original lifetime T_1 . This strong modification, known as Purcell enhancement in nanophotonics [134], originates from the film-induced modification of the electromagnetic density of states. Indeed, the dashed lines in Fig. 11(d) display the typical behavior observed for Purcell-enhanced lifetimes associated to exponentially localized surface modes such as thin-film [135] or graphene [136] surface plasmons. For small separations, the Markov approximation remains valid for $\mu_0 H_0 \gtrsim 20$ mT as $\gamma_{\beta} T_{1a,b} \gtrsim 1$. The lowest lifetime in the figure (dashed lines) tends to the original one, T_1 , as $l \rightarrow \infty$, i.e., in the absence of spin waves. This motivates us to define the spin-wave-reduced lifetime of the transition $|0\rangle \leftrightarrow |- \rangle$ as

$$T_1' \equiv \min(T_{1a}, T_{1b}) = \max\left(\frac{1}{\lambda_+}, \frac{1}{\lambda_-}\right). \quad (\text{E34})$$

This quantity, more details of which are given below, is the modified lifetime used in the main text.

The dependence of the dashed lines in Fig. 11(d) on the applied field H_0 can be understood from Fig. 11(b), which indicates the resonant spin waves (i.e., the spin waves fulfilling the resonance condition $\omega_{\beta} = \omega_-$) for each value of H_0 considered in Fig. 11(d): on the one hand, at high fields, $\mu_0 H_0 \gtrsim 30$ mT, no spin waves are resonant with the NV transition and the effect of the spin waves is strongly suppressed, resulting in a lifetime closer to T_1 . On the other hand, at low fields $\mu_0 H_0 \gtrsim 5$ mT, the lifetime modification is maximized as many spin wave modes fulfill the resonance condition $\omega_{\beta} = \omega_-$. Finally, the intermediate field case $\mu_0 H_0 \gtrsim 25$ mT is characterized by an intermediate lifetime enhancement in between the above two extreme cases. In this situation, moreover, the lifetime remains significantly different from the value T_1 even at large distances $l \sim 5d$, as the resonance condition $\omega_{\beta} = \omega_-$ is fulfilled also for spin waves of very low wave numbers

[see blue line in Fig. 11(b)]. Note finally that the lifetimes on Fig. 11(d) remain significantly different from T_1 even at easily achievable NV-film distances $l \approx d$, suggesting that the modified dynamics exemplified in Fig. 11(c) could be measured through the fluorescence of the NV center [25–29,72]. Indeed, the spin wave induced modification of the lifetime T_1 has already been proposed as a potential explanation for the observed modifications in the optically detected magnetic resonance spectrum of NV centers close to magnetic structures [27–29]. Conversely, the strong dependence of the lifetimes on the NV separation from the film, l , could be exploited to optically measure such separation.

Let us finally focus on the lifetime of the coherences, particularly of the coherences $\langle \hat{\sigma}_{0\pm} \rangle$, whose lifetime at $H_0 = 0$ defines the coherence lifetime T_2^* . In the presence of spin waves, the definition of a single coherence time is not possible, since the lifetime of each of these coherences becomes different, see Eqs. (E22) and (E23). Specifically, from these equations, we can extract the lifetimes of these two coherences as

$$\begin{bmatrix} \tau_{0+}^{-1} \\ \tau_{0-}^{-1} \end{bmatrix} = \frac{\kappa_2 + \kappa'_2 + \kappa_1 + 3\gamma_+}{2} - \frac{1}{2} \begin{bmatrix} \gamma_- - \Gamma_+ + \Gamma_- \\ -\gamma_- - 2\Gamma_+ \end{bmatrix}. \quad (\text{E35})$$

The calculation of these rates requires determining the rate κ'_2 [Eq. (E18)] which, by following similar steps as above, can be cast in integral form as

$$\begin{aligned} \kappa'_2 &= v^4 \sum_{nn'} \int d^2\mathbf{k}_{\parallel} \int d^2\mathbf{k}'_{\parallel} [1 - e^{-d|\mathbf{k}_{\parallel} - \mathbf{k}'_{\parallel}|}]^2 \\ &\times \frac{\bar{n}_{\beta}(\bar{n}_{\beta'} + 1)}{\omega_{\beta}\omega_{\beta'}} \frac{\gamma_{\beta} + \gamma_{\beta'}}{(\omega_{\beta} - \omega_{\beta'})^2 + [(\gamma_{\beta} + \gamma_{\beta'})/2]^2} \\ &\times (X_{0\beta\beta'}^-)^2 \sum_{\xi=\pm} \frac{(k_z - k'_z)^4 d^4 e^{-2l|\mathbf{k}_{\parallel} - \mathbf{k}'_{\parallel}|}}{\pi^2(n' + \xi n)^2 + (|\mathbf{k}_{\parallel} - \mathbf{k}'_{\parallel}|d)^2}. \quad (\text{E36}) \end{aligned}$$

From the above expression it is evident that κ'_2 , and therefore the spin wave induced dephasing, is the same on both sides of the slab as it does not depend on η . Furthermore, κ'_2 only depends on the vertical separation from its surface, l .

The lifetimes of the coherences $\tau_{0\pm}$, given by Eq. (E35), are displayed in Fig. 12 (green and purple lines, respectively) as a function of the distance from the YIG surface. In order to isolate the effect of the additional decay rates κ_a and κ_d from that of the additional dephasing rate κ'_2 , in Fig. 12, we plot these lifetimes calculated only from the first-order contribution \hat{V}_1 , i.e., for $\kappa'_2 = 0$ (dashed lines) and calculated up to second order, i.e., including κ'_2 (solid lines). As evidenced by the figure, the effect of κ'_2 is negligible for $l \gtrsim 10^{-2}d$, where the deviation of the coherence lifetimes from their original value T_2^* is dominated by the decay rates κ_a and κ_d , i.e., by T'_1 . In this regime the coherence lifetimes are Purcell-reduced in a similar way as the occupation lifetimes in Fig. 11(d). The lifetime of the coherence $\langle \hat{\sigma}_{0+} \rangle$ is not modified as strongly as the lifetime of $\langle \hat{\sigma}_{0-} \rangle$ as the corresponding NV transition $|0\rangle \leftrightarrow |+\rangle$ is uncoupled from the spin wave modes. As a result there is a strong difference between these two lifetimes, that can differ by up to a factor 2 at low separations $l \sim 10^{-2}d$. At even lower separations, $l/d \lesssim 10^{-2}$, the effect of the addi-

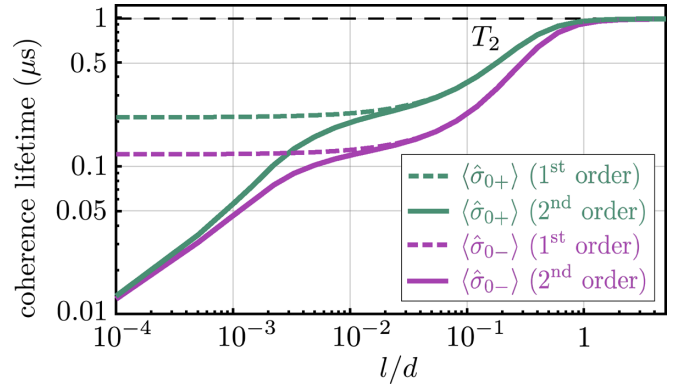


FIG. 12. Lifetimes of the two NV coherences $\langle \hat{\sigma}_{0\pm} \rangle$, Eq. (E35), at $\mu_0 H_0 = 20$ mT as a function of NV-film distance l . Dashed lines indicate the result including only the first-order contribution to the potential \hat{V}_1 in Eq. (E1), whereas the solid lines show the full result including the second-order term \hat{V}_2 . In all three panels, we take $T = 300$ K and the parameters in Table I.

tional dephasing κ'_2 becomes relevant and eventually dominant over the first-order contribution. In the low separation limit $l \ll d$, the two lifetimes become equal and much smaller than the original T_2^* of the NV center. This large increase on the dephasing rate suggests that placing the NV centers as close as possible to the YIG film is not always advisable, as the corresponding rise of the NV-spin wave coupling rate could be overcome by the unavoidable increase in decoherence. Finally, note that both the stark difference between the two lifetimes at $l \approx 10^{-2}d$ and their further decrease at $l \lesssim 10^{-2}d$ are strong effects as compared to the original decoherence time T_2^* , and could in principle be resolved by spin echo experiments [28,72,74,75]. Such experiments, combined with independent measurements of the occupation dynamics displayed in Fig. 11(c), could provide valuable information of the spin wave structure of the film.

3. Frequency shift and spin wave induced force for a single NV centre

Let us now focus on the frequency shift experienced by the two transitions of a single NV center. According to Eq. (E25), the total frequency shift experienced by the transitions of a single NV reads

$$\delta_{\pm} = \delta_{1,\pm} + \delta_{2,\pm}. \quad (\text{E37})$$

The two contributions stem from the first- and second-order interaction potentials \hat{V}_1 and \hat{V}_2 , respectively. The expression for the former, given by Eqs. (E6), reads

$$\begin{bmatrix} \delta_{1,-} \\ \delta_{1,+} \end{bmatrix} = \sum_{\beta} \frac{-\Delta_{\beta}}{\Delta_{\beta}^2 + (\gamma_{\beta}/2)^2} |g_{j\beta}|^2 \begin{bmatrix} 1 + 2\bar{n}_{\beta} \\ \bar{n}_{\beta} \end{bmatrix}. \quad (\text{E38})$$

Regarding the second-order contribution, we obtain it from combining Eqs. (E12), (E14), and (E15),

$$\begin{aligned} \delta_{2,\pm} &= \frac{1}{2} \sum_{\beta\beta'} \bar{n}_{\beta}(1 + \bar{n}_{\beta'}) |\tilde{g}_{j\beta\beta'}|^2 \\ &\times \frac{(\omega_{\beta} - \omega_{\beta'})}{(\omega_{\beta} - \omega_{\beta'})^2 + [(\gamma_{\beta} + \gamma_{\beta'})/2]^2}. \quad (\text{E39}) \end{aligned}$$

By writing the above second-order contribution in integral form as done in Eq. (E36) and making use of parity arguments it can be shown that the term proportional to $\bar{n}_\beta \bar{n}_{\beta'}$ is exactly zero. Furthermore, the same parity properties allow us to cast the second-order contribution as

$$\delta_{2,\pm} = \frac{1}{4} \sum_{\beta\beta'} (\bar{n}_\beta - \bar{n}_{\beta'}) |\tilde{g}_{j\beta\beta'}|^2 \times \frac{(\omega_\beta - \omega_{\beta'})}{(\omega_\beta - \omega_{\beta'})^2 + [(\gamma_\beta + \gamma_{\beta'})/2]^2}. \quad (\text{E40})$$

The above expression is, in general, much smaller than the first-order contributions Eq. (E38) for two reasons: first, the function in the second line is non-negligible only in a narrow region of frequency space, namely, in the region $\omega_\beta - \gamma_\beta \lesssim \omega_{\beta'} \lesssim \omega_\beta + \gamma_\beta$. In these regions, however, the thermal factors fulfill $\bar{n}_\beta \approx \bar{n}_{\beta'}$ as $\gamma_\beta \sim \text{MHz}$ (see Fig. 7). Second, even in these regions the coupling rates $|\tilde{g}_{j\beta\beta'}|$ are usually much smaller than the first-order rates $|g_{j\beta}|$ since they stem from a second-order correction to the interaction potential. These arguments allow us to safely neglect this shift, i.e.,

$$\delta_{2,\pm} \ll \delta_{1,\pm} \rightarrow \delta_\pm \approx \delta_{1,\pm}. \quad (\text{E41})$$

The frequency shifts of the two NV transitions can thus be written in integral form as

$$\begin{bmatrix} \delta_- \\ \delta_+ \end{bmatrix} \approx -v^2 \sum_n \int d^2\mathbf{k}_\parallel \frac{\omega_M}{\omega_\beta} \frac{\Delta_\beta}{\Delta_\beta^2 + (\gamma_\beta/2)^2} \times |h_{\beta\eta 0}|^2 e^{-2k_\parallel l} \left(1 + \eta \frac{k_y}{k_\parallel}\right)^2 \begin{bmatrix} 2\bar{n}_\beta + 1 \\ \bar{n}_\beta \end{bmatrix}. \quad (\text{E42})$$

From the above expression, it is evident that $|\delta_-| \geq 2|\delta_+|$. Specifically, in the low- and high-temperature limits, valid respectively at cryogenic and room temperature, we find

$$\delta_+ \rightarrow \begin{cases} 0 & \text{for } k_B T \ll \hbar\omega_M \\ \delta_-/2 & \text{for } k_B T \gg \hbar\omega_M \end{cases}. \quad (\text{E43})$$

The above relations allow us to focus on the more relevant frequency shift, namely, that of the coupled transition $|0\rangle \leftrightarrow |- \rangle$.

The frequency shift δ_- is displayed in Figs. 13(a) and 13(b) as a function of vertical separation l/d , for three representative values of the applied magnetic field and at room (a) and cryogenic (b) temperatures. Regardless of the applied field H_0 , the frequency shift becomes negligible at sufficiently large distances $l \sim d$, as the amplitude of the exponentially localized $[\exp(-k_\parallel l)]$ spin waves vanishes. The different behavior of the frequency shift at different values of the field H_0 can be understood from Eq. (E42) and the resonance iso-lines in panel Fig. 11(b). Two limiting cases can be identified: first, the high-field case $\mu_0 H_0 \gtrsim 30 \text{ mT}$ [yellow lines in Figs. 13(a) and 13(b)] where no spin wave is resonant with the NV transition [hence no curve corresponding to these fields is displayed in Fig. 11(b)]. Specifically, as evidenced also by Fig. 10(a), in this case all magnons fulfill $\omega_\beta > \omega_-$, resulting in a negative frequency shift for all values of the separation l . Second, the weak field case exemplified by $\mu_0 H_0 = 5 \text{ mT}$ [red lines in Figs. 13(a) and 13(b)], where spin waves in both $n = 0$ and $n = 1$ bands are resonant with the transition $|0\rangle \leftrightarrow |- \rangle$. The phenomenology in this case depends critically on the distance

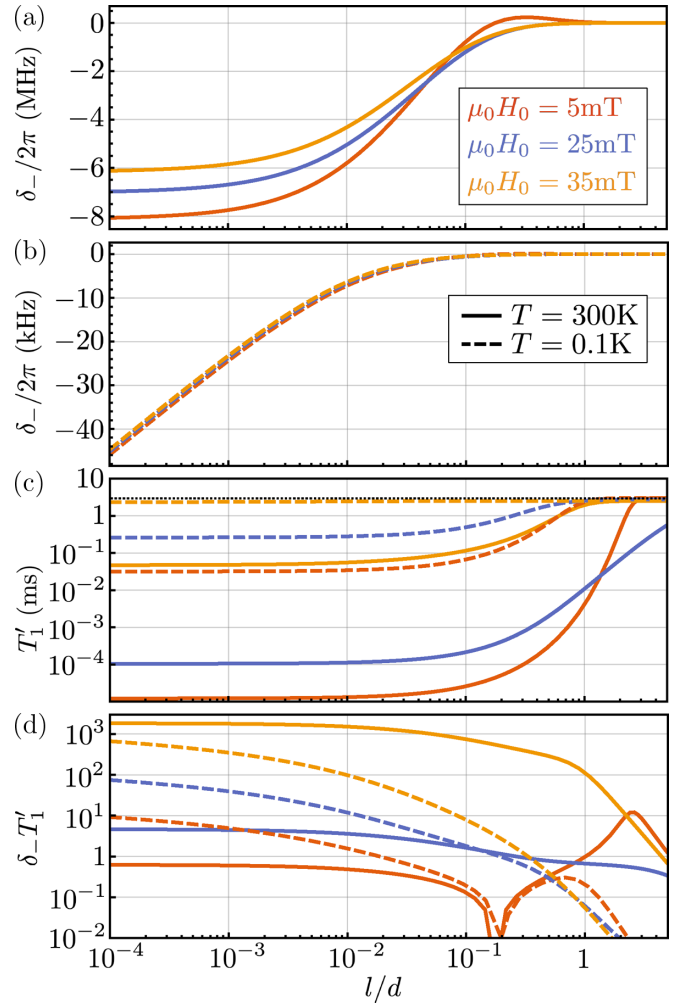


FIG. 13. [(a) and (b)] Frequency shift δ_- at room (a) and cryogenic (b) temperatures as a function of the distance between the NV center and the YIG film, for three values of the applied field H_0 . [(c) and (d)] Lifetime of the $|0\rangle \leftrightarrow |- \rangle$ transition, T_1' , and product $\delta_- T_1'$, respectively, for the same magnetic fields as in (a) and (b) and for room (solid) and cryogenic (dashed) temperatures. The black dotted line in (c) indicates the original NV lifetime in the absence of spin waves, T_1 . The yellow solid and dashed lines in (d) correspond to the red and blue curves in Fig. 4(b), respectively. In all panels, we choose the parameters as in Table I.

to the film, l : specifically, for large l only the spin waves with a very low wave number contribute significantly due to the exponential decay of the coupling rate $g_\beta \propto \exp(-k_\parallel l)$. Since all these spin wave modes fulfill $\omega_\beta < \omega_-$ the frequency shift becomes positive. On the other hand, for sufficiently small l the spin waves with higher wave number, namely, those outside the curves in Fig. 11(b), start to contribute with a negative shift as they fulfill $\omega_\beta > \omega_-$. For sufficiently short distances l , the negative contribution overcomes the positive one and the frequency shift turns negative. Finally, for intermediate values of the field such as $\mu_0 H_0 = 25 \text{ mT}$ [blue lines in Figs. 13(a) and 13(b)], most of the spin wave modes fulfill $\omega_\beta > \omega_-$, even in the low-wave-number limit. As a consequence the frequency shift remains negative for all separations l despite the resonance condition being fulfilled by some spin

waves in the $n = 0$ band. All these behaviors are similar for room and cryogenic temperatures, with the room-temperature case displaying much higher shifts due to the increased field amplitude of the thermal spin waves. Finally, note that the frequency shift is measurable for all three values of the field chosen in Figs. 13(a) and 13(b), since the corresponding spin wave-reduced lifetimes T'_1 , shown in Fig. 13(c), remain high enough for the condition $|\delta_- T'_1| > 1$ to be fulfilled [see Fig. 13(d)]. This measurement becomes less challenging at room temperature where the product $|\delta_- T'_1|$ is enhanced.

We now focus on the force exerted by the spin waves on a single NV center. This force is calculated as the steady-state expected value of the gradient of the total Hamiltonian,

$$\mathbf{F} = -\langle \nabla [\hat{H}_{\text{ps}} + \hat{H}_{\text{eff},1} + \hat{H}_{\text{eff},2}] \rangle_{\text{ss}}. \quad (\text{E44})$$

As detailed above, we can neglect the second-order frequency shifts $\delta_{2,\pm}$ and write

$$\frac{\hat{H}_{\text{eff},1} + \hat{H}_{\text{eff},2}}{\hbar} \approx -\delta_+ \hat{\sigma}_{00} + (\delta_- - \delta_+) \hat{\sigma}_{--}, \quad (\text{E45})$$

where we have added the constant (but position-dependent) correction that we neglected in Eq. (E5). Using this expression in combination with Eq. (E44), one can calculate the force in a general situation. In this work, however, we focus either on the high- or on the low-temperature limit, where the expression for the force can be simplified, using the identities Eq. (E43), to

$$\mathbf{F} = -\eta \frac{\hbar}{2} \mathbf{e}_x \frac{d\delta_-(l)}{dl} \begin{cases} 2\langle \hat{\sigma}_{--} \rangle_{\text{ss}} & \text{for } k_B T \ll \hbar \omega_M \\ \langle \hat{\sigma}_{--} - \hat{\sigma}_{00} \rangle_{\text{ss}} & \text{for } k_B T \gg \hbar \omega_M \end{cases}. \quad (\text{E46})$$

The force given by Eq. (25) in the main text results from particularizing the above expression to an NV center above the YIG film ($\eta = 1$).

The force Eq. (E44) is shown in Fig. 14 for a single NV center at room temperature (a), cryogenic temperature (b) and room temperature under optical pumping at optimal pumping conditions (c). At cryogenic temperatures optical pumping does not significantly change the force as the NV center is already near its ground state. At room temperature, the forces are very small since the steady-state occupations are generally very close to their zero-field values, i.e., $\langle \hat{\sigma}_{--} \rangle_{\text{ss}} \approx \langle \hat{\sigma}_{00} \rangle_{\text{ss}} \approx 1/3$. The resulting force is thus significantly weaker than the usual Casimir-Polder force for atoms with optical transitions (for which $\langle \hat{\sigma}_{00} \rangle_{\text{ss}} \approx 1$ even at room temperature), and lies in the 10^{-23} – 10^{-21} range. This reduced Casimir-Polder force is common for magnetic dipole transitions where the transition frequencies are comparable to thermal energy scales [95]. Moreover, room temperature forces are mostly repulsive, except at very low fields $\mu_0 H_0 = 5$ mT (red curve), where the force becomes attractive for $l \gtrsim 0.3d \approx 60$ nm following the corresponding change of slope in the frequency shift [compare with Fig. 13(a)]. Repulsive Casimir-Polder forces are a common feature of magnetic dipole transitions [94,95]. Conversely, forces become attractive at cryogenic temperatures. Regarding optical pumping, it is clearly more efficient at high fields as shown by Fig. 14(c). The reason behind this is the relatively large lifetime T'_1 of the NV transition at these fields [see Fig. 13(c)], which facilitates the pumping of occupation into the ground state. Moreover, in this case the pumping intensity used for optimal pumping in the absence of

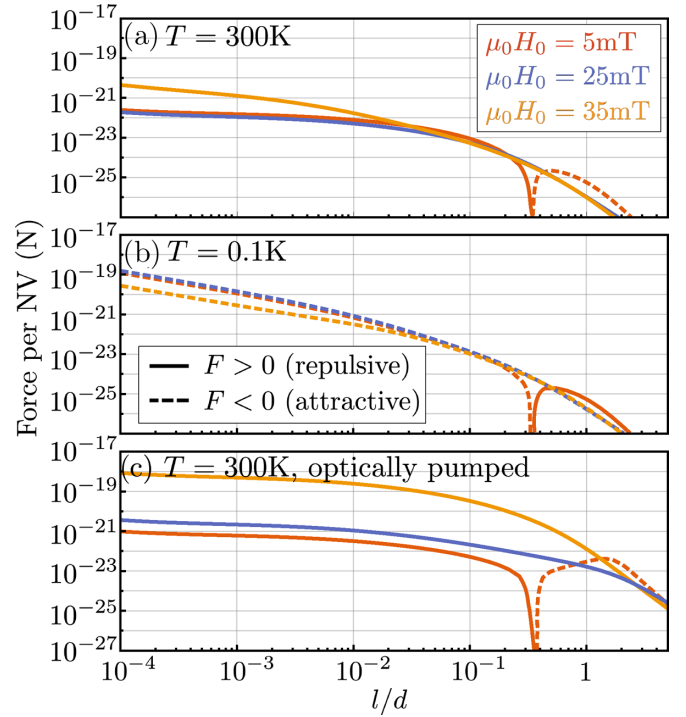


FIG. 14. Spin-wave induced force per NV center as a function of its distance to the YIG film, for three values of the applied field H_0 . (a) System at room temperature. (b) System at cryogenic temperatures. (c) System at room temperature with the NV center being optically pumped (optimal pumping conditions). The yellow curves in each panel correspond to the curves in Fig. 4(c). In all panels, we choose the parameters as in Table I.

spin waves, $I_d = 0.13$ GW m $^{-2}$, still results in very efficient initialization of the NV center, since T_1 and T'_1 are relatively similar. Conversely, at fields for which the resonance condition $\omega_\beta = \omega_-$ is fulfilled (i.e., red and blue curves Fig. 14), the very short lifetimes T'_1 make optical pumping inefficient. We emphasize that in these cases the force can still be enhanced by employing higher optical pumping intensities I_d .

4. Coupling between different NV centers

Let us finally consider the effective spin wave dynamics induced on an ensemble of NV centers. On the one hand, each NV center in the ensemble will experience the same frequency shift and the same lifetime modifications as in the single-NV case analyzed in previous sections. On the other hand, however, different NV centers will be coupled through the compound coupling rates appearing in the equations of motion, namely,

$$\Gamma_{d,jk} = \sum_{\beta} \frac{g_{j\beta}^* g_{k\beta}}{i(\omega_- - \omega_\beta) - \gamma_\beta/2} \quad (\text{E47})$$

and

$$\Gamma_{z,jk} = i \sum_{\beta\beta'} \bar{n}_\beta (\bar{n}_{\beta'} + 1) \tilde{g}_{j\beta\beta'} \tilde{g}_{k\beta'\beta} \times \frac{\omega_\beta - \omega_{\beta'}}{(\omega_\beta - \omega_{\beta'})^2 + [(\gamma_\beta - \gamma_{\beta'})/2]^2}. \quad (\text{E48})$$

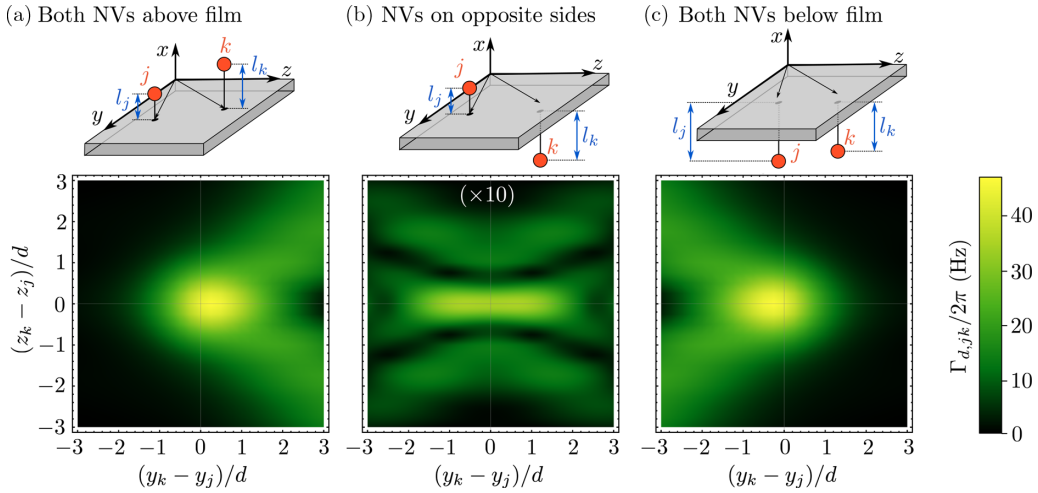


FIG. 15. Modulus of the coupling rate between NV center j and NV center k as appearing in the equation of motion for NV center j , i.e., $|\Gamma_{d,jk}|$, as a function of the relative separation in the parallel plane. The total vertical separation is $L_{kj} = l_j + l_k = d = 200$ nm, the applied field $\mu_0 H_0 = 20$ mT and the NV centers are in thermal equilibrium at room temperature. (a)–(c) show, respectively, the cases of the two NV centers lying above the film, one NV center above and a second below the film, and the two NV centers below the film.

The latter contribution, $\Gamma_{z,jk}$, can be manipulated analogously to the second-order frequency shifts $\delta_{2,\pm}$, see Eqs. (E39) and (E40), and following the same argumentation it can also be neglected. Hereafter we thus focus on the dominant coupling rate which in integral form reads

$$\Gamma_{d,jk} = v^2 \sum_n \int d^2 \mathbf{k}_{\parallel} \frac{\omega_M}{\omega_{\beta}} e^{-k_{\parallel}(l_j+l_k)} e^{i\mathbf{k}_{\parallel}(\mathbf{r}_{\parallel k}-\mathbf{r}_{\parallel j})} \left[1 + \eta_j \frac{k_y}{k_{\parallel}} \right] \times \left[1 + \eta_k \frac{k_y}{k_{\parallel}} \right] \frac{h_{\beta\eta_j} h_{\beta\eta_k} \omega}{i(\omega_{-} - \omega_{\beta}) - \gamma_{\beta}/2}. \quad (\text{E49})$$

From the above expression, we deduce that the coupling rates only depend on three variables, namely, the difference between the parallel coordinates of the two involved spins, $\mathbf{r}_{\parallel k} - \mathbf{r}_{\parallel j} \equiv y_{kj}\mathbf{e}_y + z_{kj}\mathbf{e}_z$, and the sum of their distances to the slab, $l_k + l_j \equiv L_{kj}$:

$$\Gamma_{d,jk} \equiv \Gamma_d(L_{kj}, y_{kj}, z_{kj}). \quad (\text{E50})$$

Moreover, by using the symmetries of the frequencies and loss rates under sign change of k_y and k_z , together with the symmetries Eqs. (A64) and (A65), one can show that the couplings are symmetric under permutation of the z coordinate of the two NV centers,

$$\Gamma_d(L_{kj}, y_{kj}, z_{kj}) = \Gamma_d(L_{kj}, y_{kj}, z_{jk}). \quad (\text{E51})$$

Using the same symmetry arguments, we can also derive relations between the coupling rates corresponding to different positions of the NV centers with respect to the slab, quantified by the respective indices η_j and η_k .

Specifically, (1) for NVs on different sides of the slab ($\eta_j = -\eta_k$), the rate Γ_d becomes independent on η_j and η_k , i.e., it does not depend on which side each NV center is on. Furthermore, in this case the coupling rate is symmetric under permutation of the two NV centers:

$$\Gamma_d(L_{kj}, y_{kj}, z_{kj}) = \Gamma_d(L_{kj}, y_{jk}, z_{kj}). \quad (\text{E52})$$

(2) For NVs on the same side of the slab ($\eta_j = \eta_k = \eta$), the coupling remains η -dependent but obeys the symmetry

$$\Gamma_d(L_{kj}, y_{kj}, z_{kj})|_{\eta=+} = \Gamma_d(L_{kj}, y_{jk}, z_{kj})|_{\eta=-}, \quad (\text{E53})$$

The coupling rates between two NV centers j and k , as appearing in the equations of motion for NV center j , are shown in Fig. 15 for three cases, namely, the two NV centers above the slab (a), one NV center above and a second below the slab (b), and the two NV centers below the slab (c). In general the most relevant coupling rates correspond to the two NV centers lying on the same side of the slab [(a) and (c)]. These couplings also display a strong directionality which originates from the combination of the nonreciprocity of the bath modes, i.e., the spin waves, and the polarization-selective transition of the NV center, $|0\rangle \leftrightarrow |- \rangle$. To understand this asymmetry, let us focus on the case of the two NV centers above the slab (a). The NV center j , assumed to lie at the origin of coordinates for simplicity, interacts only with spin waves polarized along \mathbf{e}_{-} , which propagate on the positive y direction [see Fig. 6(c)]. This enhances the interaction with NV centers k placed on the right half of the y - z plane ($y_k > y_j$), while suppressing the interaction with those placed on the left half ($y_k < y_j$). The emitted spin waves are resonant with the frequency of the NV transition, ω_{-} . Thus, emitted spin waves propagating near the y axis (i.e., $\phi_k \ll 1$) have much lower wave numbers than emitted spin waves propagating along a larger angle ϕ_k . Since the field amplitude, and thus the coupling rate, becomes very small also at low wave numbers, the coupling is maximized for NV centers k placed along a certain angle along the y - z plane. Note that this directional coupling mechanism is analogous to the phenomenon of chirality in quantum nanophotonics, which has attracted significant attention lately [137] due to its potential applications in quantum computing and processing, among others. Most of these applications, however, are not directly extensible to the NV-spin wave interfaces as the typical coupling strengths (several Hz in Fig. 15, potentially several kHz for NV centers near the surface of the film) are much weaker than the dissipation rates of the

NV centers. An interesting outlook of our work, and a direct application of our theoretical model, consists on exploring the enhancement of the interaction rates, for instance through coherent driving of particular spin wave modes, as well as the potential of these highly directional interactions e.g., for studying unconventional many-body physics [137].

APPENDIX F: EFFECTIVE SPIN WAVE DYNAMICS

In this section, we apply the general formalism derived in Appendix D to derive the effective dynamics of a system of spin waves induced by a bath of paramagnetic spins. As in the previous section we focus on NV centers, but our results hold for any paramagnetic spin with similar values of T_1 and T_2^* . First, we summarize the derivation of the master equation for the spin waves and provide analytical expressions for all the involved rates in Appendix F1. We then particularize these rates to a bath formed by a large number $N \gg 1$ of NV centers at random positions within the diamond slab in Appendix F2. Finally, in Appendix F3, we compute the magnetic field power spectral density in the presence of the NV centers and discuss its experimental detection.

1. Derivation of the effective dynamics

Deriving the effective spin wave dynamics requires some special attention due to the drastic difference between the slow timescale associated to the second-order contribution \hat{V}_2 , namely, T_1 (or τ_{nv} for optically pumped NV centers, see Appendix B2), and the fast timescales associated to both the first-order contribution \hat{V}_1 and the bare dissipation of the spin waves, namely, $\sim T_2^*$ and γ_β^{-1} . Note that from the equations of motion Eq. (B4) and (B10), and from the correlators of the NV center operators, Eqs. (B18), (B19), and (B23), one can show that

$$\langle \hat{\sigma}_{-0}^{(j)}(t) \hat{S}_z^{(k)}(t-s) \rangle_{\text{ss}} = \langle \hat{S}_z^{(k)}(t) \hat{\sigma}_{-0}^{(j)}(t-s) \rangle_{\text{ss}} = 0 \quad (\text{F1})$$

and

$$\langle \hat{\sigma}_{0-}^{(j)}(t) \hat{S}_z^{(k)}(t-s) \rangle_{\text{ss}} = \langle \hat{S}_z^{(k)}(t) \hat{\sigma}_{0-}^{(j)}(t-s) \rangle_{\text{ss}} = 0. \quad (\text{F2})$$

The same identities hold in the presence of optical pumping, i.e., for NV centers governed by Eqs. (B33), (B36), and (B37). As a consequence of the above expressions, the master equation does not contain crossed terms involving both \hat{V}_1 and \hat{V}_2 , which can thus be treated separately as independent reservoirs. The master equation for the magnons can thus be cast in the following form:

$$\begin{aligned} \frac{d}{dt} \hat{\rho}_{\text{sw}} = & -\frac{i}{\hbar} [\hat{H}_{\text{sw}} + \hat{H}_{\text{sw,eff},1} + \hat{H}_{\text{sw,eff},2}, \hat{\rho}_{\text{sw}}] \\ & + \mathcal{D}_{\text{sw}}[\hat{\rho}_{\text{sw}}] + \mathcal{D}_{\text{sw},1}[\hat{\rho}_{\text{sw}}] + \mathcal{D}_{\text{sw},2}[\hat{\rho}_{\text{sw}}], \end{aligned} \quad (\text{F3})$$

namely, a modification of the original magnon master equation Eq. (A72) which includes the independent contributions of \hat{V}_1 and \hat{V}_2 , i.e., the contributions originating from the effect of the NV coherences and from the NV occupations, respectively.

Let us first analyze the contribution of the coherences, namely, of the first-order term \hat{V}_1 . We include this term within the Born-Markov formalism introduced in Appendix D. Since the two-time correlators $\langle \hat{\sigma}_{0\pm}(t) \hat{\sigma}_{\mp}(t-s) \rangle_{\text{ss}}$

decay on a timescale $2/(\kappa_1 + \kappa_2 + 3\gamma_+ + \gamma_- + 2\Omega) \approx T_2^*$ [see Eqs. (B18) and (B19) or Eqs. (B36) and (B37) and note that for efficient optical pumping $\Omega \ll \kappa_2$], the Markov approximation is valid for $T_2^* \gamma_\beta \ll 1$. Regarding the spin wave dynamics, all the results in this paper focus on the $n = 0$ spin wave band, for which the Markov approximation is justified as $\gamma_\beta T_2^* \lesssim 1$ (especially at low fields $H_0 \lesssim 15$ mT). For higher order ($n \geq 1$) spin wave bands, non-Markovian corrections could be expected. Exploring the small non-Markovian corrections expectable for higher order ($n \geq 1$) bands could be an interesting outlook of our work.

Within the Markov approximation and using the correlators Eqs. (B18) and (B19) or, for optically pumped NV centers, the correlators (B36) and (B37), we can compute the contributions stemming from \hat{V}_1 . On the one hand, the coherent contribution

$$\hat{H}_{\text{sw,eff},1} = \hbar \sum_{\beta} \delta_{\beta} \hat{s}_{\beta}^{\dagger} \hat{s}_{\beta} + \hbar \sum_{\beta, \beta' \neq \beta} W_{\beta\beta'} \hat{s}_{\beta}^{\dagger} \hat{s}_{\beta'}, \quad (\text{F4})$$

which describes both a spin wave frequency shift and an effective interaction between spin waves mediated by the NV centers. Under the assumption of identical NV centers, these rates are given by

$$\begin{aligned} W_{\beta\beta'} \equiv & -\frac{G_{\beta\beta'}^2}{2} \langle \hat{\sigma}_{--} - \hat{\sigma}_{00} \rangle_{\text{ss}} \\ & \times \frac{\Delta_{\beta} + \Delta_{\beta'}}{(i\Delta_{\beta} + \kappa_T/2)(-i\Delta_{\beta'} + \kappa_T/2)} \end{aligned} \quad (\text{F5})$$

and

$$\delta_{\beta} \equiv W_{\beta\beta} = -G_{\beta\beta}^2 \langle \hat{\sigma}_{--} - \hat{\sigma}_{00} \rangle_{\text{ss}} \frac{\Delta_{\beta}}{\Delta_{\beta}^2 + (\kappa_T/2)^2}, \quad (\text{F6})$$

where we define the total coupling rates as

$$G_{\beta\beta'}^2 \equiv \sum_j g_{j\beta}^* g_{j\beta'} \quad (\text{F7})$$

and the total decay rate of the coherence $\langle \hat{\sigma}_{0-} \rangle$ as [see Eq. (B33)]

$$\kappa_T \equiv \kappa_1 + \kappa_2 + 3\gamma_+ + \gamma_- + 2\Omega. \quad (\text{F8})$$

On the other hand, the dissipator

$$\begin{aligned} \mathcal{D}_{\text{sw},1}[\hat{\rho}] = & \sum_{\beta} \Gamma_{d\beta} \mathcal{L}_{\hat{s}_{\beta} \hat{s}_{\beta}^{\dagger}}[\hat{\rho}] + \Gamma_{a\beta} \mathcal{L}_{\hat{s}_{\beta}^{\dagger} \hat{s}_{\beta}}[\hat{\rho}] \\ & + \sum_{\beta, \beta' \neq \beta} \Gamma_{\beta\beta'}^{(n)} \mathcal{L}_{\hat{s}_{\beta'} \hat{s}_{\beta}^{\dagger}}[\hat{\rho}] + \Gamma_{\beta\beta'}^{(a)} \mathcal{L}_{\hat{s}_{\beta'}^{\dagger} \hat{s}_{\beta}}[\hat{\rho}], \end{aligned} \quad (\text{F9})$$

which represents incoherent interaction between different spin wave modes at rates

$$\begin{aligned} \Gamma_{\beta\beta'}^{(n)} = & \Gamma_{\beta'\beta}^{(a)} \frac{\langle \hat{\sigma}_{00} \rangle_{\text{ss}}}{\langle \hat{\sigma}_{--} \rangle_{\text{ss}}} \\ \equiv & \langle \hat{\sigma}_{00} \rangle_{\text{ss}} G_{\beta\beta'}^2 \frac{i(\Delta_{\beta} - \Delta_{\beta'}) + \kappa_T}{(i\Delta_{\beta} + \kappa_T/2)(-i\Delta_{\beta'} + \kappa_T/2)}, \end{aligned} \quad (\text{F10})$$

as well as additional decay and absorption of each spin wave mode at rates

$$\Gamma_{d\beta} \equiv \Gamma_{\beta\beta}^{(n)}; \quad \Gamma_{a\beta} \equiv \Gamma_{\beta\beta}^{(a)}. \quad (\text{F11})$$

It is convenient to define the difference between the above ratios as

$$\Gamma_\beta \equiv \Gamma_{d\beta} - \Gamma_{a\beta} = G_{\beta\beta}^2 \langle \hat{\sigma}_{00} - \hat{\sigma}_{--} \rangle_{ss} \frac{\kappa_T}{\Delta_\beta^2 + (\kappa_T/2)^2}, \quad (\text{F12})$$

which, as we will see below, represents the increase in the decay rate of magnon mode β .

Let us now focus on the contribution from the occupations of the NV centers, namely, of the term \hat{V}_2 . For this term the Markov approximation is not applicable, as the correlators $\langle \hat{S}_z(t) \hat{S}_z(t-s) \rangle$ decay at a very slow rate $\gtrsim \tau_{nv}^{-1}$ [see Eq. (B43) and Fig. 9(c)]. However, since the spin wave observables decay at a much faster rate $\gamma_\beta \gg \tau_{nv}^{-1}$, we can compute the contribution \hat{V}_2 within the frozen bath model described in Appendix D 2. The resulting contributions to the master equation are thus

$$\mathcal{D}_{\text{sw},2}[\hat{\rho}] = 0, \quad (\text{F13})$$

$$\hat{H}_{\text{sw,eff},2} = \sum_{\beta\beta'} \Omega_{\beta\beta'} \hat{S}_\beta^\dagger \hat{S}_{\beta'}, \quad (\text{F14})$$

with a rate given, assuming identical NV centers, by

$$\Omega_{\beta\beta'} \equiv \langle \hat{S}_z / \hbar \rangle_{ss} \sum_j \tilde{g}_{j\beta\beta'}. \quad (\text{F15})$$

As expected from a bath with “frozen” fluctuations, the contribution \hat{V}_2 does not generate dissipation on the spin waves. Note that since $\tilde{g}_{j\beta\beta} = 0$ [see Eqs. (A110) and (C19)] the above contribution does not generate a frequency shift on the spin wave modes.

Having obtained the master equation for the spin waves, we can compute the equations of motion for the expected values of the spin observables in a similar way as for Eqs. (A76)–(A78). These equations of motion read

$$\frac{d}{dt} \langle \hat{S}_\beta \rangle = \left[-i(\omega_\beta + \delta_\beta) - \frac{\gamma_\beta + \Gamma_\beta}{2} \right] \langle \hat{S}_\beta \rangle - \sum_{\beta' \neq \beta} K_{\beta'\beta}^* \langle \hat{S}_{\beta'} \rangle, \quad (\text{F16})$$

$$\begin{aligned} \frac{d}{dt} \langle \hat{S}_\beta \hat{S}_{\beta'} \rangle &= \left[-i(\omega_\beta + \omega_{\beta'} + \delta_\beta + \delta_{\beta'}) \right. \\ &\quad \left. - \frac{\gamma_\beta + \gamma_{\beta'} + \Gamma_\beta + \Gamma_{\beta'}}{2} \right] \langle \hat{S}_\beta \hat{S}_{\beta'} \rangle \\ &\quad - \sum_{\beta'' \neq \beta'} K_{\beta'\beta''} \langle \hat{S}_\beta \hat{S}_{\beta''} \rangle - \sum_{\beta'' \neq \beta} K_{\beta\beta''} \langle \hat{S}_{\beta'} \hat{S}_{\beta''} \rangle, \end{aligned} \quad (\text{F17})$$

$$\begin{aligned} \frac{d}{dt} \langle \hat{S}_\beta^\dagger \hat{S}_{\beta'} \rangle &= \left[i(\omega_\beta + \delta_\beta - \omega_{\beta'} - \delta_{\beta'}) \right. \\ &\quad \left. - \frac{\gamma_\beta + \gamma_{\beta'} + \Gamma_\beta + \Gamma_{\beta'}}{2} \right] \langle \hat{S}_\beta^\dagger \hat{S}_{\beta'} \rangle(t) + \Gamma_{\beta\beta'}^{(a)} \\ &\quad + \delta_{\beta\beta'} (\gamma_\beta \bar{n}_\beta + \Gamma_{a\beta}) - \sum_{\beta'' \neq \beta'} K_{\beta'\beta''} \langle \hat{S}_\beta^\dagger \hat{S}_{\beta''} \rangle \\ &\quad - \sum_{\beta'' \neq \beta} K_{\beta\beta''}^* \langle \hat{S}_{\beta'}^\dagger \hat{S}_{\beta''} \rangle, \end{aligned} \quad (\text{F18})$$

where we have defined a compound interaction rate

$$\begin{aligned} K_{\beta\beta'} &\equiv i\Omega_{\beta\beta'} + iW_{\beta\beta'} + \frac{\Gamma_{\beta\beta'}^{(n)} - \Gamma_{\beta\beta'}^{(a)}}{2} \\ &= i\Omega_{\beta\beta'} + \frac{G_{\beta\beta'}^2}{i\Delta_\beta + \kappa_T/2} \langle \hat{\sigma}_{--} - \hat{\sigma}_{00} \rangle_{ss}. \end{aligned} \quad (\text{F19})$$

Note that the above system of equations is closed as the master equation is quadratic.

2. Master equation rates for large N and randomly distributed spins

All the rates in the master equation or in the equations of motion are given in terms of the frequencies $G_{\beta\beta'}$ and $\Omega_{\beta\beta'}$. Let us derive an expression for the former in the limit of interest, namely, a large number $N \gg 1$ of NV centers at random positions. A similar argument follows for the rate $\Omega_{\beta\beta'}$. By using the definitions of $G_{\beta\beta'}$ and the expressions for the modal fields and the couplings in Appendices A and B, we can write this rate explicitly as

$$\begin{aligned} G_{\beta\beta'}^2 &= \left(\frac{2\pi}{L} \right)^2 \frac{v^2 \omega_M}{\sqrt{\omega_\beta \omega_{\beta'}}} \left(1 + \eta \frac{k_y}{k_{\parallel}} \right) \left(1 + \eta \frac{k'_y}{k'_{\parallel}} \right) \\ &\quad \times h_{\beta\eta_0} h_{\beta'\eta_0} \sum_{j=1}^N e^{-i(\mathbf{k}_{\parallel} - \mathbf{k}'_{\parallel}) \mathbf{r}_{\parallel j}} e^{-(k_{\parallel} + k'_{\parallel}) l_j}, \end{aligned} \quad (\text{F20})$$

where the coefficient v^2 is defined in Eq. (E31), and $h_{\beta\eta_0}$ are the modal field amplitudes defined by Eq. (A63). From this explicit form it is easy to check the following symmetry between the rates corresponding to the traced out NV ensemble lying above ($\eta = 1$) or below the film ($\eta = -1$),

$$G_{(n,\mathbf{k}_{\parallel}), (n',\mathbf{k}'_{\parallel})}^2 \Big|_{\eta=-1} = (-1)^{n+n'} G_{(n,-\mathbf{k}_{\parallel}), (n',-\mathbf{k}'_{\parallel})}^2 \Big|_{\eta=1}, \quad (\text{F21})$$

from which similar relations for the frequency shift and decay rates δ_β and Γ_β follow. Moreover, $G_{\beta\beta'}$ is maximized at $n = n' = 0$. Similar properties also hold for $\Omega_{\beta\beta'}$.

The two rates $G_{\beta\beta'}^2$ and $\Omega_{\beta\beta'}$ are proportional to a function of the following general form:

$$F(\mathbf{q}, q_0) \equiv \frac{1}{L^2} \sum_{j=1}^N e^{i\mathbf{q}\mathbf{r}_{\parallel j}} e^{-q_0 l_j}. \quad (\text{F22})$$

The above quantity depends on the position of the N NV centers and thus it—and hence all the master equation rates—can be engineered by spatially patterning the distribution of NV centers or the intensity of the light used for optical pumping. As discussed in the main text [see e.g., Fig. 2(a)], here we consider an ensemble of NV centers distributed in a volume delimited by l_1 and l_2 along the x direction and infinitely extended on the directions parallel to the slab. For such configuration, we can compute the above function $F(\mathbf{q}, q_0)$ following the strategy in Ref. [138], namely, dividing the volumetric distribution of the NV centers into N_L thin layers at positions l_{0m} ($m = 1, 2, \dots, N_L$), with $l_{01} = l_1$ and $l_{0N_L} = l_2$. In the limit of large number of NV centers, $N \rightarrow \infty$, we can choose a large number of layers $N_L \gg 1$, each containing a number $N_S \rightarrow \infty$ of NV centers. By grouping the NV centers

in this way, and after multiplying and dividing by the separation between consecutive layers, namely, $\Delta l \equiv (l_2 - l_1)/N_L$, we can cast Eq. (F22) in the form

$$F(\mathbf{q}, q_0) = \varrho_{\text{ps}} \sum_{m=1}^{N_L} (\Delta l) e^{-q_0 l_{0m}} \frac{1}{N_S} \sum_{k \in \text{layer } m}^{N_S} e^{i\mathbf{q}\mathbf{r}_{\parallel k}}, \quad (\text{F23})$$

where we have defined the volumetric density of paramagnetic spins,

$$\varrho_{\text{ps}} \equiv \frac{N_S N_L}{L^2 (l_2 - l_1)}. \quad (\text{F24})$$

In the above form, the function $F(\mathbf{q}, q_0)$ can be exactly evaluated at $\mathbf{q} = 0$,

$$F(0, q_0) = \varrho_{\text{ps}} \sum_{l=l_1}^{l_2} (\Delta l) e^{-q_0 l} \approx \varrho_{\text{ps}} \int_{l_1}^{l_2} dl e^{-q_0 l}, \quad (\text{F25})$$

where in the last step, we have approximated the sum as an integral using the fact that $\Delta l \ll l_2 - l_1$ and assuming that $q_0 \Delta l \ll 1$. The above expression allows us to compute the coefficient $G_{\beta\beta}^2$, which determines the frequency shifts and decay rate modifications of the spin waves. For a slab of NV centers above the YIG film, this coefficient can be written using Eq. (F20) as

$$\begin{aligned} G_{\beta\beta}^2 &= \frac{4\pi^2 v^2}{\omega_\beta / \omega_M} \left(1 + \frac{k_y}{k_{\parallel}}\right)^2 h_{\beta+0}^2 F(0, 2k_{\parallel}) \\ &= \frac{4\pi^2 v^2 \varrho_{\text{ps}}}{\omega_\beta / \omega_M} \left(1 + \frac{k_y}{k_{\parallel}}\right)^2 h_{\beta+0}^2 \int_{l_1}^{l_2} dl e^{-2k_{\parallel} l}. \end{aligned} \quad (\text{F26})$$

Combining the above expression, for $n = 0$, with Eqs. (F6) and (F12), we obtain the definitions Eq. (20) in the main text.

We now focus on the more general coefficients $G_{\beta\beta'}^2$, whose calculation requires evaluating the function $F(\mathbf{q}, q_0)$ for $\mathbf{q} \neq 0$. This requires some further treatment as, by definition, the function as defined by Eq. (F23) depends on the values of the positions of all the NV centers. We thus assume that the NV centers are randomly distributed within each layer, and define the normalized two-dimensional structure factor as

$$s_{2D}(\mathbf{q}) \equiv \frac{1}{N_S} \sum_{m \text{ random}}^{N_S} e^{i\mathbf{q}\mathbf{r}_{\parallel m}} \quad (\text{F27})$$

to write

$$F(\mathbf{q}, q_0) = \varrho_{\text{ps}} \sum_{l=l_1}^{l_2} (\Delta l) e^{-q_0 l} s_{2D}^{(l)}(\mathbf{q}). \quad (\text{F28})$$

Here, the quantity $s_{2D}^{(l)}(\mathbf{q})$ represents, for each l , a single value sampled from the probability distribution defined by the structure factor $s_{2D}(\mathbf{q})$. In the limit $N_S \rightarrow \infty$, the real and imaginary parts of such probability distribution tend to simple Gaussian distributions with mean value 0, as can be easily derived from the one-dimensional result [139]. Thus, in this limit, the average value of the function $F(\mathbf{q}, q_0)$ vanishes

exactly

$$\lim_{N_S \rightarrow \infty} \langle F(\mathbf{q}, q_0) \rangle = \lim_{N_S \rightarrow \infty} \varrho_{\text{ps}} \sum_{l=l_1}^{l_2} (\Delta l) e^{-q_0 l} \langle s_{2D}^{(l)}(\mathbf{q}) \rangle = 0. \quad (\text{F29})$$

From the above expression, we conclude that, in the thermodynamic limit, all the coupling rates $G_{\beta\beta'}$ become, in terms of statistical averaging over many random arrangements of NV centers, negligible for $\beta \neq \beta'$, and thus can be neglected. The same argument holds for the rate $\Omega_{\beta\beta'}$ which, since $\Omega_{\beta\beta} = 0$, can be neglected for any β and β' .

3. Spin wave correlators and modification of the power spectral densities

Under the assumption $G_{\beta\beta'}, \Omega_{\beta\beta'} \approx \delta_{\beta\beta'}$ justified above, the correlators of spin wave operators can be obtained from Eqs. (F16)–(F18) using the quantum regression formula [90]. For any operator \hat{O} and for $s > 0$, they read

$$\begin{aligned} \langle \hat{s}_\beta(t+s) \hat{O}(t) \rangle_{\text{ss}} &= \langle \hat{s}_\beta \hat{O} \rangle_{\text{ss}} \exp[-(i(\omega_\beta + \delta_\beta) \\ &\quad - (\gamma_\beta + \Gamma_\beta)/2)s], \end{aligned} \quad (\text{F30})$$

$$\begin{aligned} \langle \hat{s}_\beta^\dagger(t+s) \hat{O}(t) \rangle_{\text{ss}} &= \langle \hat{s}_\beta^\dagger \hat{O} \rangle_{\text{ss}} \exp[(i(\omega_\beta + \delta_\beta) \\ &\quad - (\gamma_\beta + \Gamma_\beta)/2)s]. \end{aligned} \quad (\text{F31})$$

The steady-state occupations are also derived from Eqs. (F16)–(F18) and read

$$\langle \hat{s}_\beta \rangle_{\text{ss}} = \langle \hat{s}_\beta \hat{s}_{\beta'} \rangle_{\text{ss}} = 0, \quad (\text{F32})$$

$$\langle \hat{s}_\beta^\dagger \hat{s}_{\beta'} \rangle_{\text{ss}} = \delta_{\beta\beta'} \frac{\gamma_\beta \bar{n}_\beta + \Gamma_{\alpha\beta}}{\gamma_\beta + \Gamma_\beta} \equiv \delta_{\beta\beta'} N_\beta. \quad (\text{F33})$$

By using the above results we can compute the power spectral density of the magnetic field, Eq. (A87), in an analogous way as for the uncoupled spin waves in Appendix A 6. Specifically, one can show that for the above steady-state values, Eq. (A88) holds also in the presence of NV centers. By introducing in this equation, the corresponding correlators we obtain the following generalized expression for the power spectral density:

$$\begin{aligned} S_{\mathbf{e}_j \mathbf{e}_k}(l, \omega) &= \frac{1}{2\pi} \sum_{\beta} \mathcal{M}_{0\beta}^2 h_{\beta\eta 0}^2 e^{-2k_{\parallel} l} (\gamma_\beta + \Gamma_\beta) \\ &\quad \times \left[\bar{\Lambda}_{jk}(\eta, \mathbf{k}_{\parallel}) \frac{N_\beta + 1}{(\omega - \omega_\beta - \delta_\beta)^2 + ((\gamma_\beta + \Gamma_\beta)/2)^2} \right. \\ &\quad \left. + \bar{\Lambda}_{jk}(-\eta, \mathbf{k}_{\parallel}) \frac{N_\beta}{(\omega + \omega_\beta + \delta_\beta)^2 + ((\gamma_\beta + \Gamma_\beta)/2)^2} \right], \end{aligned} \quad (\text{F34})$$

with the matrices $\bar{\Lambda}_{jk}(\eta, \mathbf{k}_{\parallel})$ defined in Eq. (A90). This expression is formally equivalent to the power spectral density in the absence of NV centers, Eq. (A89), under the substitutions $\omega_\beta \rightarrow \omega_\beta + \delta_\beta$, $\gamma_\beta \rightarrow \gamma_\beta + \Gamma_\beta$, and $\bar{n}_\beta \rightarrow N_\beta$. Hence, the above power spectral density satisfies the same symmetry properties of the power spectral density derived in the absence

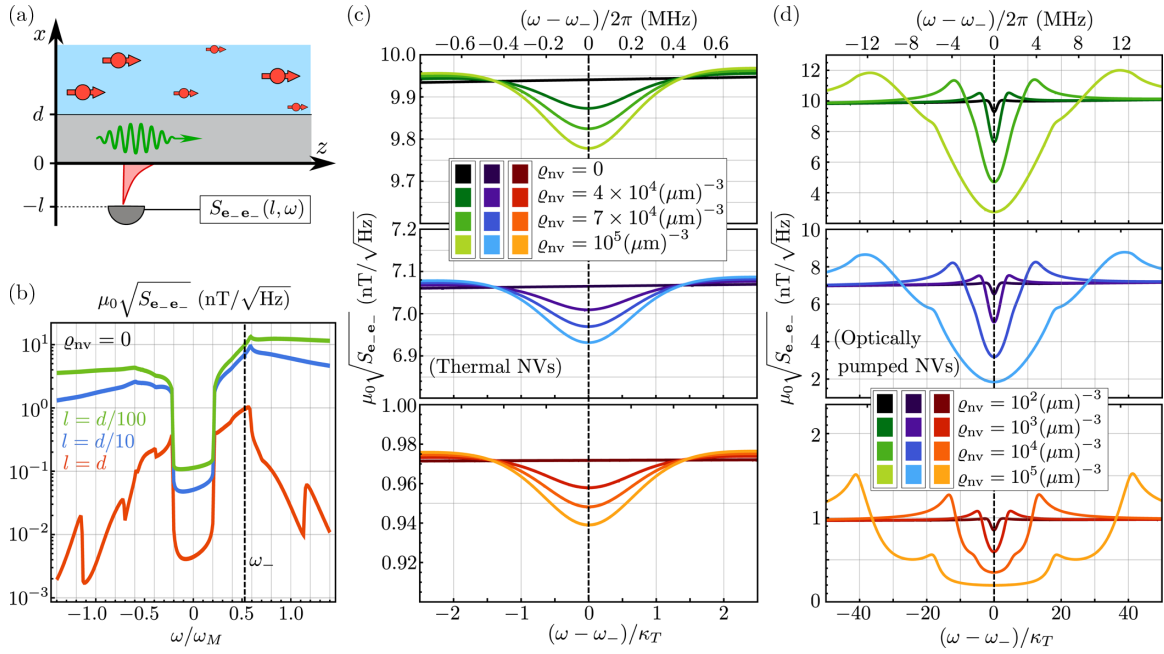


FIG. 16. (a) We consider the magnetic field power spectral density below the YIG film. (b) Power spectral density in the absence of NV centers ($\varrho_{nv} = 0$) at different separations l from the film surface. The dashed line indicates the NV transition frequency ω_- . (c) Power spectral density near $\omega = \omega_-$ for NV centers in a thermal state ($T = 300$ K). Panels with green, blue, and red-orange color schemes correspond to the same color scheme as in (a), i.e., to $l = 10^{-2}d$, $10^{-1}d$, and d , respectively. The four lines on each set correspond to different densities of NV centers. (d) Same as in (c), for optically pumped NV centers (optimal pumping conditions). In all the panels, we take $\mu_0 H_0 = 10$ mT, $l_1 = 0$, $l_2 = \infty$, $T = 300$ K, and the parameters of Table I.

of spin waves: first, the property Eq. (A93) stems from the form of $\bar{\Lambda}_{jk}(\eta, \mathbf{k}_{\parallel})$ which remains unaltered in the presence of NV centers; second, the properties Eqs. (A92) and (A96) hold due to the easily verifiable symmetries

$$G_{\beta\beta}(-k_z) = G_{\beta\beta}(k_z) \quad (\text{F35})$$

and

$$G_{\beta\beta}(k_y)|_{\eta} = G_{\beta\beta}(-k_y)|_{-\eta}, \quad (\text{F36})$$

respectively. Finally, the high-temperature parity properties Eqs. (A94) and (A95) hold in the limit $N_{\beta} \gg 1$. Since for the parameters chosen in this work $N_{\beta} \approx \bar{n}_{\beta}$ we conclude (and have numerically checked) that these parity properties also hold, at room temperature, in the presence of NV centers.

We focus on the power spectral density $S_{e_{-}e_{-}}(l, \omega) \approx S_{e_{+}e_{+}}(l, -\omega)$, for which the NV-induced modification is the most pronounced. As schematically depicted in Fig. 16(a), we consider this power spectral density in the region below the film ($\eta = -1$), where the diamond slab cannot hinder its detection. We first compute the power spectral density in the absence of NV centers in Fig. 16(b), at room temperature and at three different separations l from the YIG film. As discussed in Appendix A 6, the power spectral density is higher at shorter distances to the film l , where the thermal amplitude of the magnetic field is larger. It also becomes smoother at shorter distances as the contribution of many high-wave-number spin waves becomes practically as relevant as that of low-wave-number spin waves. In the presence of NV centers, the only appreciable change in the power spectral density occurs in a narrow frequency range centered at the NV transition frequency, ω_- , and with width of the order of

κ_T . In Fig. 16(c), we show the power spectral density within this relevant frequency range for un-pumped NV centers at room temperature thermal equilibrium. The spin waves that contribute most significantly to the power spectral density within this frequency range are those resonant to the NV transition, i.e., those fulfilling $\omega_{\beta} \approx \omega_-$. Since for these spin waves the linewidth is enhanced by a factor Γ_{β} (see discussion in Sec. III in the main text), the steady-state spin wave correlators (F30) and (F31) decay faster (i.e., the fluctuations become smaller) than in the absence of the NV centers, resulting in a decrease of the power spectral density. Note that this decrease could be interpreted as a lower effective temperature for these spin waves, as the equilibrium power spectral density is proportional to the thermal occupation factor [see, e.g., Eq. (A88)]. In this way, the action of the NV centers is equivalent to an effective frequency-resolved cooling of the spin waves. As shown by Fig. 16(c), the dip in the power spectral density becomes more pronounced near the film, where the NV centers are more strongly coupled to the spin waves. Similar phenomenology is observed for optically pumped NV centers [Fig. 16(d)]. In this case, optical pumping enhances the impact of the NV centers on the power spectral density, which now shows much deeper minima (up to $\sim 80\%$ decrease with respect to the case $\varrho_{nv} = 0$, as opposed to the $\sim 2\%$ in the unpumped case) and modifications within a much wider frequency range (about $50\kappa_T$ as opposed to $\sim \kappa_T$). Although, in both the pumped and the unpumped scenario, observing the dip in the power spectral density requires a lower magnetic noise floor and thus a higher sensitivity, this dip can still be experimentally measured. Indeed, our results in Figs. 16(c) and 16(d) for the most part remain within the sensitivity

range ($\sim 10^{-4}$ – 10^{-6} nT/ $\sqrt{\text{Hz}}$) of ultra-sensitive magnetometry techniques [127–130]. As a final remark, we note that the opposite effect, namely, the electron spin-induced *increase* of the magnetic fluctuations, could also be attained by driving the transition $|0\rangle \leftrightarrow |-\rangle$ into saturation or into population inversion. This procedure, which results in a reduction of the spin

wave linewidth, is known as “spectral hole burning” and has been successfully used to increase the quality factor of mechanical resonators whose coherence is limited by two-level system impurities [140]. Exploring the potential of spectral hole burning for spintronics is an interesting outlook to this work that can be studied with the theory we have developed.

-
- [1] Y. Tabuchi, S. Ishino, T. Ishikawa, R. Yamazaki, K. Usami, and Y. Nakamura, Hybridizing Ferromagnetic Magnons and Microwave Photons in the Quantum Limit, *Phys. Rev. Lett.* **113**, 083603 (2014).
- [2] X. Zhang, C.-L. Zou, L. Jiang, and H. X. Tang, Strongly Coupled Magnons and Cavity Microwave Photons, *Phys. Rev. Lett.* **113**, 156401 (2014).
- [3] J. A. Haigh, A. Nunnenkamp, A. J. Ramsay, and A. J. Ferguson, Triple-Resonant Brillouin Light Scattering in Magneto-Optical Cavities, *Phys. Rev. Lett.* **117**, 133602 (2016).
- [4] X. Zhang, C.-L. Zou, L. Jiang, and H. X. Tang, Cavity magnomechanics, *Sci. Adv.* **2**, e1501286 (2016).
- [5] S. Viola Kusminskiy, H. X. Tang, and F. Marquardt, Coupled spin-light dynamics in cavity optomagnonics, *Phys. Rev. A* **94**, 033821 (2016).
- [6] C. Gonzalez-Ballester, J. Gieseler, and O. Romero-Isart, Quantum Acoustomechanics with a Micromagnet, *Phys. Rev. Lett.* **124**, 093602 (2020).
- [7] H. Huebl, C. W. Zollitsch, J. Lotze, F. Hocke, M. Greifenstein, A. Marx, R. Gross, and S. T. B. Goennenwein, High Cooperativity in Coupled Microwave Resonator Ferrimagnetic Insulator Hybrids, *Phys. Rev. Lett.* **111**, 127003 (2013).
- [8] J. Li, Y. Xu, M. Aldosary, C. Tang, Z. Lin, S. Zhang, R. Lake, and J. Shi, Observation of magnon-mediated current drag in pt/yttrium iron garnet/pt(ta) trilayers, *Nat. Commun.* **7**, 10858 (2016).
- [9] Y. Tabuchi, S. Ishino, A. Noguchi, T. Ishikawa, R. Yamazaki, K. Usami, and Y. Nakamura, Coherent coupling between a ferromagnetic magnon and a superconducting qubit, *Science* **349**, 405 (2015).
- [10] D. Marcos, M. Wubs, J. M. Taylor, R. Aguado, M. D. Lukin, and A. S. Sørensen, Coupling Nitrogen-Vacancy Centers in Diamond to Superconducting Flux Qubits, *Phys. Rev. Lett.* **105**, 210501 (2010).
- [11] X. Zhu, S. Saito, A. Kemp, K. Kakuyanagi, S.-i. Karimoto, H. Nakano, W. J. Munro, Y. Tokura, M. S. Everitt, K. Nemoto, M. Kasu, N. Mizuochi, and K. Semba, Coherent coupling of a superconducting flux qubit to an electron spin ensemble in diamond, *Nature (London)* **478**, 221 (2011).
- [12] B. Lenk, H. Ulrichs, F. Garbs, and M. Münzenberg, The building blocks of magnonics, *Phys. Rep.* **507**, 107 (2011).
- [13] V. V. Kruglyak, S. O. Demokritov, and D. Grundler, Magnonics, *J. Phys. D: Appl. Phys.* **43**, 260301 (2010).
- [14] A. V. Chumak, V. I. Vasyuchka, A. A. Serga, and B. Hillebrands, Magnon spintronics, *Nat. Phys.* **11**, 453 (2015).
- [15] R. L. Stamps, S. Breitkreutz, J. Åkerman, A. V. Chumak, Y. Otani, G. E. W. Bauer, J.-U. Thiele, M. Bowen, S. A. Majetich, M. Kläui, I. L. Prejbeanu, B. Dieny, N. M. Dempsey, and B. Hillebrands, The 2014 magnetism roadmap, *J. Phys. D: Appl. Phys.* **47**, 333001 (2014).
- [16] A. V. Chumak *et al.*, Roadmap on spin wave computing, [arXiv:2111.00365](https://arxiv.org/abs/2111.00365).
- [17] A. A. Serga, A. V. Chumak, and B. Hillebrands, YIG magnonics, *J. Phys. D: Appl. Phys.* **43**, 264002 (2010).
- [18] A. V. Chumak, A. A. Serga, and B. Hillebrands, Magnon transistor for all-magnon data processing, *Nat. Commun.* **5**, 4700 (2014).
- [19] A. Gurevich and G. Melkov, *Magnetization Oscillations and Waves* (Taylor & Francis, New York, USA, 1996).
- [20] D. Stancil and A. Prabhakar, *Spin Waves: Theory and Applications* (Springer US, New York, USA, 2009).
- [21] K. Nakata, K. A. van Hoogdalem, P. Simon, and D. Loss, Josephson and persistent spin currents in bose-einstein condensates of magnons, *Phys. Rev. B* **90**, 144419 (2014).
- [22] S. Takei and Y. Tserkovnyak, Superfluid Spin Transport Through Easy-Plane Ferromagnetic Insulators, *Phys. Rev. Lett.* **112**, 227201 (2014).
- [23] D. Lachance-Quirion, Y. Tabuchi, A. Gloppe, K. Usami, and Y. Nakamura, Hybrid quantum systems based on magnonics, *Appl. Phys. Express* **12**, 070101 (2019).
- [24] J. Gieseler, A. Kabcenell, E. Rosenfeld, J. D. Schaefer, A. Safira, M. J. A. Schuetz, C. Gonzalez-Ballester, C. C. Rusconi, O. Romero-Isart, and M. D. Lukin, Single-Spin Magnetomechanics with Levitated Micromagnets, *Phys. Rev. Lett.* **124**, 163604 (2020).
- [25] I. Bertelli, J. J. Carmiggelt, T. Yu, B. G. Simon, C. C. Pothoven, G. E. Bauer, Y. M. Blanter, J. Aarts, and T. van der Sar, Magnetic resonance imaging of spin wave transport and interference in a magnetic insulator, *Sci. Adv.* **6**, eabd3556 (2020).
- [26] E. Lee-Wong, R. Xue, F. Ye, A. Kreisel, T. van der Sar, A. Yacoby, and C. R. Du, Nanoscale detection of magnon excitations with variable wavevectors through a quantum spin sensor, *Nano Lett.* **20**, 3284 (2020).
- [27] C. S. Wolfe, V. P. Bhallamudi, H. L. Wang, C. H. Du, S. Manuilov, R. M. Teeling-Smith, A. J. Berger, R. Adur, F. Y. Yang, and P. C. Hammel, Off-resonant manipulation of spins in diamond via precessing magnetization of a proximal ferromagnet, *Phys. Rev. B* **89**, 180406(R) (2014).
- [28] P. Andrich, C. F. de las Casas, X. Liu, H. L. Bretscher, J. R. Berman, F. J. Heremans, P. F. Nealey, and D. D. Awschalom, Long-range spin wave mediated control of defect qubits in nanodiamonds, *npj Quantum Inf.* **3**, 28 (2017).
- [29] M. R. Page, B. A. McCullian, C. M. Purser, J. G. Schulze, T. M. Nakatani, C. S. Wolfe, J. R. Childress, M. E. McConney,

- B. M. Howe, P. C. Hammel, and V. P. Bhallamudi, Optically detected ferromagnetic resonance in diverse ferromagnets via nitrogen vacancy centers in diamond, *J. Appl. Phys.* **126**, 124902 (2019).
- [30] D. Kikuchi, D. Prananto, K. Hayashi, A. Laraoui, N. Mizuochi, M. Hatano, E. Saitoh, Y. Kim, C. A. Meriles, and T. An, Long-distance excitation of nitrogen-vacancy centers in diamond via surface spin waves, *Appl. Phys. Express* **10**, 103004 (2017).
- [31] H. Zhang, M. J. H. Ku, F. Casola, C. H. R. Du, T. van der Sar, M. C. Onbasli, C. A. Ross, Y. Tserkovnyak, A. Yacoby, and R. L. Walsworth, Spin-torque oscillation in a magnetic insulator probed by a single-spin sensor, *Phys. Rev. B* **102**, 024404 (2020).
- [32] S. R. K. Rodriguez, J. Feist, M. A. Verschuuren, F. J. Garcia Vidal, and J. Gómez Rivas, Thermalization and Cooling of Plasmon-Exciton Polaritons: Towards Quantum Condensation, *Phys. Rev. Lett.* **111**, 166802 (2013).
- [33] G. M. Gehring, A. Schweinsberg, C. Barsi, N. Kostinski, and R. W. Boyd, Observation of backward pulse propagation through a medium with a negative group velocity, *Science* **312**, 895 (2006).
- [34] H. Kang, G. Hernandez, and Y. Zhu, Superluminal and slow light propagation in cold atoms, *Phys. Rev. A* **70**, 011801(R) (2004).
- [35] T. Peyronel, O. Firstenberg, Q.-Y. Liang, S. Hofferberth, A. V. Gorshkov, T. Pohl, M. D. Lukin, and V. Vuletić, Quantum nonlinear optics with single photons enabled by strongly interacting atoms, *Nature (London)* **488**, 57 (2012).
- [36] C. Murray and T. Pohl, Quantum and nonlinear optics in strongly interacting atomic ensembles, in *Advances In Atomic, Molecular, and Optical Physics*, edited by E. Arimondo, C. C. Lin, and S. F. Yelin (Academic Press, 2016), Vol. 65, pp. 321–372.
- [37] E. Cao, W. Lin, M. Sun, W. Liang, and Y. Song, Exciton-plasmon coupling interactions: from principle to applications, *Nanophotonics* **7**, 145 (2018).
- [38] F. Casola, T. van der Sar, and A. Yacoby, Probing condensed matter physics with magnetometry based on nitrogen-vacancy centres in diamond, *Nat. Rev. Mater.* **3**, 17088 (2018).
- [39] Y. Au, E. Ahmad, O. Dmytriiev, M. Dvornik, T. Davison, and V. V. Kruglyak, Resonant microwave-to-spin wave transducer, *Appl. Phys. Lett.* **100**, 182404 (2012).
- [40] A. Khitun and K. L. Wang, Non-volatile magnonic logic circuits engineering, *J. Appl. Phys.* **110**, 034306 (2011).
- [41] K. Vogt, F. Y. Fradin, J. E. Pearson, T. Sebastian, S. D. Bader, B. Hillebrands, A. Hoffmann, and H. Schultheiss, Realization of a spin wave multiplexer, *Nat. Commun.* **5**, 3727 (2014).
- [42] M. Fukami, D. R. Candido, D. D. Awschalom, and M. E. Flatté, Opportunities for long-range magnon-mediated entanglement of spin qubits via on- and off-resonant coupling, *PRX Quantum* **2**, 040314 (2021).
- [43] D. R. Candido, G. D. Fuchs, E. Johnston-Halperin, and M. Flatté, Predicted strong coupling of solid-state spins via a single magnon mode, *Mater. Quantum. Technol.* **1**, 011001 (2020).
- [44] M. W. Doherty, N. B. Manson, P. Delaney, F. Jelezko, J. Wrachtrup, and L. C. Hollenberg, The nitrogen-vacancy colour centre in diamond, *Phys. Rep.* **528**, 1 (2013).
- [45] I. Aharonovich, A. D. Greentree, and S. Prawer, Diamond photonics, *Nat. Photonics* **5**, 397 (2011).
- [46] M. Atatüre, D. Englund, N. Vamivakas, S.-Y. Lee, and J. Wrachtrup, Material platforms for spin-based photonic quantum technologies, *Nat. Rev. Mater.* **3**, 38 (2018).
- [47] R. Albrecht, A. Bommer, C. Deutsch, J. Reichel, and C. Becher, Coupling of a Single Nitrogen-Vacancy Center in Diamond to a Fiber-Based Microcavity, *Phys. Rev. Lett.* **110**, 243602 (2013).
- [48] J. R. Maze, P. L. Stanwix, J. S. Hodges, S. Hong, J. M. Taylor, P. Cappellaro, L. Jiang, M. V. G. Dutt, E. Togan, A. S. Zibrov, A. Yacoby, R. L. Walsworth, and M. D. Lukin, Nanoscale magnetic sensing with an individual electronic spin in diamond, *Nature (London)* **455**, 644 (2008).
- [49] F. Dolde, H. Fedder, M. W. Doherty, T. Nöbauer, F. Rempp, G. Balasubramanian, T. Wolf, F. Reinhard, L. C. L. Hollenberg, F. Jelezko, and J. Wrachtrup, Electric-field sensing using single diamond spins, *Nat. Phys.* **7**, 459 (2011).
- [50] P.-B. Li, Z.-L. Xiang, P. Rabl, and F. Nori, Hybrid Quantum Device with Nitrogen-Vacancy Centers in Diamond Coupled to Carbon Nanotubes, *Phys. Rev. Lett.* **117**, 015502 (2016).
- [51] K. V. Keesidis, S. D. Bennett, S. Portolan, M. D. Lukin, and P. Rabl, Phonon cooling and lasing with nitrogen-vacancy centers in diamond, *Phys. Rev. B* **88**, 064105 (2013).
- [52] A. Laraoui, H. Aycock-Rizzo, Y. Gao, X. Lu, E. Riedo, and C. A. Meriles, Imaging thermal conductivity with nanoscale resolution using a scanning spin probe, *Nat. Commun.* **6**, 8954 (2015).
- [53] F. Grazioso, B. R. Patton, P. Delaney, M. L. Markham, D. J. Twitchen, and J. M. Smith, Measurement of the full stress tensor in a crystal using photoluminescence from point defects: The example of nitrogen vacancy centers in diamond, *Appl. Phys. Lett.* **103**, 101905 (2013).
- [54] L. Shao, M. Zhang, M. Markham, A. M. Edmonds, and M. Lončar, Diamond Radio Receiver: Nitrogen-Vacancy Centers as Fluorescent Transducers of Microwave Signals, *Phys. Rev. Appl.* **6**, 064008 (2016).
- [55] A. Aharoni, *Introduction to the Theory of Ferromagnetism*, International Series of Monographs (Clarendon Press, 2000).
- [56] B. A. Kalinikos, Spectrum and linear excitation of spin waves in ferromagnetic films, *Sov. Phys. J.* **24**, 718 (1981).
- [57] B. A. Kalinikos and A. N. Slavin, Theory of dipole-exchange spin wave spectrum for ferromagnetic films with mixed exchange boundary conditions, *J. Phys. C: Solid State* **19**, 7013 (1986).
- [58] B. A. Kalinikos, Dipole-exchange spin wave spectrum of magnetic films, in *Linear and Nonlinear Spin Waves in Magnetic Films and Superlattices* (World Scientific Publishing, Singapore, 1994), pp. 89–156.
- [59] C. E. Patton, Magnetic excitations in solids, *Phys. Rep.* **103**, 251 (1984).
- [60] M. Kostylev, Non-reciprocity of dipole-exchange spin waves in thin ferromagnetic films, *J. Appl. Phys.* **113**, 053907 (2013).
- [61] D. Mills, Quantum theory of spin waves in finite samples, *J. Magn. Magn. Mater.* **306**, 16 (2006).
- [62] C. Gonzalez-Ballester, D. Hümmer, J. Gieseler, and O. Romero-Isart, Theory of quantum acoustomagnonics and acoustomechanics with a micromagnet, *Phys. Rev. B* **101**, 125404 (2020).

- [63] N. Bar-Gill, L. M. Pham, A. Jarmola, D. Budker, and R. L. Walsworth, Solid-state electronic spin coherence time approaching one second, *Nat. Commun.* **4**, 1743 (2013).
- [64] S. Ajisaka and Y. B. Band, Decoherence of three-level systems: Application to nitrogen-vacancy centers in diamond near a surface, *Phys. Rev. B* **94**, 134107 (2016).
- [65] Z.-Y. Wang, J.-M. Cai, A. Retzker, and M. B. Plenio, All-optical magnetic resonance of high spectral resolution using a nitrogen-vacancy spin in diamond, *New J. Phys.* **16**, 083033 (2014).
- [66] D. Hümmer, O. Romero-Isart, A. Rauschenbeutel, and P. Schneeweiss, Probing Surface-Bound Atoms with Quantum Nanophotonics, *Phys. Rev. Lett.* **126**, 163601 (2021).
- [67] S. S. Kalarickal, P. Krivosik, M. Wu, C. E. Patton, M. L. Schneider, P. Kabos, T. J. Silva, and J. P. Nibarger, Ferromagnetic resonance linewidth in metallic thin films: Comparison of measurement methods, *J. Appl. Phys.* **99**, 093909 (2006).
- [68] H.-P. Breuer and F. Petruccione, *The Theory of Open Quantum Systems* (Oxford University Press, New York, USA, 2002).
- [69] A. V. Chumak, Magnon spintronics, in *Spintronics Handbook: Spin Transport and Magnetism, Second Edition* (CRC Press, New York, 2019), Chap. 6.
- [70] D. D. Stancil, Phenomenological propagation loss theory for magnetostatic waves in thin ferrite films, *J. Appl. Phys.* **59**, 218 (1986).
- [71] J.-P. Tetienne, T. Hingant, L. Rondin, A. Cavallès, L. Mayer, G. Dantelle, T. Gacoin, J. Wrachtrup, J.-F. Roch, and V. Jacques, Spin relaxometry of single nitrogen-vacancy defects in diamond nanocrystals for magnetic noise sensing, *Phys. Rev. B* **87**, 235436 (2013).
- [72] B. A. Myers, A. Ariyaratne, and A. C. Bleszynski Jayich, Double-Quantum Spin-Relaxation Limits to Coherence of Near-Surface Nitrogen-Vacancy Centers, *Phys. Rev. Lett.* **118**, 197201 (2017).
- [73] E. D. Herbschleb, H. Kato, Y. Maruyama, T. Danjo, T. Makino, S. Yamasaki, I. Ohki, K. Hayashi, H. Morishita, M. Fujiwara, and N. Mizuochi, Ultra-long coherence times amongst room-temperature solid-state spins, *Nat. Commun.* **10**, 3766 (2019).
- [74] R. Hanson, V. V. Dobrovitski, A. E. Feiguin, O. Gywat, and D. D. Awschalom, Coherent dynamics of a single spin interacting with an adjustable spin bath, *Science* **320**, 352 (2008).
- [75] G. de Lange, Z. H. Wang, D. Ristè, V. V. Dobrovitski, and R. Hanson, Universal dynamical decoupling of a single solid-state spin from a spin bath, *Science* **330**, 60 (2010).
- [76] E. E. Kleinsasser, M. M. Stanfield, J. K. Q. Banks, Z. Zhu, W.-D. Li, V. M. Acosta, H. Watanabe, K. M. Itoh, and K.-M. C. Fu, High density nitrogen-vacancy sensing surface created via he+ ion implantation of 12c diamond, *Appl. Phys. Lett.* **108**, 202401 (2016).
- [77] E. Bauch, C. A. Hart, J. M. Schloss, M. J. Turner, J. F. Barry, P. Kehayias, S. Singh, and R. L. Walsworth, Ultralong Dephasing Times in Solid-State Spin Ensembles Via Quantum Control, *Phys. Rev. X* **8**, 031025 (2018).
- [78] L. Robledo, H. Bernien, T. van der Sar, and R. Hanson, Spin dynamics in the optical cycle of single nitrogen-vacancy centers in diamond, *New J. Phys.* **13**, 025013 (2011).
- [79] P. Wang and W. Yang, Theory of nuclear spin dephasing and relaxation by optically illuminated nitrogen-vacancy center, *New J. Phys.* **17**, 113041 (2015).
- [80] I. Meirzada, Y. Hovav, S. A. Wolf, and N. Bar-Gill, Negative charge enhancement of near-surface nitrogen vacancy centers by multicolor excitation, *Phys. Rev. B* **98**, 245411 (2018).
- [81] R. Mildren and J. Rabeau, *Optical Engineering of Diamond* (Wiley, Weinheim, Germany, 2013).
- [82] R. P. Roberts, M. L. Juan, and G. Molina-Terriza, Spin-dependent charge state interconversion of nitrogen vacancy centers in nanodiamonds, *Phys. Rev. B* **99**, 174307 (2019).
- [83] J.-P. Tetienne, L. Rondin, P. Spinicelli, M. Chipaux, T. Debuisschert, J.-F. Roch, and V. Jacques, Magnetic-field-dependent photodynamics of single NV defects in diamond: an application to qualitative all-optical magnetic imaging, *New J. Phys.* **14**, 103033 (2012).
- [84] K. Kustura, O. Romero-Isart, and C. Gonzalez-Ballester, Effective quantum dynamics induced by a driven two-level-system bath, *Phys. Rev. A* **103**, 053709 (2021).
- [85] Y. Hatano, T. Sekiguchi, T. Iwasaki, M. Hatano, and Y. Harada, Magnetic field imaging of superparamagnetic particles using high-density, perfectly oriented nv centers in diamond cvd film, *Phys. Status Solidi A* **215**, 1800254 (2018).
- [86] H. Ozawa, Y. Hatano, T. Iwasaki, Y. Harada, and M. Hatano, Formation of perfectly aligned high-density NV centers in (111) CVD-grown diamonds for magnetic field imaging of magnetic particles, *Jpn. J. Appl. Phys.* **58**, SIIB26 (2019).
- [87] V. M. Acosta, E. Bauch, M. P. Ledbetter, C. Santori, K. M. C. Fu, P. E. Barclay, R. G. Beausoleil, H. Linget, J. F. Roch, F. Treussart, S. Chemerisov, W. Gawlik, and D. Budker, Diamonds with a high density of nitrogen-vacancy centers for magnetometry applications, *Phys. Rev. B* **80**, 115202 (2009).
- [88] G. Kucsko, S. Choi, J. Choi, P. C. Maurer, H. Zhou, R. Landig, H. Sumiya, S. Onoda, J. Isoya, F. Jelezko, E. Demler, N. Y. Yao, and M. D. Lukin, Critical Thermalization of a Disordered Dipolar Spin System in Diamond, *Phys. Rev. Lett.* **121**, 023601 (2018).
- [89] M. Mojahedi, K. J. Malloy, G. V. Eleftheriades, J. Woodley, and R. Y. Chiao, Abnormal wave propagation in passive media, *IEEE J. Sel. Top. Quantum* **9**, 30 (2003).
- [90] H. Carmichael, *Statistical Methods in Quantum Optics I: Master Equations and Fokker-Planck Equations*, Theoretical and Mathematical Physics (Springer, Berlin, Heidelberg, 2013).
- [91] H. B. G. Casimir and D. Polder, The influence of retardation on the london-van der waals forces, *Phys. Rev.* **73**, 360 (1948).
- [92] S. Y. Buhmann and D.-G. Welsch, Dispersion forces in macroscopic quantum electrodynamics, *Prog. Quantum Electron.* **31**, 51 (2007).
- [93] S. Y. Buhmann and S. Scheel, Thermal Casimir Versus Casimir-Polder Forces: Equilibrium and Nonequilibrium Forces, *Phys. Rev. Lett.* **100**, 253201 (2008).
- [94] B.-S. Skagerstam, P. K. Rekdal, and A. H. Vaskinn, Theory of casimir-polder forces, *Phys. Rev. A* **80**, 022902 (2009).
- [95] H. Haakh, F. Intravaia, C. Henkel, S. Spagnolo, R. Passante, B. Power, and F. Sols, Temperature dependence of the magnetic casimir-polder interaction, *Phys. Rev. A* **80**, 062905 (2009).
- [96] A. Vinante, G. Wijts, O. Usenko, L. Schinkelshoek, and T. H. Oosterkamp, Magnetic resonance force microscopy of paramagnetic electron spins at millikelvin temperatures, *Nat. Commun.* **2**, 572 (2011).
- [97] P.-B. Li, Y.-C. Liu, S.-Y. Gao, Z.-L. Xiang, P. Rabl, Y.-F. Xiao, and F.-L. Li, Hybrid Quantum Device Based on NV Centers in

- Diamond Nanomechanical Resonators Plus Superconducting Waveguide Cavities, *Phys. Rev. Appl.* **4**, 044003 (2015).
- [98] J. S. Bunch, A. M. van der Zande, S. S. Verbridge, I. W. Frank, D. M. Tanenbaum, J. M. Parpia, H. G. Craighead, and P. L. McEuen, Electromechanical resonators from graphene sheets, *Science* **315**, 490 (2007).
- [99] P. Weber, J. Güttinger, A. Noury, J. Vergara-Cruz, and A. Bachtold, Force sensitivity of multilayer graphene optomechanical devices, *Nat. Commun.* **7**, 12496 (2016).
- [100] R. Fischer, D. P. McNally, C. Reetz, G. G. T. Assumpção, T. Knief, Y. Lin, and C. A. Regal, Spin detection with a micromechanical trampoline: towards magnetic resonance microscopy harnessing cavity optomechanics, *New J. Phys.* **21**, 043049 (2019).
- [101] M. Li, H. X. Tang, and M. L. Roukes, Ultra-sensitive nems-based cantilevers for sensing, scanned probe and very high-frequency applications, *Nat. Nanotechnol.* **2**, 114 (2007).
- [102] V. Sazonova, Y. Yaish, H. Üstünel, D. Roundy, T. A. Arias, and P. L. McEuen, A tunable carbon nanotube electromechanical oscillator, *Nature (London)* **431**, 284 (2004).
- [103] J. Moser, J. Güttinger, A. Eichler, M. J. Esplandiú, D. E. Liu, M. I. Dykman, and A. Bachtold, Ultrasensitive force detection with a nanotube mechanical resonator, *Nat. Nanotechnol.* **8**, 493 (2013).
- [104] J. M. Nichol, E. R. Hemesath, L. J. Lauhon, and R. Budakian, Nanomechanical detection of nuclear magnetic resonance using a silicon nanowire oscillator, *Phys. Rev. B* **85**, 054414 (2012).
- [105] A. Gloppe, P. Verlot, E. Dupont-Ferrier, A. Siria, P. Poncharal, G. Bachelier, P. Vincent, and O. Arcizet, Bidimensional nano-optomechanics and topological backaction in a non-conservative radiation force field, *Nat. Nanotechnol.* **9**, 920 (2014).
- [106] N. Rossi, F. R. Braakman, D. Cadeddu, D. Vasyukov, G. Tütüncüoğlu, A. Fontcuberta i Morral, and M. Poggio, Vectorial scanning force microscopy using a nanowire sensor, *Nat. Nanotechnol.* **12**, 150 (2017).
- [107] F. R. Braakman and M. Poggio, Force sensing with nanowire cantilevers, *Nanotechnology* **30**, 332001 (2019).
- [108] M. Hérítier, A. Eichler, Y. Pan, U. Grob, I. Shorubalko, M. D. Krass, Y. Tao, and C. L. Degen, Nanoladder cantilevers made from diamond and silicon, *Nano Lett.* **18**, 1814 (2018).
- [109] J.-C. Jaskula, E. Bauch, S. Arroyo-Camejo, M. D. Lukin, S. W. Hell, A. S. Trifonov, and R. L. Walsworth, Superresolution optical magnetic imaging and spectroscopy using individual electronic spins in diamond, *Opt. Express* **25**, 11048 (2017).
- [110] D. Zoepfl, M. L. Juan, C. M. F. Schneider, and G. Kirchmair, Single-Photon Cooling in Microwave Magnetomechanics, *Phys. Rev. Lett.* **125**, 023601 (2020).
- [111] P. Rabl, P. Cappellaro, M. V. Gurudev Dutt, L. Jiang, J. R. Maze, and M. D. Lukin, Strong magnetic coupling between an electronic spin qubit and a mechanical resonator, *Phys. Rev. B* **79**, 041302(R) (2009).
- [112] G. Via, G. Kirchmair, and O. Romero-Isart, Strong Single-Photon Coupling in Superconducting Quantum Magnetomechanics, *Phys. Rev. Lett.* **114**, 143602 (2015).
- [113] J. Jackson, *Classical Electrodynamics* (Wiley, New York, USA, 1975).
- [114] E. Wohlfarth, *Handbook of Magnetic Materials*, Ferromagnetic Materials: A Handbook on the Properties of Magnetically Ordered Substances Vol. 2 (Elsevier Science, Amsterdam, the Netherlands, 1986).
- [115] A. Krysztofik, H. Glowiński, P. Kuświk, S. Ziętek, L. E. Coy, J. N. Rychły, S. Jurga, T. W. Stobiecki, and J. Dubowik, Characterization of spin wave propagation in (111) YIG thin films with large anisotropy, *J. Phys. D: Appl. Phys.* **50**, 235004 (2017).
- [116] B. A. Kalinikos, M. P. Kostylev, N. V. Kozhus, and A. N. Slavin, The dipole-exchange spin wave spectrum for anisotropic ferromagnetic films with mixed exchange boundary conditions, *J. Phys.: Condens. Matter* **2**, 9861 (1990).
- [117] G. Rado and J. Weertman, Spin-wave resonance in a ferromagnetic metal, *J. Phys. Chem. Solids* **11**, 315 (1959).
- [118] Q. Wang, B. Heinz, R. Verba, M. Kewenig, P. Pirro, M. Schneider, T. Meyer, B. Lägel, C. Dubs, T. Brächer, and A. V. Chumak, Spin Pinning and Spin-Wave Dispersion in Nanoscopic Ferromagnetic Waveguides, *Phys. Rev. Lett.* **122**, 247202 (2019).
- [119] R. E. De Wames and T. Wolfram, A new type of surface spin wave in ferromagnetic films, *Appl. Phys. Lett.* **15**, 297 (1969).
- [120] R. E. De Wames and T. Wolfram, Dipole-exchange spin waves in ferromagnetic films, *J. Appl. Phys.* **41**, 987 (1970).
- [121] R. E. De Wames and T. Wolfram, Experimental Test for Pinned Spins in Ferromagnetic Resonance, *Phys. Rev. Lett.* **26**, 1445 (1971).
- [122] T. Wolfram and R. E. De Wames, Macroscopic and Microscopic Theories of Dipole-Exchange Spin Waves in Thin Films: Case of the Missing Surface States, *Phys. Rev. Lett.* **24**, 1489 (1970).
- [123] T. Yu, C. Liu, H. Yu, Y. M. Blanter, and G. E. W. Bauer, Chiral excitation of spin waves in ferromagnetic films by magnetic nanowire gratings, *Phys. Rev. B* **99**, 134424 (2019).
- [124] Z. Liu, F. Giesen, X. Zhu, R. D. Sydora, and M. R. Freeman, Spin Wave Dynamics and the Determination of Intrinsic Damping in Locally Excited Permalloy Thin Films, *Phys. Rev. Lett.* **98**, 087201 (2007).
- [125] T. Sebastian, K. Schultheiss, B. Obry, B. Hillebrands, and H. Schultheiss, Micro-focused Brillouin light scattering: imaging spin waves at the nanoscale, *Front. Phys.* **3**, 35 (2015).
- [126] Y. Acremann, C. H. Back, M. Buess, O. Portmann, A. Vaterlaus, D. Pescia, and H. Melchior, Imaging precessional motion of the magnetization vector, *Science* **290**, 492 (2000).
- [127] T. Wolf, P. Neumann, K. Nakamura, H. Sumiya, T. Ohshima, J. Isoya, and J. Wrachtrup, Subpicotesla Diamond Magnetometry, *Phys. Rev. X* **5**, 041001 (2015).
- [128] J. Wrachtrup and A. Finkler, Single spin magnetic resonance, *J. Magn. Reson.* **269**, 225 (2016).
- [129] W. Wasilewski, K. Jensen, H. Krauter, J. J. Renema, M. V. Balabas, and E. S. Polzik, Quantum Noise Limited and Entanglement-Assisted Magnetometry, *Phys. Rev. Lett.* **104**, 133601 (2010).
- [130] M. P. Ledbetter, I. M. Savukov, D. Budker, V. Shah, S. Knappe, J. Kitching, D. J. Michalak, S. Xu, and A. Pines, Zero-field remote detection of nmr with a microfabricated atomic magnetometer, *Proc. Natl. Acad. Sci. USA* **105**, 2286 (2008).
- [131] A. Montoya-Castillo, T. C. Berkelbach, and D. R. Reichman, Extending the applicability of redfield theories into highly non-markovian regimes, *J. Chem. Phys.* **143**, 194108 (2015).

- [132] M. Campisi, S. Denisov, and P. Hänggi, Geometric magnetism in open quantum systems, *Phys. Rev. A* **86**, 032114 (2012).
- [133] Y. Liu and A. A. Houck, Quantum electrodynamics near a photonic bandgap, *Nat. Phys.* **13**, 48 (2017).
- [134] L. Novotny and B. Hecht, *Principles of Nano-Optics* (Cambridge University Press, New York, USA, 2006).
- [135] C. A. Marocico and J. Knoester, Effect of surface-plasmon polaritons on spontaneous emission and intermolecular energy-transfer rates in multilayered geometries, *Phys. Rev. A* **84**, 053824 (2011).
- [136] P. A. Huidobro, A. Y. Nikitin, C. González-Ballesterro, L. Martín-Moreno, and F. J. García-Vidal, Superradiance mediated by graphene surface plasmons, *Phys. Rev. B* **85**, 155438 (2012).
- [137] P. Lodahl, S. Mahmoodian, S. Stobbe, A. Rauschenbeutel, P. Schneeweiss, J. Volz, H. Pichler, and P. Zoller, Chiral quantum optics, *Nature (London)* **541**, 473 (2017).
- [138] A. González-Tudela, P. A. Huidobro, L. Martín-Moreno, C. Tejedor, and F. J. García-Vidal, Theory of Strong Coupling between Quantum Emitters and Propagating Surface Plasmons, *Phys. Rev. Lett.* **110**, 126801 (2013).
- [139] R. Barakat, Probability density functions of sums of sinusoidal waves having nonuniform random phases and random numbers of multipaths, *J. Acoust. Soc. Am.* **83**, 1014 (1988).
- [140] G. Andersson, A. L. O. Bilobran, M. Scigliuzzo, M. M. de Lima, J. H. Cole, and P. Delsing, Acoustic spectral hole-burning in a two-level system ensemble, *npj Quantum Inf.* **7**, 15 (2021).